

**Polarimetric Decomposition of Fully Polarimetric Synthetic Aperture
RADAR to Examine Freshwater Lake Ice Microwave Backscatter
Behaviour**

by

Connor McRae-Pharo

A thesis

presented to the University of Waterloo

in fulfillment of the

thesis requirement for the degree of

Master of Science

in

Geography

Waterloo, Ontario, Canada, 2025

© Connor McRae-Pharo 2025

Author's Declaration

I hereby declare that I am the sole author of this thesis. This is a true copy of the thesis, including any required final revisions, as accepted by my examiners.

I understand that my thesis may be made electronically available to the public.

Abstract

Lake ice, a critical component of the cryosphere, plays an essential role in climate regulation, freshwater availability, and the socio-economic stability of northern communities. Despite its importance, the interaction between lake ice and microwave signals remains insufficiently understood, particularly regarding how average lake depth influences microwave backscatter behavior. This study systematically analyzed fully polarimetric C-band, X-band, and L-band SAR data across multiple sites to determine the dominant scattering mechanisms driving lake ice backscatter. The findings demonstrate that single-bounce scattering is the predominant mechanism across all studied sites, irrespective of lake depth and wavelength, aligning with recent research that challenges traditional assumptions about the role of tubular bubbles in backscatter enhancement. These results have refined our understanding of SAR-based lake ice backscatter, paving the way for more tangible microwave-based lake ice monitoring techniques. By advancing knowledge of microwave-ice interactions, this research enhances remote sensing applications for cryospheric studies and provides critical insights into lake ice dynamics under changing climatic conditions.

Acknowledgements

This thesis is the culmination of several years of research, exploration, and personal growth, and it would not have been possible without the guidance, support, and encouragement of many people.

First and foremost, I would like to extend my deepest gratitude to my supervisor, Dr. Grant Gunn, for their unwavering support, invaluable feedback, and insightful advice throughout this process. Their expertise and mentorship have been instrumental in shaping both my research and my approach to problem-solving. I am truly fortunate to have had the opportunity to gain experience from such a dedicated and knowledgeable mentor. I would also like to thank my committee members, Dr. Richard Kelly and Dr. Wesley Van-Wychen, for their time, and guidance.

To my colleagues and lab mates, thank you for creating an environment of collaboration, support, and camaraderie. I am grateful for the countless discussions, shared frustrations, and successes we experienced together. Special thanks to Danielle Hallé, Peter Wray, and Ariana Mansingh whose friendship and encouragement have meant the world to me throughout this journey.

To my family and friends, your patience, understanding, and unwavering belief in me have been a constant source of strength. To my parents, thank you for always being there, cheering me on, and reminding me to take breaks. To my friends, thank you for keeping me grounded, for the laughs, and for reminding me that there is in fact a life beyond radar and research.

This thesis is a reflection of all the people who have helped, supported, and inspired me along the way, and for that, I am deeply grateful.

Table of Contents

Author’s Declaration	ii
Abstract	iii
Acknowledgements	iv
List of Figures	viii
List of Tables.....	x
List of Abbreviations.....	xi
Chapter 1 : Introduction.....	1
1.1 Motivation	1
1.2 Objectives.....	3
Chapter 2 : Background.....	4
2.1 Lake-Ice Formation	4
2.2 Lake Ice Influences on Meteorology	5
2.3 History of Microwave Remote Sensing of Lake Ice	6
2.4 : Microwave Remote sensing Fundamentals.....	10
2.4.1 Microwave Polarization.....	10
2.4.2 Dielectrics.....	12
2.4.3 Matrices	14
2.4.4 Polarimetric Decomposition.....	16
2.4.5 Scattering Mechanisms.....	19
2.4.6 SAR Systems	22
Chapter 3 : Study Areas.....	26
3.1 Old Crow Flats	26

3.2 Noel Lake	28
3.3 Churchill.....	31
3.4 Lena River Delta	33
3.5 Alaska North Slope	35
Chapter 4 : Data and Methods	37
4.1 SAR Acquisitions	38
4.2 Polarimetric Data.....	40
4.3 Polarimetric Decomposition.....	41
4.4 Co-Polarization Analysis.....	45
4.5 Methodological Limitations and Uncertainty.....	45
Chapter 5 : Results	48
5.1 Old Crow	48
5.2 Noel Lake	58
5.3 Multiple Lakes and Wavelengths	67
5.3.1 TanDEM-X.....	69
5.3.2 SAOCOM.....	78
5.3.3 RADARSAT 2.....	85
Chapter 6 : Discussion.....	91
6.1 Polarimetric Decomposition.....	91
6.1.1 Single Bounce.....	91
6.1.2 Double-Bounce.....	95
6.1.3 Volume Scattering	97
6.2 Co-polarization.....	99
6.3 Uncertainty	100

Chapter 7 : Conclusion	104
7.1 Summary of Key Findings.....	104
7.2 Limitations.....	106
7.3 Future Work	107
References	109

-

List of Figures

Figure 1: Location of Old Crow Lake in the Old Crow Flats, Yukon. Lakes Highlighted were examined in study.....	27
Figure 2: Mean temperatures and snow on ground for Old Crow Flats	28
Figure 3: Noel Lake study area, near Inuvik, Northwest Territories. Lakes highlighted were examined in study.....	29
Figure 4: Noel Lake mean temperatures and snow on ground acquired by Environment Canada weather station located at 68.3594° N, 133.7294° W.....	30
Figure 5: Capture area for Churchill, Manitoba. Lakes Highlighted were examined in study.....	31
Figure 6: Capture area for Lena River Delta Study Area. Lakes highlighted were used in study.....	33
Figure 7: Capture area for the Alaska North Slope, near Utqiagvik, Alaska. Lakes highlighted were used in study.....	35
Figure 8: Methods Flow Diagram	37
Figure 9: Old Crow, RADARSAT 2 Standard Quad-Pol Beammode 24. Median signal power.....	49
Figure 10: Old Crow, RADARSAT-2 Standard Quad-Pol Beammode 24. Average relative power.....	50
Figure 11: Old Crow, RADARSAT-2 Standard Quad-Pol Beammode 24. Average proportion of signal	51
Figure 12: Old Crow, RADARSAT 2 Standard Quad-Pol Beam mode 16, median backscatter power.....	63
Figure 13: Old Crow, RADARSAT 2 Standard Quad-Pol Beam mode 16, relative power.....	64
Figure 14: Old Crow, RADARSAT 2 Standard Quad-Pol Beam mode 16, proportion of signal.....	65
Figure 15: C-band co-polarization ratio for fine beam quad mode 19 from 2011-2012 at Old Crow (RADARSAT 2).....	67
Figure 16: Old Crow scattering mechanisms in grey scale. SQ24, RADARSAT-2, 2011.....	69
Figure 17: Noel Lake, RADARSAT 2 Fine Quad-Pol Beam mode 2, mean backscatter power (dB).....	70
Figure 18: Noel Lake, RADARSAT 2 Fine Quad-Pol Beam mode 2, relative power.....	73
Figure 19: Noel Lake, RADARSAT 2 Fine Quad-Pol Beam mode 2, proportion of signal.....	75

Figure 20: Noel Lake, RADARSAT 2 Fine Quad-Pol Beam mode 19, mean backscatter power (dB).....	76
Figure 21: Noel Lake, RADARSAT 2 Fine Quad-Pol Beam mode 19, proportion of signal.....	77
Figure 22: Noel Lake, RADARSAT 2 Fine Quad-Pol Beam mode 19, relative signal power.....	77
Figure 23: Noel Lake, RADARSAT 2, co-polarization returns.....	79
Figure 24: Noel Lake scattering mechanisms in grey scale. FQ19W, RADARSAT-2, 2018.....	80
Figure 25: All sites and beam modes, RADARSAT 2, SAOCOM, and TanDEM-X, average relative signal intensity visualized in linear power. Showing all wavelengths and scattering types.....	92
Figure 26: Mean backscatter power broken out by lake depths. 2m depth binning interval. TanDEM-X, 2015. Strip-map Far 8. Incidence angles 30-50°.....	93
Figure 27: Mean signal proportion by depth. 2m depth binning interval. TanDEM-X, 2015. Strip-map Far 8. Incidence angles 30-50°.....	94
Figure 28: Mean backscatter power broken out by lake depths for Churchill. 2m depth binning interval. TanDEM-X, 2015. Strip-map Far 8. Incidence angles 30-50°.....	95
Figure 29: Mean signal proportion broken out by lake depths for Churchill. 2m depth binning interval. TanDEM-X, 2015. Strip-map Far 8. Incidence angles 30-50°.....	95
Figure 30: Mean backscatter power broken out by lake depths for Lena River Delta. 2m depth binning interval. TanDEM-X, 2015. Strip-map Far 8. Incidence angles 30-50°.....	96
Figure 31: Mean signal proportion broken out by lake depth, Lena River Delta. 2m depth binning interval. TanDEM-X, 2015. Strip-map Far. Incidence angles 30-50°.....	96
Figure 32: Mean backscatter power by depth class for Noel Lake. 2m depth binning interval. SAOCOM, 2021, TOPSAR, incidence angle 20-45°.....	97
Figure 33: Mean signal proportion by depth class for Noel Lake. 2m depth binning interval. SAOCOM, 2021, TOPSAR, incidence angle 20-45°.....	97
Figure 34: Mean backscatter power by depth class for Old Crow. 2m depth binning interval. SAOCOM, 2021, TOPSAR, incidence angle 20-45°.....	98
Figure 35: Mean signal proportion by depth class for Old Crow. 2m depth binning interval. SAOCOM, 2021, TOPSAR, incidence angle 20-45°.....	98
Figure 36: Mean backscatter power by depth class for Noel Lake. 2m depth binning interval. RADARSAT 2, 2019, Fine-Quad Pol Beam mode 19. Incidence angle 20-45°.....	99
Figure 37: Mean signal proportion by depth class for Noel Lake. 2m depth binning interval. RADARSAT 2, 2019, Fine-Quad Pol Beam mode 19. Incidence angle 20-45°.....	99
Figure 38: Mean backscatter power by depth class for Old Crow. 2m depth binning interval. RADARSAT 2, 2019, Fine-Quad Pol Beam mode 19. Incidence angle 20-45°.....	100
Figure 39: Mean signal proportion by depth class for Old Crow. 2m depth binning interval. RADARSAT 2, 2019, Fine-Quad Pol Beam mode 19. Incidence angle 20-45°.....	100

List of Tables

Table 1: Polarimetric SAR platforms	25
Table 2: SAR acquisitions utilized in study	39

List of Abbreviations

ASAR	Advanced Synthetic Aperture Radar
CONAE	National Space Activities Commission
SAR	Synthetic Aperture Radar
RADAR	Radio detecting and ranging
EM	Electro Magnetic
EMS	Electro Magnetic Spectrum
EOWEB	Earth Observation Web Portal
EODMS	Earth Observation Data Management System
FD	Freeman-Durden
HH	Horizontal Horizontal
HV	Horizontal Vertical
MLC	Multi Look Complex
PD	polarimetric decomposition
PolSAR	Polarimetric Synthetic Aperture Radar
RMS	Root Mean Square
SLAR	Side Looking RADAR
SNAP	Sentinel Application Platform
SLC	Single Look Complex
VV	Vertical Vertical
VH	Vertical Horizontal
YFD	Yamaguchi-Freeman-Durden

Chapter 1: Introduction

1.1 Motivation

Lake ice is a dynamic component of the cryosphere, intimately linked with the broader environmental and climate systems. Covering significant portions of the Northern Hemisphere, particularly in North America's Arctic and Subarctic regions, lake ice plays a crucial role in regional climate regulation, water storage, and ecosystems (Brown et al. 2010; Duguay et al. 2003). The presence of lake ice and the associated variability of timing and duration of ice cover have direct implications on freshwater availability and the regional energy balance due to its reflective properties and insulation effects (Brown et al. 2010).

From a utilitarian perspective, the formation of lake ice is essential for temporary transportation routes in remote areas, significantly impacting the logistics and economy of Northern communities (Arp et al. 2019). The ice cover facilitates the seasonal movement of goods and personnel, otherwise impossible due to the lack of permanent infrastructure. The economic and social stability provided by these ice roads is vital, yet increasingly threatened by a warming climate (Kirillina et al. 2023).

Ecologically, lake ice serves as a critical barrier that modulates gas exchanges and thermal interactions between the atmosphere and the aquatic environment (Griffiths et al. 2017). This barrier supports unique ecological niches and affects biogeochemical cycles. However, the sensitivity of lake ice to climatic warming poses risks to biodiversity and ecological productivity (Griffiths et al. 2017).

Given the significant influence of lake ice on various systems, the importance of accurately monitoring and understanding its characteristics cannot be overstated. Traditional in-situ measurement techniques have been supplanted by remote sensing methods due to their ability to

provide extensive spatial coverage and frequent data collection, crucial for capturing the dynamic nature of lake ice (Gunn et al. 2018). Remote sensing technologies, particularly microwave remote sensing, have shown promise in overcoming the limitations of ground-based observations by providing detailed data on ice thickness, extent, and condition across vast and inaccessible areas (Ferguson et al. 2020).

Despite significant advancements in remote sensing technology, accurately capturing and modeling the characteristics and impacts of lake ice remain challenging due to the complex interplay between ice cover and its surrounding environment. The research community has made significant progress in the identification of key phenological events (freeze-up and melt), but the underlying mechanisms of microwave interactions with freshwater ice remains unclear. Historically, the discipline's view was that the formation of tubular bubbles at the ice water interface cause an increase in backscatter due to double-bounce scattering mechanisms (Weeks et al, 1976). This view has become widely challenged, with recent studies examining how microwave interact with freshwater ice cover (Gunn et al, 2018).

The major challenge in this field is the determination of which variables significantly influence ice roughness, and, as a result, the backscatter signal (Murfit et al, 2024). Smaller lakes, for example, tend to show a higher backscatter throughout the progression of winter, which led to the historical hypothesis that bubble inclusions are responsible. Regardless, this relationship has not been straightforward to establish, and other physical parameters of the ice could be playing a critical role. The relative depth and morphology of lakes has yet to be systematically explored, as variations in either could affect the overall characteristics of lake ice, and therefore the scattering regime.

This research is pertinent in the context of environmental monitoring and climate change response, as lake ice is exceptionally sensitive to environmental conditions. Any changes or regional

variations in air temperature and precipitation can have exceptional effects on the timing of phenological events, ice stability, and ice-thickness. These changes in turn can have considerable trickle-down effects on socio-economic function, water resource management, transportation infrastructure, and recreational activities (Magnuson et al. 2014). Therefore, before expanding our understanding of lake ice dynamics via remote sensing techniques, it must be confirmed where within the freshwater ice structure the microwaves are interacting with. The stated gap that this research aims to fill, will advance our understanding of microwave freshwater ice interactions.

1.2 Objectives

The overarching research objective of this thesis is to expand our understanding of microwave-ice interactions, by identifying and quantifying the dominant backscattering signal from lakes of contrasting morphometries. There are two important considerations which guide this study: the role of various ice structures and inclusions, and the role of morphometry. To accomplish the overarching objective of this study, two specific objectives are:

- 1) Identify the differences in microwave backscattering behaviour of lakes of differing depths
- 2) Utilize polarimetric decomposition algorithms to quantify the dominant scattering mechanisms associated with lakes of different sizes.

Chapter 2: Background

2.1 Lake-Ice Formation

Air temperature, driving the energy balance of lakes, is key to the initiation, growth, and decay of lake ice. However, when considering the types of ice which forms, other factors, such as snow, lake depth, and wind, play a significant determining factor (Duguay et al, 2003, Adams et al, 1984) In general there are three layers of freshwater ice: primary, secondary and superimposed ice, each of which have unique characteristics and are formed by different processes (Michel et al, 1971). Primary ice is the first stage in freshwater ice formation, occurring in calm conditions, forming a thin ice cover layer (Kirillin et al, 2012) This stage can be disrupted by wind or the introduction of snow. Secondary ice (i.e. congelation ice) is ice which forms from the bottom of ice cover, beneath the primary ice layer, and is characterized by elongated columnar crystals, orientated in a vertical direction (Michel et al, 1971). This uniformity of orientation is what give this class of ice its transparent characteristic (Kirillin et al, 2012). The important physical characteristic that drives the formation of this ice is the thickness of existing ice, water density, latent heat, and air temperature (Bengtsson, 1986). The superimposed layer, often called snow ice, forms when snow deposited on the primary layer becomes flooded and freeze, creating a mass of randomly orientated ice crystals (Michel et al, 1971, Bengtsson, 1986). Secondary ice and superimposed ice layers differ primarily in their crystal orientation and formation processes: secondary ice features highly ordered, vertically aligned columnar crystals that create a transparent appearance typical of black ice, while superimposed ice, formed from refrozen slush or meltwater, contains randomly oriented crystals that scatter light, resulting in the opaque appearance characteristic of white ice (Kirillin et al, 2012, Bengtsson, 1986).

In addition to the classes of ice there are a number of inclusions found within the ice structure stemming from gases released from decomposition, gas saturation in water, rapid freezing due to a cold snap, different types of snow granules, or flooded cracks and deformations (Engram et al. 2013; Gunn et al. 2018). Of all these inclusions one of them is an important consideration in the realm of microwave remote sensing and has been the cause of some debate. This inclusion, the tubular bubble, is an elongated column of air, which forms at the ice-water interface and is incorporated into the ice column, and is orientated vertically (Murffit et al. 2022; Gunn et al. 2018). Forming a dense mat at the ice-water interface, they have prominent geometry, appearing similar to a bunch of hairs. These inclusions are formed exclusively in waterbodies with depth no greater than 4.7m and are a result of gas saturation in the water column (Murffit et al. 2022). This gas saturation is not formed by an input of gases into the system but is seeded by the removal of water from the water body by freezing ice, which causes a supersaturation of dissolved gas (Gunn et al. 2018). Gas concentration and ice growth speed directly controls the concentration and length of the tubular bubbles, leading to some variance in structure (Yoshimura et al. 2008). Essentially, as the ice draws water from a shallow lake, it reduces the holding capacity of the water for gases, and since the water is sealed in by the ice cap it cannot easily exchange with the atmosphere (Yoshimura et al. 2008). This eventually causes the gas to become supersaturated and small bubbles to bead upon the ice-water interface (Yoshimura et al. 2008). These small bubbles are then incorporated into the ice structure creating elongated tubular bubbles at the ice-water interface (Yoshimura et al. 2008).

2.2 Lake Ice Influences on Meteorology

The presence of lakes influences the overall meteorological conditions of an area, dependent on the percentage of landcover, with the greatest effects brought on by ice cover on large lakes (Prowse et al. 2011). The presence and absence of lake ice can be thought of as a tarp over a landfill,

when the tarp is present no gases release, when the tarp is gone gases escape. Translating this metaphor, when ice is present on the lakes surface, the transfer of heat and moisture to the atmosphere is significantly reduced, limiting both as inputs from the various regional energy budgets and moisture to the local environment. When the ice is no longer present then the lake acts as a source or store of heat and moisture. This, in turn, influences local weather conditions, including surface-air temperature, rainfall, evaporation rates, and the formation of clouds close to the ground (Prowse et al. 2011). The magnitude of lake ice's effect on the atmosphere depends on a number of factors such as latitude, ice-cover duration and timing of phenological events (Brown et al. 2010). Additionally, depending on frequency and size, lakes considerably affect regional evaporative and sensible heat inputs to the atmosphere, making them crucial for regional climatic and meteorological processes (Rouse et al. 2005).

2.3 History of Microwave Remote Sensing of Lake Ice

During the 2000's a number of airborne polarimetric Synthetic Aperture Radar (PolSAR) were employed for scientific research (MAESTRO, INDREX, AGRISAR, BIOSAR, AfriSAR, etc.) with success, introducing a new wave of spaceborne polarimetric microwave sensors (Hajnsek and Desnos 2021). The utility of microwave sensors lies in the ability to penetrate through ground cover to see the underlying terrain, and to characterize target's structure (Hajnsek & Desnos, 2021). In addition to airborne PolSARs, the Advanced Synthetic Aperture Radar (ASAR) sensor, mounted on the ENVISAT satellite and launched in 2002, was able to alternate polarizations, thus rendering it multi-polarization capable (Hajnsek and Desnos 2021). These feature of ASAR and PolSARs not only highlighted the utility but also cemented the critical importance of multi-polarization platforms in advancing scientific research, opening the door to more powerful and purpose-built platforms (Hajnsek and Desnos 2021). In the late 2000's three PolSAR platforms were launched into space:

Japan Aerospace Exploration Agency's ALOS, Canadian Space Agency's RADARSAT-2, and German Aerospace Centre's TanDEM-X (Hajnsek and Desnos 2021). The data that these systems would collect would open the door to more complex analysis of cryospheric features, allowing for greater explorations into the dynamics of microwave and freshwater ice interactions. Using these sensors, researchers have identified that a long-held theory in the microwave fresh-water ice remote sensing community that tubular bubbles cause double-bounce of the signal may not be sound, warranting further exploration (Engram et al., 2013, Atwood et al., 2015, Gunn et al., 2018).

Initial investigations into the interaction between microwave signals and lake ice, utilizing X-band Side-Looking Airborne Radar (SLAR), noted a significant increase in backscatter responses as winter progressed (Weeks et al. 1978). The variances in radar responses from lakes on the Alaskan North Slope was attributed to a double-bounce interactions with the long, tubular-shaped bubbles present within the ice column (Weeks et al. 1978). It was hypothesized that the structure of the bubbles aligned with the ice growth direction and acted as forward scatterers, reflecting the microwaves downwards to the ice-water interface, where upon they would reflect back to the sensor (Weeks et al. 1978). Satellite observations acquired in 1994 via the European Remote-Sensing Satellite-1 (ERS-1), a C-band radar, over the North Slope of Alaska revealed an increase in backscatter concurrent with ice thickening and the development of tubular bubbles, lending further credence to this theory (Jeffries et al. 1994). The role of tubular bubbles and double bounce scattering within lake ice was further corroborated through C-band radar imagery and field studies in shallow lakes across Alaska and Manitoba (Duguay et al. 2002; Morris et al. 1995). As well, additional ERS-1 observations of deeper and larger lakes showed a reduction in backscatter response, which was attributed to the absences of tubular bubbles (Morris et al. 1995)

Recent exploration of lake ice scattering mechanisms has been significantly advanced by the advent and availability of PolSAR data. This technology is instrumental in the distinction of the several scattering mechanisms (surface, volume, double bounce and helical) which make up the backscatter signal (Murfit et al. 2022). When considering lake ice, only three of the four scattering mechanisms are generally found, specifically single bounce, double bounce, and volumetric scattering, while the fourth is associated with urban structures (helical) (Atwood et al. 2015 ; Yamaguchi et al. 1998). Using L-band acquisitions from ALOS-PALSAR, Engram et al., (2009) observed that the return from floating ice is primarily influenced by surface bounce (Engram et al. 2013). In 2015, using imagery from TerraSAR-X, ALOS PALSAR, and RADARSAT-2, single bounce scattering at the ice-water interface was observed to be predominant in X, C, and L-band (Atwood et al., 2015). A key component of this study was that the single bounce was found to be dominant regardless of the presence methane ebullitions (Atwood et al. 2015). Utilizing RADARSAT-2 images for shallow sub-Arctic lakes near Churchill, Manitoba, surface scattering from the ice-water interface was observed to be the primary contributor to backscatter throughout the winter season (Gunn et al. 2018). Recent research currently hypothesizes that single-bounce is the dominant scattering mechanism in lake ice and is driven by variations in surface roughness at the ice-water interface (Engram et al., 2012; Atwood et al. 2015; Gunn et al., 2018). These variations in surface roughness could stem from factors such as a) the extrusion of bubble terminuses at the ice-water interface, b) differing snow depths across the ice surface affecting ice thickness, or c) the presence of methane ebullition bubbles (Engram et al., 2012; Atwood et al. 2015; Gunn et al., 2018). These studies using TerraSAR-X, ALOS PALSAR, and RADARSAT-2 images, have indicated that surface scattering from a rough ice-water interface is the dominant scattering mechanism, which stands in contrast to previous research.

As the evidence mounts in opposition to double-bounce microwave interaction, there remains a need for further investigation into the composition of the scattering mechanisms that comprise the backscatter intensity observed at the sensor. Recent research (Engram et al., 2012; Atwood et al. 2015; Gunn et al., 2018) has significantly illuminated the role of single-bounce scattering in microwave backscatter, the realm of deep lakes, where the formation of tubular bubbles is scant, remains unexamined (Murfitt et al. 2022). To fill this gap, it is imperative to identify and select lakes exceeding 4.7 m in depth (which is the threshold where formation of tubular bubbles is significantly reduced), that have been observed by PolSAR (Murfitt et al. 2022). In pursuit of a robust science, capturing a timeseries that spans the entire winter season is vital, as a comprehensive dataset of this nature would highlight the evolution of backscatter behavior over time. This is critical as it will offer invaluable insights into the dynamic processes of lake ice throughout the winter season. A study of this nature is particularly important considering the rapid advancements in the field of lake ice microwave remote sensing, with a keen interest in the development of ice thickness products. If these products, which are still in their infancy, are to reach their full potential and efficacy, especially in applications such as climate monitoring, ecological studies, and community planning in northern regions, an accurate understanding of microwave interactions is indispensable. Moreover, unraveling the microwave backscatter of deeper lakes will expand our current knowledge and pave the way for more precise and reliable measurements. This, in turn, can significantly contribute to our understanding of climate dynamics, hydrological cycles, and ecosystem health in cold regions, where lakes play a pivotal role.

2.4 : Microwave Remote sensing Fundamentals

2.4.1 Microwave Polarization

Polarization describes the orientation and temporal behavior of the electric field vector of an electromagnetic (EM) wave as it propagates through space. This characteristic is crucial as it dictates how the electric and magnetic fields (which are inherently orthogonal to each other and to the direction of wave propagation) oscillate. These oscillations are not arbitrary but follow precise geometric patterns that are fundamental to understanding wave propagation and interaction with materials (Ferguson & Gunn, 2022).

EM radiation can originate from coherent and incoherent sources. Coherent sources emit EM waves whose electric fields oscillate in a synchronized manner, maintaining constant phase relationships and amplitudes across the wavefront (Woodhouse, 2017). This coherence results in predictable and uniform polarization states, ideal for applications requiring high precision such as lidar and radar systems (Lee et al, 2009). Incoherent sources in contrast produce EM waves by the random superposition of multiple waves of differing phases and amplitudes. This results in a complex, often unpredictable polarization state that can vary over time and space, typical of natural light sources and broad-spectrum emission processes (Ferguson & Gunn, 2022).

The state of an EM wave encompasses three fundamental degrees of freedom, which define its geometric and physical properties, orientation, ellipticity, and rotation (Woodhouse, 2017). Orientation refers to the angle at which the major axis of the waveform's ellipse is tilted relative to a reference direction, describing the predominant direction of the electric field vector as the wave propagates (Woodhouse, 2017). Ellipticity is ratio of the minor axis to the major axis of the ellipse traced by the electric field vector, ellipticity describes the shape of the polarization ellipse. Ellipticity varies from zero (linear polarization) to one (circular polarization), with varying degrees of elliptical

shapes in between, each representing different polarization states (Lee et al, 2009). Rotation indicates whether the electric field vector rotates left-handedly or right handedly, as viewed along the direction of wave travel (Lee et al, 2009). This aspect determines whether the polarization is right-handed or left-handed, which can affect the interaction of the wave with the surface (Lee et al, 2009).

Polarization describes the orientation and temporal behavior of the electric field vector of an electromagnetic (EM) wave as it propagates through space. This characteristic is crucial as it dictates how the electric and magnetic fields (which are inherently orthogonal to each other and to the direction of wave propagation) oscillate. These oscillations are not arbitrary but follow precise geometric patterns that are fundamental to understanding wave propagation and interaction with materials (Ferguson & Gunn, 2022).

EM radiation can originate from coherent and incoherent sources. Coherent sources emit EM waves whose electric fields oscillate in a synchronized manner, maintaining constant phase relationships and amplitudes across the wavefront (Hajnsek et al, 2021). This coherence results in predictable and uniform polarization states, ideal for applications requiring high precision such as lidar and radar systems (Hajnsek et al, 2021). Incoherent sources in contrast produce EM waves by the random superposition of multiple waves of differing phases and amplitudes. This results in a complex, often unpredictable polarization state that can vary over time and space, typical of natural light sources and broad-spectrum emission processes (Hajnsek et al, 2021)

The state of an EM wave encompasses three fundamental degrees of freedom, which define its geometric and physical properties, orientation, ellipticity, and rotation (Woodhouse, 2017). Orientation refers to the angle at which the major axis of the waveform's ellipse is tilted relative to a reference direction, describing the predominant direction of the electric field vector as the wave propagates (Woodhouse, 2017). Ellipticity is ratio of the minor axis to the major axis of the ellipse

traced by the electric field vector, ellipticity describes the shape of the polarization ellipse. Ellipticity varies from zero (linear polarization) to one (circular polarization), with varying degrees of elliptical shapes in between, each representing different polarization states (Lee et al, 2009). Rotation indicates whether the electric field vector rotates left-handedly or right handedly, as viewed along the direction of wave travel (Lee et al, 2009). This aspect determines whether the polarization is right-handed or left-handed, which can affect the interaction of the wave with the surface (Lee et al, 2009)

Understanding polarization involves examining the horizontal and vertical oscillations of the electric field, the form of the ellipse traced by these oscillations, and the phase relationship between orthogonal field components, often referred to as the mixing parameter. This understanding is crucial in microwave remote sensing applications, providing valuable information about the orientation and scattering mechanisms of surfaces like lake ice. Understanding how vertically and horizontally polarized waves interact with surfaces is particularly important in distinguishing different surface features (Van der Sanden & Geldsetzer, 2013).

Polarization is critical for interpreting the scattering properties of surfaces in remote sensing (Woodhouse, 2017). Different polarization states help differentiate between surface types based on their unique scattering characteristics. Vertically polarized waves and horizontally polarized waves interact differently with surfaces, which is essential for analyzing smooth surfaces like calm water or rough surfaces similar to lake ice (Van der Sanden & Geldsetzer, 2013).

2.4.2 Dielectrics

Following polarization another crucial variable to consider is the dielectric properties of a target medium. The relative permittivity of a target provides the foundation of understanding for how a wave reflects transmits or is absorbed by different materials. The relative permittivity can be denoted as:

$$\varepsilon^* = \varepsilon' + j\varepsilon'' \quad (3.1)$$

where ε' is the real part of the permittivity or the dielectric constant and ε'' is the imaginary part of the also know as the dielectric loss factor. Of these two elements of relative permittivity the real, or dielectric constant, value is the most critical. The dielectric constants of air, ice, and water are fundamental to understanding freshwater ice microwave remote sensing. Their distinct electrical properties, termed relative permittivity dictate how they interact with electromagnetic waves, either preventing or allowing the microwave signal to transmit through its structure. These interactions are crucial for interpreting microwave remote sensing data, as they determine the reflection, absorption, and transmission of the microwave signals. Air is characterized by an essentially non-existent dielectric constant, and in many cases is treated as a vacuum (Mätzler, 1987). This causes the atmosphere to have minimal interactions with microwave fields allowing for clear signal transmission through to the target surface. This property is what makes microwave remote sensing so attractive as it ensures that radar signals travel without significant interference from the atmosphere. Water, in its liquid form, displays a sharp contrast in its dielectric response due to its molecular structure, which aligns with incoming electric fields, leading to a high dielectric constant (Gunn et al, 2018). This high relative permittivity of liquid water, approximately 90 for C-band radar, forms a significant contrasting medium, causing notable microwave signal reflection and absorption when encountered. Relative permittivity of liquid water is frequency dependent and is explained by the Debye relaxation model, which describes how the orientation of polar molecules lags behind the applied alternating electric field, leading to dispersion and relaxation phenomena within liquid water (Debye, 1929). Uniquely, ice presents different dielectric properties from liquid water due to its well-ordered crystalline structure, which limits molecular reorientation under an electric field due to the rigid covalent hydrogen bonds of the ice lattice itself (Gunn et al, 2018). This results in a much lower

relative permittivity, of approximately 3.19 at C-band radar compared to that of water, providing a distinct interface with a large contrast for microwave reflection to occur (Gunn et al, 2018, Mätzler, 1987). The similarity between air and ice in regards to permittivity is sharply contrasted by water, creating a stark boundary between the interface of ice and water.

2.4.3 Matrices

A precursor to polarimetric decomposition, a foundation of the matrices that describe microwave scattering from PolSAR system must be provided, of which there are three critical types: coherent matrices, incoherent matrices, and the Mueller matrix. Coherent matrices capture the conversion of the pure incident polarization state by a scatterer and are represented by what is known as a Sinclair matrix [S]:

$$[S] = \begin{bmatrix} S_{HH} & S_{VH} \\ S_{HV} & S_{VV} \end{bmatrix} \quad (3.2)$$

In this matrix, S_{HH} , S_{VH} , S_{HV} , and S_{VV} represent the scattering amplitudes, where the first subscript indicates the polarization of the emitted wave (Horizontal or Vertical) and the second subscript denotes the polarization of the received wave. Specifically, S_{HH} corresponds to the scattering when both the transmitted and received waves are horizontally polarized, while S_{VV} refers to when both are vertically polarized. S_{VH} and S_{HV} are the cross-polarization terms, where the polarization of the transmitted and received waves differs—vertical for one and horizontal for the other. These Sinclair matrices are fundamental in describing dynamic backscatter processes (Ferguson & Gunn, 2022). Often, this matrix is converted into a target vector to transform it into a more manageable form for mathematical operations. For instance, the transformation into a lexicographic target vector is expressed as:

$$\mathbf{K}_{\text{Lex}} = \mathbf{K}_l = \begin{bmatrix} S_{HH} \\ \sqrt{2}S_{HV} \\ S_{VV} \end{bmatrix} \quad (3.3)$$

Here \mathbf{K}_{Lex} or \mathbf{K}_l is the lexicographic target vector, where the elements of the Sinclair matrix are organized into a column vector. This organization is a popular mathematical manipulation making the matrix more manageable for calculations. Similarly, the transformation into a Pauli target vector, which utilizes two-by-two complex matrices, is given by:

$$\mathbf{K}_{\text{Pauli}} = \mathbf{K}_p = \frac{1}{\sqrt{2}} \begin{bmatrix} S_{HH} + S_{VV} \\ S_{HH} - S_{VV} \\ 2S_{HV} \end{bmatrix} \quad (3.4)$$

In this matrix, $\mathbf{K}_{\text{Pauli}}$ or \mathbf{K}_p represents the Pauli target vector, where the Sinclair matrix elements are combined and normalized by the factor $\frac{1}{\sqrt{2}}$. The terms $S_{HH} + S_{VV}$ and $S_{HH} - S_{VV}$ are linear combinations of the matrix elements, highlighting different scattering mechanisms, while $2S_{HV}$ combines the cross-polarization terms. These two vectors represent alternative forms of the Sinclair matrix and are created for convenient use in further mathematical operations (Ferguson & Gunn, 2022). The Pauli vector is especially important as it offers a distinct perspective by interpreting the physical scattering mechanisms through mathematical operations, providing a deeper insight to the scattering targets behaviour.

For the incoherent matrices, all of the rules laid out in the coherent matrices remain true but are expanded upon due to the nature of remote sensing of targets with a natural distribution or composition of targets. A wide variety of polarimetric properties and orientations will be present, creating a significant amount of noise which must be accounted for via higher-order statistics (Ferguson & Gunn, 2022). This is achieved by taking the \mathbf{K}_{Lex} target vector and creating a new matrix, the covariance matrix or \mathbf{C}_3 , which contains all of the covariances of the elements in \mathbf{K}_{Lex}

(Cloude & Pottier, 1996). Similarly, the K_{Pauli} target vector is treated similarly to create a coherency or T_3 matrix (Cloude & Pottier, 1996).

These final matrices, which takes the form of a Mueller matrix, are employed to describe depolarizing scattering processes. Unlike coherent matrix, which are only applicable to fully polarized radiation, the incoherent matrices can describe partially polarized or depolarized radiation. The Mueller matrix, in the monostatic context takes, the form of a 3x3 matrix, capturing the polarimetric properties of the subject (Ferguson & Gunn, 2022). These matrices are created by multiplying the target vector by a transposed version of itself, which in regard to a K_p or T_3 matrix, takes on this form:

$$T_3 = \langle K_p \times K_p^{*T} \rangle = \left\langle \frac{1}{2} \begin{bmatrix} \langle |S_{HH} + S_{VV}|^2 \rangle & \langle (S_{HH} + S_{VV})(S_{HH} - S_{VV})^* \rangle & 2\langle (S_{HH} + S_{VV})S_{HV}^* \rangle \\ \langle (S_{HH} - S_{VV})(S_{HH} + S_{VV})^* \rangle & \langle |S_{HH} - S_{VV}|^2 \rangle & 2\langle (S_{HH} - S_{VV})S_{HV}^* \rangle \\ 2\langle S_{HV}(S_{HH} + S_{VV})^* \rangle & 2\langle S_{HV}(S_{HH} - S_{VV})^* \rangle & 4\langle |S_{HV}|^2 \rangle \end{bmatrix} \right\rangle \quad (3.5)$$

And for K_L or C_3 takes the form:

$$C_3 = \langle K_L \times K_L^{*T} \rangle = \left\langle \begin{bmatrix} \langle |S_{HH}|^2 \rangle & \sqrt{2}\langle S_{HH}S_{HV}^* \rangle & \langle S_{HH}S_{VV}^* \rangle \\ \sqrt{2}\langle S_{HV}S_{HH}^* \rangle & 2\langle |S_{HV}|^2 \rangle & \sqrt{2}\langle S_{HV}S_{VV}^* \rangle \\ \langle S_{VV}S_{HH}^* \rangle & \sqrt{2}\langle S_{VV}S_{HV}^* \rangle & \langle |S_{VV}|^2 \rangle \end{bmatrix} \right\rangle \quad (3.6)$$

where T indicates a transpose operation and * indicates a complex conjugation.

2.4.4 Polarimetric Decomposition

The pioneering work in polarimetric decomposition began with J. R. Huyen in the 1970s. Huyen was the first to propose that fluctuations between various polarization states could be analyzed

to deduce the dominant backscatter component in radar observations. This innovative approach involved decomposing the Mueller matrix $[M]$ into two distinct matrices:

$$[M] = [M]_s + [M]_n \quad (3.7)$$

The matrix $[M]_s$ represents an equivalent single bounce matrix, which encapsulates a stable component of the scattering process. Conversely, $[M]_n$ embodies the additional noise within $[M]$, thus differentiating the deterministic and stochastic aspects of the backscatter (Cloude & Pottier, 1996). Although this method was a significant advancement, it was limited by the ambiguity in decomposition methods, necessitating the development of a unique polarization base invariant decomposition to refine the approach (Cloude & Pottier, 1996).

Building on Huyen's foundational work, S. R. Cloude introduced a novel method in the mid-1990s that utilized coherency and covariance matrices as primary tools for extracting information from backscattering interactions.

$$C_3 = \left\langle \begin{bmatrix} \langle |S_{HH}|^2 \rangle & \sqrt{2}\langle S_{HH}S_{HV}^* \rangle & \langle S_{HH}S_{VV}^* \rangle \\ \sqrt{2}\langle S_{HV}S_{HH}^* \rangle & 2\langle |S_{HV}|^2 \rangle & \sqrt{2}\langle S_{HV}S_{VV}^* \rangle \\ \langle S_{VV}S_{HH}^* \rangle & \sqrt{2}\langle S_{VV}S_{HV}^* \rangle & \langle |S_{VV}|^2 \rangle \end{bmatrix} \right\rangle \quad (3.8)$$

$$T_3 = \left\langle \frac{1}{2} \begin{bmatrix} \langle |S_{HH} + S_{VV}|^2 \rangle & \langle (S_{HH} + S_{VV})(S_{HH} - S_{VV})^* \rangle & 2\langle (S_{HH} + S_{VV})S_{HV}^* \rangle \\ \langle (S_{HH} - S_{VV})(S_{HH} + S_{VV})^* \rangle & \langle |S_{HH} - S_{VV}|^2 \rangle & 2\langle (S_{HH} - S_{VV})S_{HV}^* \rangle \\ 2\langle S_{HV}(S_{HH} + S_{VV})^* \rangle & 2\langle S_{HV}(S_{HH} - S_{VV})^* \rangle & 4\langle |S_{HV}|^2 \rangle \end{bmatrix} \right\rangle \quad (3.9)$$

These matrices are subjected to an algebraic decomposition that identifies dominant backscatter interactions and facilitates the classification of backscatter into broad categories. This

method provides a more structured approach to categorizing the scattering mechanisms and is especially useful in analyzing and interpreting complex radar datasets (Cloude & Pottier, 1996).

A further refinement in the field of polarimetric decomposition was introduced by Freeman and Durden in 1998. Their model-based method presupposes the presence of specific scattering mechanisms within the target medium. Each mechanism is then re-expressed as a sum of individual backscatter components within a matrix. This decomposition distinguishes between three primary classes of scattering: single-bounce, double-bounce, and volume scattering. The Freeman-Durden decomposition is particularly effective in natural environments, where these three scattering mechanisms are prevalent. Each class is modeled to accurately estimate the behavior of the respective scattering mechanism, with assumptions tailored to the physical properties of the scatterers, such as cylindrical volume scatterers for volume scattering and dihedral corner reflectors for double-bounce scattering. This method is deeply rooted in the physical principles of radar scattering, providing a robust framework for interpreting polarimetric radar data (Freeman & Durden, 1998).

The latest significant enhancement to polarimetric decomposition techniques is the Yamaguchi-Freeman-Durden (YFD) decomposition, developed in 2005. This four-component model extends the Freeman-Durden three-component model by introducing an additional helix scattering component and slightly changing the formula for volume scattering as a result. This addition is particularly critical for accurately modeling urban areas, where complex structures introduce additional scattering mechanisms not present in natural settings. The YFD model addresses these complexities by incorporating the imaginary part of the $S_{HH}S_{HV}^*$ interaction, which becomes prominent in urban environments, thereby enhancing the model's applicability and accuracy in such contexts (Yamaguchi et al., 2005).

2.4.5 Scattering Mechanisms

For most natural scenes there is general assumption applied to the composition of backscattering found within the microwave signal comprises three forms: single-bounce, double-bounce, volume-scattering (SAR Handbook, 2016). For C-band radar systems, Murfit et al. (2022), identified, through modelling, the structures which are responsible for the three backscattering mechanisms present at lake ice sites (Murfit et al., 2022). Single-bounce scattering is attributed to several distinct interactions, including cracks or deformations on the ice surface, the roughness at the ice-water interface, the presence of bubble terminus extrusions, and reflections from overflow or wet snow (Wakabayashi, 1999). If a high proportion of double-bounce scattering is observed, the current hypothesis is that these interactions primarily arise from tubular bubbles embedded within the ice structure (Murfit et al., 2022). Volume scattering, on the other hand, is associated with internal structures within the ice column near the snow-ice interface that scatter the radar signals in multiple directions (Fung et al, 1992). Understanding the specific structures linked to each scattering mechanism, and how they are quantified by the Yamaguchi Freeman-Durden decomposition, provides a clear interpretation of polarimetric SAR data.

2.4.5.1 Single Bounce

There are two types of single bounce scattering mechanisms: specular and diffuse. Specular backscatter occurs when the incoming signal reflects off a smooth surface, such as water (Lee et al, 2009). This smooth surface acts like a mirror and sends most of the signal off into space, resulting in low backscatter. The second, and more important for this study, is diffuse scattering, and from now on when discussing single bounce, diffuse scattering is being referenced. Diffuse scattering occurs when the incoming radar signal interacts with a sufficiently rough surface, causing the signal to scatter in all directions, including back towards the sensor. The amount of returning backscatter is

dependent on the roughness of the surface, which can be described by the Fraunhofer roughness criterion:

$$h_{\text{smooth}} < \frac{\lambda}{32 \cos \theta} \quad (3.10)$$

Where λ is the wavelength and θ represents the incident angle of the incoming wave (Woodhouse, 2017). The surface is considered rough if the height variations of a surface exceed the wavelength divided by 32 cosine incidence angle. Furthermore, since the Yamaguchi-Freeman-Durden decomposition method models surface scattering as Bragg surfaces, which determines the surface roughness to exhibit a regular and periodic pattern, this roughness metric is simplified to $h_{\text{smooth}} < \frac{\lambda}{8}$ (Woodhouse, 2017). The YFD method builds upon the original Freeman-Durden method, which uses first order Bragg scattering model for the surface-bounce and focuses on the diagonal elements of $\langle |S_{HH}|^2 \rangle$ and $\langle |S_{VV}|^2 \rangle$ (Yamaguchi et al., 2005). This approach assumes that the like-polarized and cross-polarized elements of the covariance matrix are uncorrelated (Yamaguchi et al., 2005). This results in a product that effectively isolates the single-bounce scattering from the total signal composition and identifies its overall contribution (Yamaguchi et al., 2005).

2.4.5.2 Double Bounce

Double-bounce scattering is characterized by the interaction of microwaves with two orthogonal surfaces, often forming what are referred to as corner reflectors (Lee et al., 2009; Woodhouse, 2017). These structures typically involve a vertical and a horizontal surface, such as the open expanse of a flat field and the elongated trunk of a coniferous tree. The incident microwave signal reflects off one surface, then the other, and is directed back toward the emission source along the same path. This process results in a strong backscatter signal, as a significant portion of the microwave energy is returned directly to the source, making double-bounce scattering a key indicator of urban

environments and man-made structures (Lee et al., 2009; Chen et al, 2018). Similarly to single-bounce, the YFD makes no changes to the FD method for double-bounce (Yamaguchi et al., 2005). The model isolates the double-bounce scattering contribution by analyzing the phase differences between $\langle |S_{HH}|^2 \rangle$ and $\langle |S_{VV}|^2 \rangle$ (Yamaguchi et al., 2005). This is accomplished by introducing the off-diagonal element $\langle S_{HH}S_{VV}^* \rangle$, which provides the wave's phase information and shows the correlations between $\langle |S_{HH}|^2 \rangle$ and $\langle |S_{VV}|^2 \rangle$ channels (Yamaguchi et al., 2005). As well, the cross-polarization elements $\sqrt{2}\langle S_{HH}S_{HV}^* \rangle$ and $\sqrt{2}\langle S_{VV}S_{HV}^* \rangle$ and considered to confirm that the phase and power returns are consistent (Yamaguchi et al., 2005). This comprehensive approach allows the YFD method to accurately separate and quantifies the contributions of double-bounce in the microwave signal (Yamaguchi et al., 2005).

2.4.5.3 Volume Scattering

Volume scattering is characterized by the interaction between a microwave and multiple, randomly oriented and spaced, scatterers within a medium, before the waves return to the source (Chen et al, 2018; Woodhouse, 2017). This scattering occurs when the microwave's path is intercepted by discrete elements that cause the wave to scatter in various directions, thereby complicating the signal's return pattern (Chen et al, 2018). Volume scattering is where YFD begins to differ from the FD, removing the scattering which can be attributed to helical structures from being represented in the volume scattering. The model isolates volume scattering by employing rotation matrix, second-order matrix statistics, and comparing the overall magnitude of $\langle |S_{HH}|^2 \rangle$ and $\langle |S_{VV}|^2 \rangle$. Due to the randomly orientated nature of a volume scattering a rotation is necessary to align the scattering matrix with the radar's coordinate system. The rotation matrix takes the form:

$$R(\phi) = \begin{bmatrix} \cos\phi & -\sin\phi \\ \sin\phi & \cos\phi \end{bmatrix} \quad (3.11)$$

This rotational matrix is applied to a scattering matrix taking on this form:

$$S = \begin{bmatrix} S_V & 0 \\ 0 & S_H \end{bmatrix} \quad (3.12)$$

The resulting scattering matrix after rotation is:

$$\begin{aligned} R(\phi) * S * R(\phi)^{-1} = \\ \begin{bmatrix} \cos\phi & -\sin\phi \\ \sin\phi & \cos\phi \end{bmatrix} \begin{bmatrix} S_V & 0 \\ 0 & S_H \end{bmatrix} \begin{bmatrix} \cos\phi & \sin\phi \\ -\sin\phi & \cos\phi \end{bmatrix} = \\ \begin{bmatrix} S_h \sin^2\phi + S_V \cos^2\phi & (S_V - S_H) \cos\phi \sin\phi \\ (S_V - S_H) \cos\phi \sin\phi & S_h \cos^2\phi + S_V \sin^2\phi \end{bmatrix} \end{aligned} \quad (3.13)$$

After successfully applying the rotational matrix, a probability $p(\phi)$ function is used to describe the likely orientation of the scatterers:

$$\langle f \rangle = \int_0^{2\pi} d\phi f(\phi) p(\phi) \quad (3.14)$$

This allows for an averaging of the scattering effects over all possible orientations. After the scattering matrix is rotated and aligned, the second-order statistics are applied to analyze how the microwaves are interacting with the medium. These statistics help in quantifying the power and the phase correlation between polarization components. The YFD goes on to simplify the model under the assumption of thin cylindrical scatterers and assumes uniform distribution within $p(\phi)$. The combination of these steps have allowed for the

2.4.6 SAR Systems

Synthetic Aperture Radar (SAR) is a sophisticated remote sensing method, which uses the microwave portion of the EM spectrum to create high-resolution images of the Earth surface. Its origins can be

found in the works of Carl Wiley in the 1950s, where it was discovered that side-looking radar can increase its resolution by utilizing the Doppler spread of the echo signal. In the following years, significant developments occurred, including the launch of several rockets equipped with L-band SAR instruments and a lunar mission. These advancements culminated in the creation of the first purpose-built spaceborne SAR platform, SeaSAT-A, which was launched in 1978. Before the development of imaging radar, most high-resolution sensors were operated via a camera system, with sensors sensitive to emitted thermal radiation from the earth's surface or reflected solar radiation. The onset of SAR into the field of remote sensing brought about a completely unique approach to observing properties of the earth's surface. Since radar is an active sensor, transmitting its own radiation within the microwave region of the EM spectrum, this class of instruments allowed for the observation of properties of the earth's surface previously undetectable. Additionally, the new class of active sensors can operate without the input of light from the sun or thermal energy from the earth. Pairing this with the ability of microwaves to penetrate through the atmosphere regardless of the presence of water vapour, these sensors make for excellent all-conditions imaging systems.

One of the major drawbacks of microwave remote sensing is the size of the wavelength, which before the onset of SAR, would require platforms to contain apertures of significant size to get the resolutions achievable in optical sensors. For example, a platform orbiting at 800 km, using a standard wavelength such as L-band (approximately 25 cm), would require an aperture of approximately 8 km in length to achieve a modest resolution of 25 m. For context, the largest aperture created for a radar system was the land-based Duga array, which stretched over 700m, well below the 8 km aperture theoretically required to achieve a modest ground spatial resolution.

To address this hurdle, the introduction of a synthetic aperture was implemented, circumventing the need for kilometer-long apertures. The fundamental principles driving SAR are the Doppler effect

and microwave phase information, which allows the system to distinguish between objects at different distances and angles. By measuring the slight variations in frequency and phase as the radar platform moves, SAR can reconstruct a detailed image of the Earth's surface, achieving high resolution without requiring a physically large antenna. As SAR technology advanced, spaceborne sensors exhibit improved development from single-polarization to fully polarimetric SAR, unlocking a greater depth of information about the target's physical and geometric properties. Fully PolSAR platforms further enhance the ability to differentiate between different materials, analyze surface properties, and monitor changes in complex environments, making it an invaluable tool for environmental analysis.

Currently, there are eight active fully PolSAR platforms in operation around the world, each offering varying levels of imagery access and coverage areas. These platforms are critical for a wide range of applications, from environmental monitoring and disaster response to agricultural assessments and military surveillance. The capability to capture fully polarimetric data enhances the ability to distinguish between different types of surfaces and materials, providing detailed insights that are invaluable in numerous scientific and practical domains.

The ongoing development of new PolSAR platforms, such as DLR's TanDEM-L, ISRO's RISAT-2 and NASA/ISRO's NISAR, which are scheduled to launch in the coming years, underscores a continued investment in this class of remote sensing technology. The expansion of PolSAR capabilities demonstrates the growing acceptance of these systems for high-resolution, all-weather imaging, of environmental features.

Below is an overview of some key active PolSAR platforms, highlighting their operational timelines, wavelengths, resolutions, and repeat cycles:

Table 1: Polarimetric SAR platforms

Sensor Name	Operation Dates	Wavelength	Resolution	Repeat Cycle
ALOS-1	2006-2011	L-band	30x10m	46 days
Radarsat-2	2007-present	C-band	~3x3m-25x25m	24 days
TanDEM-X	2011-present	X-band	3x3m	11 days
ALOS-2- PALSAR-2	2014-present	L-band	3x3m-10x10m	14 days
SAOCOM	2018-present	L-band	10x10m	16 days
RCM	2019-present	C-band	3m-100m	12 days
BIOMASS	2021-present	P-band	60x50m	17 days
NISAR	2021-present	L-band	3m-20m	12 days

Chapter 3: Study Areas

This research focuses on two primary locations where a long time series of winter quad-polarized data were acquired that contained lakes with various depths, each with unique ecological, geological, and climatic characteristics. After we consider the two primary sites, we expand the scope of our research to include the Alaskan North Slope, Churchill, and the Lena Delta River while we explore additional wavelengths and their interactions with lake ice.

3.1 Old Crow Flats

The primary lake to be explored will be Old Crow Lake, located at 68.15° N, 148.23° W, which lies within the Old Crow Flats in the traditional territories of the Vuntut Gwitchin First Nations, Yukon Territory. This lake is part of a unique ancient lacustrine environment that was not glaciated during the Wisconsinan period but was once submerged beneath glacial Lake Old Crow. The lake, which spans 8.9 km in length and 6.3 km in width, is surrounded by mountains on three sides, forming a total shoreline of 38.6 km. The Old Crow Flats, covering approximately 617,000 hectares, showcase a topographical variety in a region predominantly characterized by mountainous terrain.

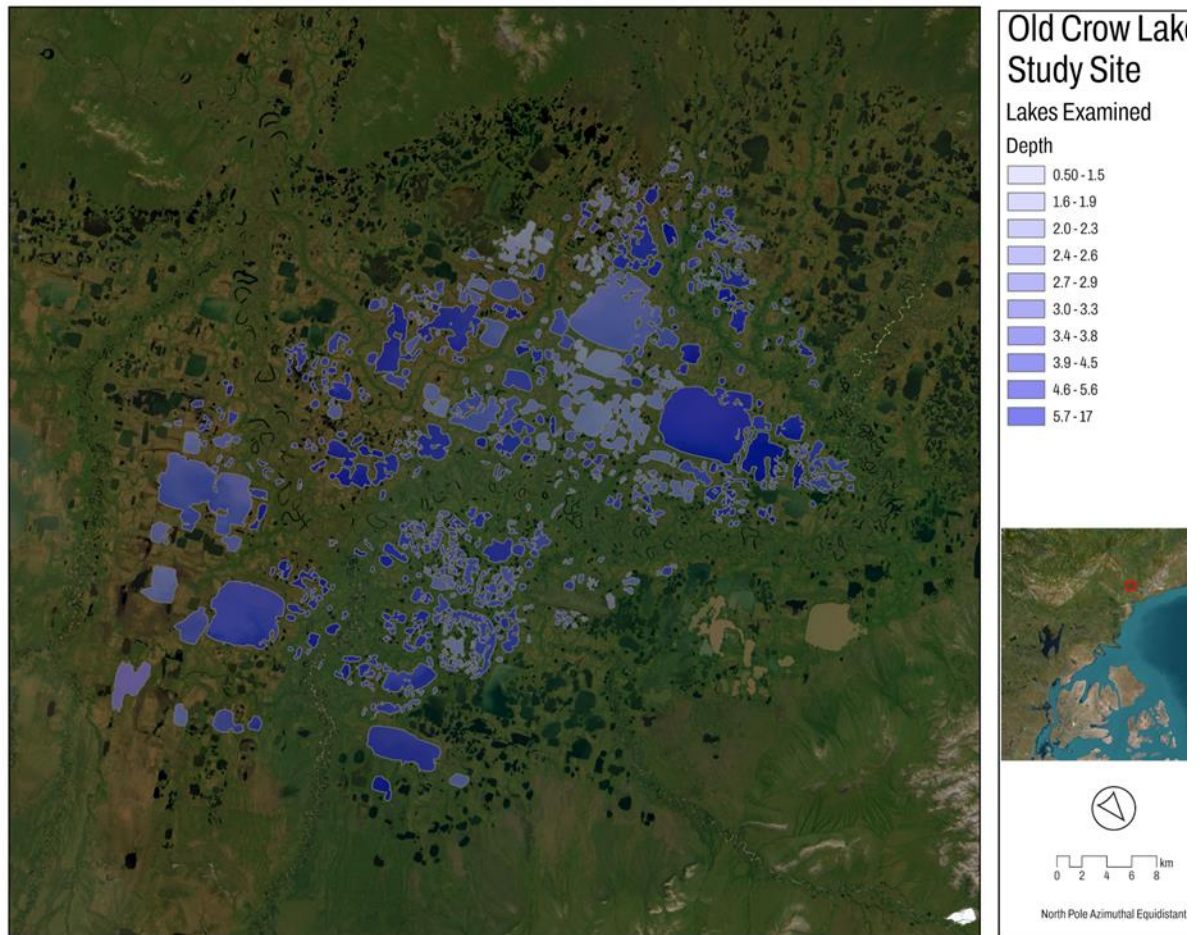


Figure 1: Location of Old Crow Lake in the Old Crow Flats, Yukon. Lakes Highlighted were examined in study

The climate in this subarctic zone features long, cold winters and brief, mild summers, with a mean annual air temperature recorded at -8.3°C between 1981 and 2010 (Environment Canada, 2012)). Despite low overall precipitation averaging 279 mm annually, the region's high latitude results in substantial snowfall, contributing to extended periods of frozen ground and ice cover. Thermokarst processes, prevalent during the early Holocene thermal optimum, have shaped much of the landscape, suggesting that many lakes here, including potentially Old Crow Lake, are remnants of

the expansive glacial Lake Old Crow. These lakes are typically shallow, flat-bottomed, and have an average depth around 1.2 meters, significant for studying limnological phenomena like the formation of tubular bubbles at the ice-water interface due to gas saturation (Gray and Alt, 2001). During the period of acquisition, the weather conditions in the Old Crow Flats were typical for this subarctic region, with temperatures frequently dropping below -30°C during the winter months (Environment Canada, 2011; Environment Canada, 2012). The winter of 2011/2012, in particular, was characterized by prolonged periods of extreme cold, with temperatures dropping below -40°C (Environment Canada, 2011; Environment Canada, 2012). The lowest temperature on record was -48.7 , and the maximum snow on ground depth of 20 cm (Environment Canada, 2011; Environment Canada, 2012).

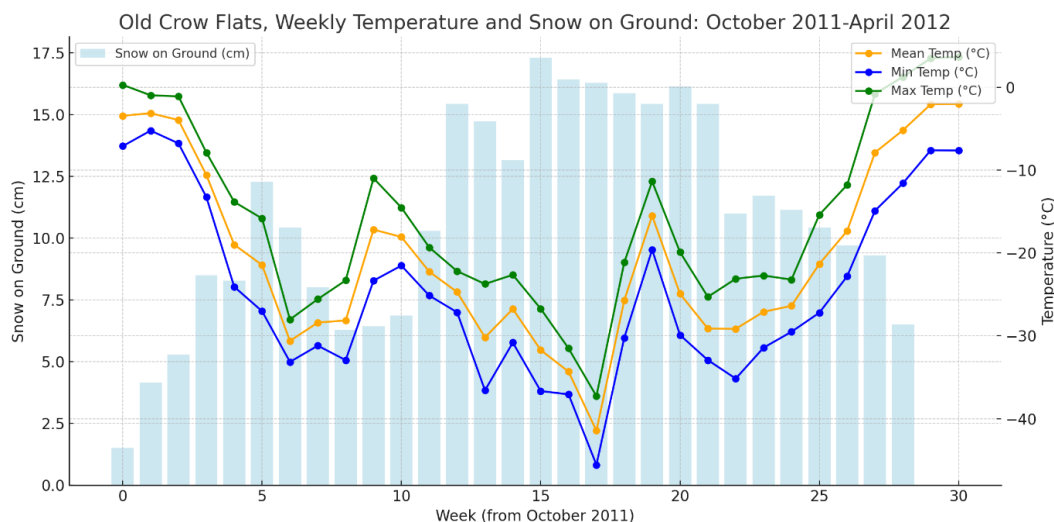


Figure 2: Mean temperatures and snow on ground for Old Crow Flats

3.2 Noel Lake

Noel Lake (68.53 N, 133.51 W) is positioned at an altitude of 89.9 meters above sea level. This lake, found to the east of the Mackenzie River Delta in the western Canadian Arctic, is not connected to the Mackenzie River's large network, despite its close proximity (Ogbebo et al., 2009; Ramlal et al., 1991). The area is characterized by continuous permafrost and the bedrock mainly

consists of carbonate and shale (Pienitz et al., 1997; Kokelj et al., 2005). Covering 30 square kilometers, Noel Lake reaches depths up to 18.3 meters (de Rham and Carter, 2009). The lake's edges slope gently towards the middle except on the western and northeastern sides, where the slopes are significantly steeper (Struger et al, 2018). Ecologically positioned in the Arctic tundra zone, the lake supports a rich variety of flora including grasses, dwarf shrubs, herbs, lichens, mosses, and sedges, all adapted to the brief and intense growing seasons of the area (Ogbebo et al., 2009).

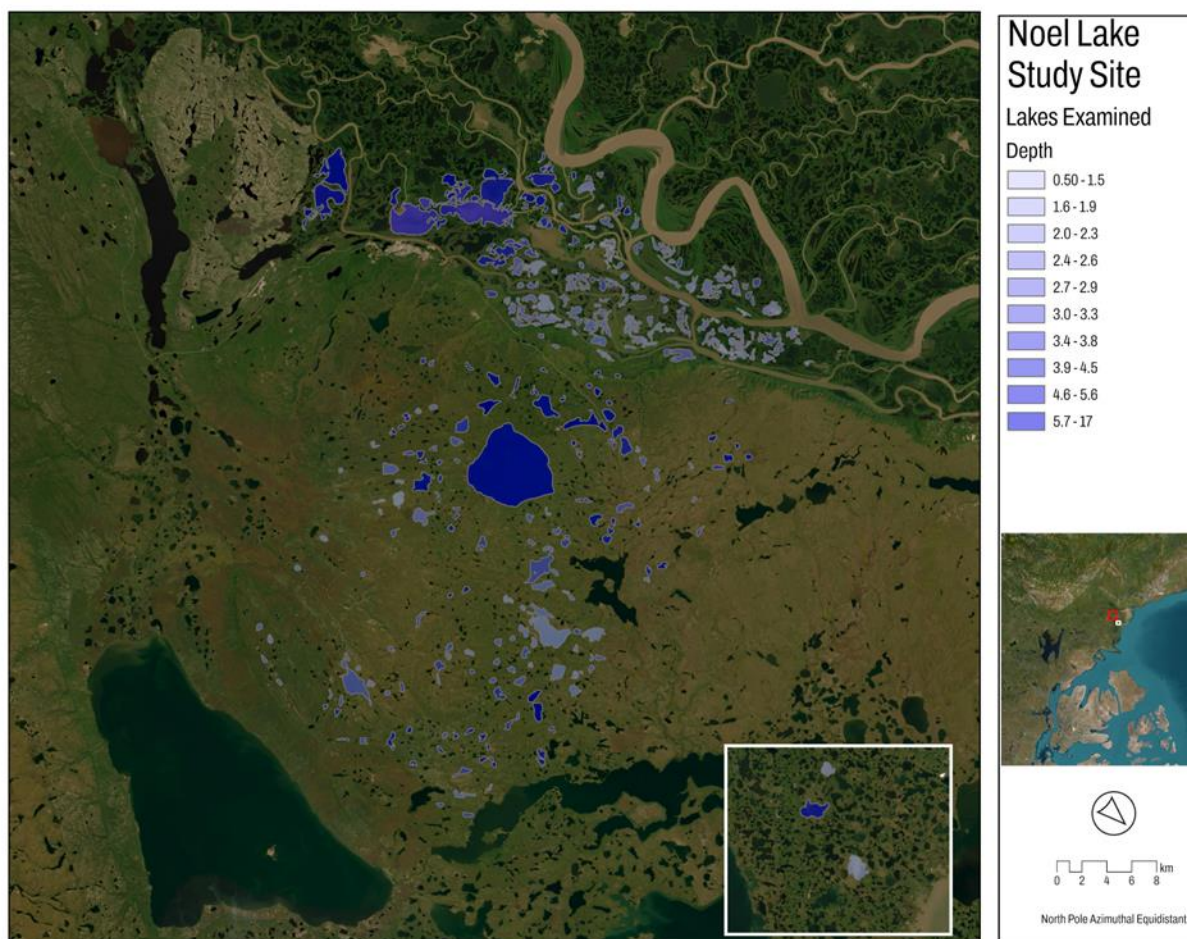


Figure 3: Noel Lake study area, near Inuvik, Northwest Territories. Lakes highlighted were examined in study.

The nearest weather station, which is about 21 kilometers away at the Inuvik airport, has recorded a mean annual air temperature of -7.22°C from 1992 to 2021, with January temperatures averaging -25°C and July temperatures at 14.44°C . During this period, the annual precipitation averaged 243.1 mm, mostly as summer rain (Environment Canada, 2021).

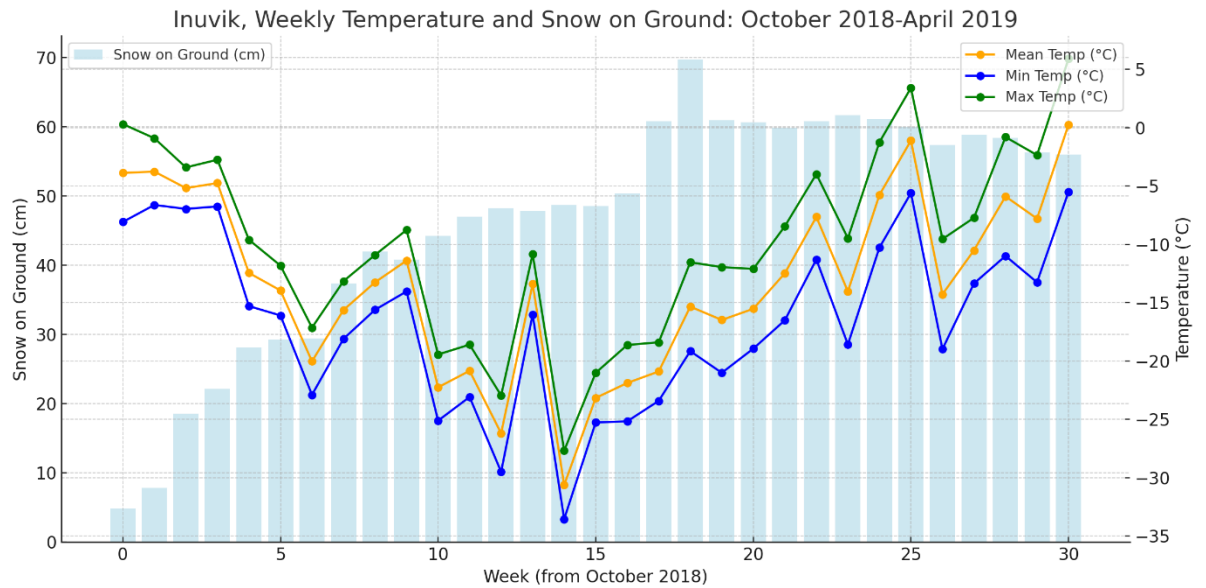


Figure 4: Noel Lake mean temperatures and snow on ground acquired by Environment Canada weather station located at 68.3594°N , 133.7294°W

3.3 Churchill

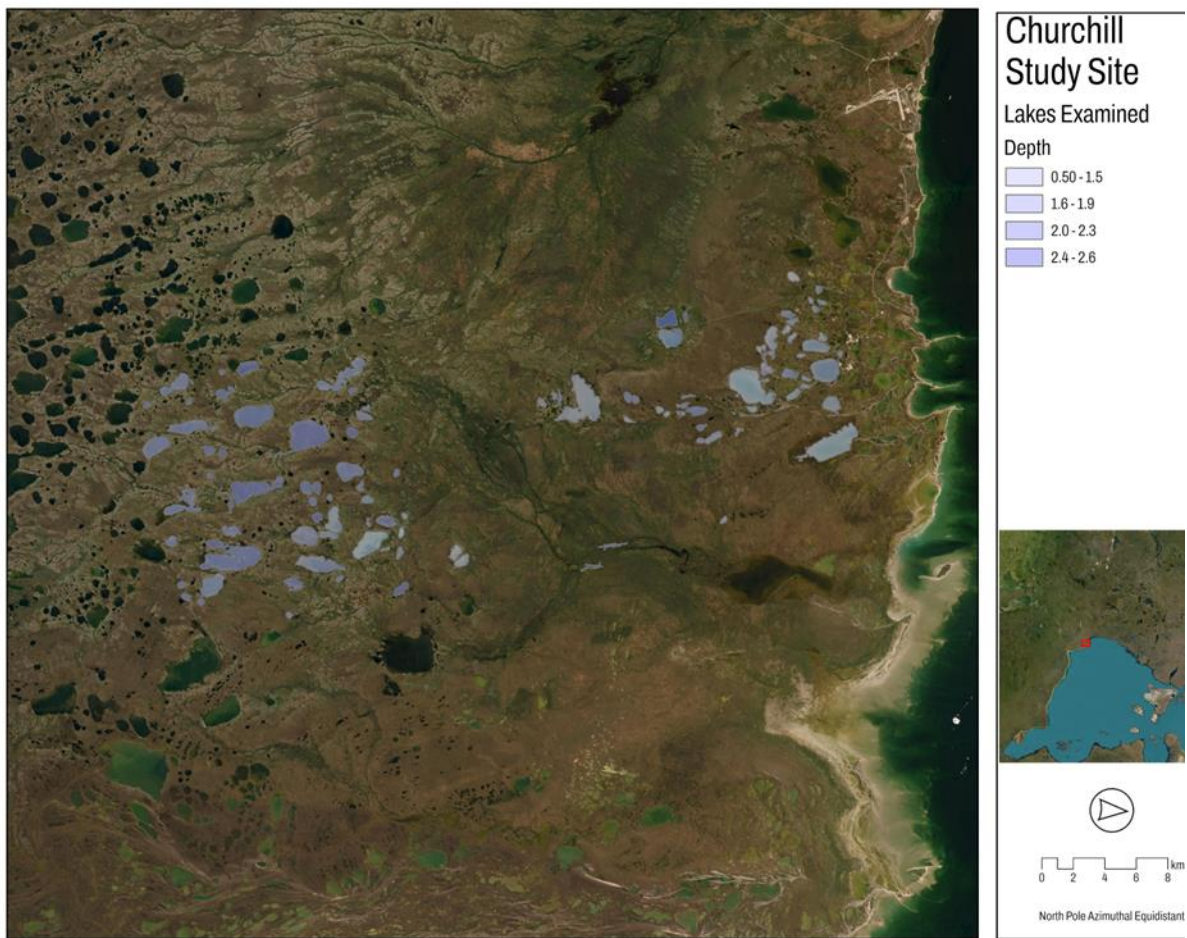


Figure 5: Capture area for Churchill, Manitoba. Lakes Highlighted were examined in study.

The first of our expanded study areas is located in Churchill, Manitoba, positioned at approximately 58.77° N, 94.17° W, on the southwestern shore of Hudson Bay. Churchill lies within the Subarctic climate zone, where long, harsh winters dominate the annual cycle, and is a part of the Hudson Bay lowlands (Scott et al., 1987). The region is characterized by its vast, flat terrain, interspersed with numerous lakes and wetlands that play a crucial role in the local hydrology and ecology (Scott et al., 1987). Churchill's environment is deeply

influenced by its location in the sub-Arctic, resulting in a climate where winter conditions prevail for the majority of the year. Mean annual air temperatures are recorded at around -7°C , but during winter months, temperatures frequently plummet below -30°C . The area experiences reduced hours of sunlight in the winter, which contributes to the persistence of ice and snow cover on the landscape. Annual precipitation is relatively low, averaging 400-500 mm, with the majority falling as snow, leading to substantial snow accumulation at shorelines and the formation of thick ice on the lakes. The lakes in the Churchill region, integral to the study, are typically shallow with consolidated ice cover from November through April. These lakes, remnants of ancient glacial activity, exhibit flat-bottomed topography and often have depths that range around 1-2 meters (Lafleur et al., 1997). The surrounding landscape, shaped by permafrost and seasonal thawing, is dotted with numerous small, isolated lakes and ponds, which become interconnected during the brief summer thaw (Hansell et al., 1983).

3.4 Lena River Delta

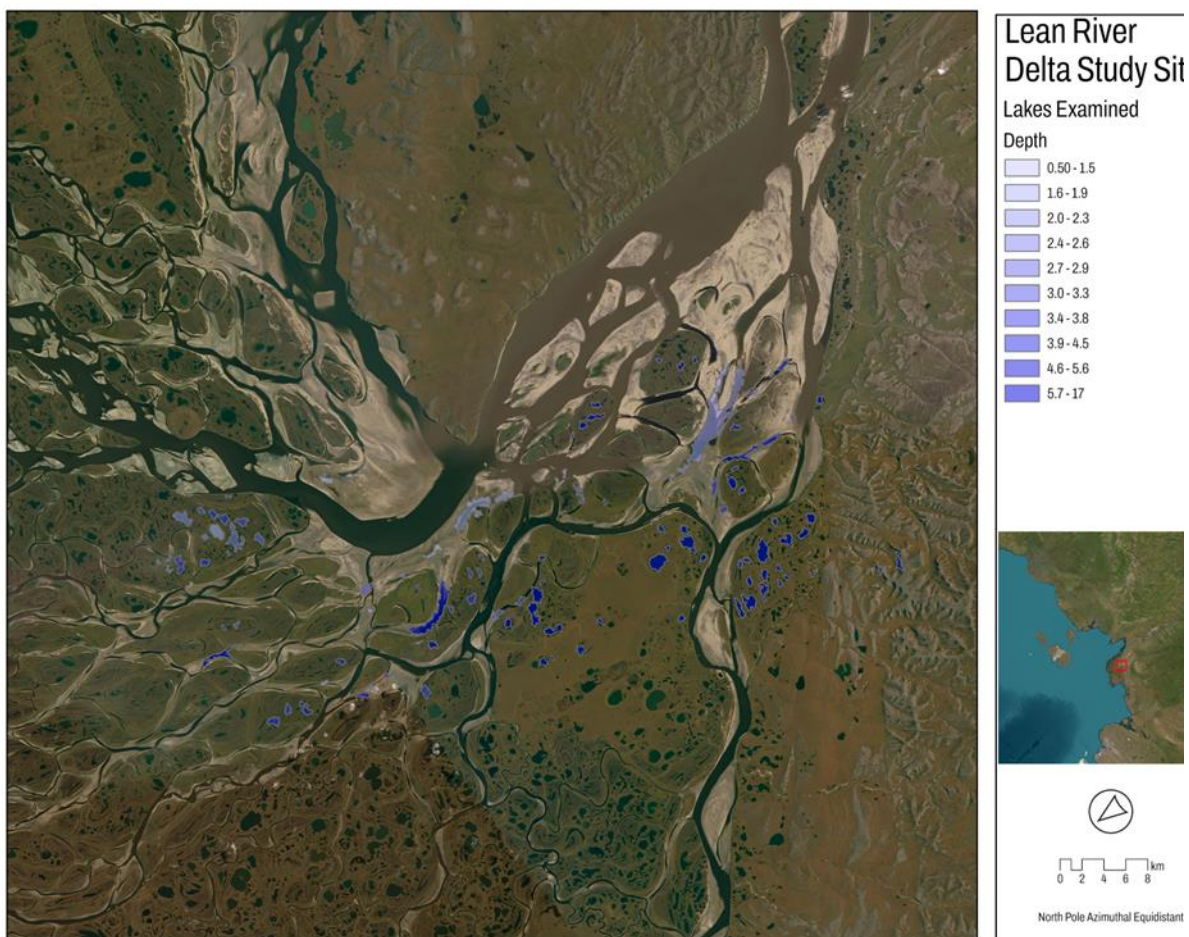


Figure 6: Capture area for Lena River Delta Study Area. Lakes highlighted were used in study.

The second of our secondary study areas will focus on a subset of the Lena River Delta, situated at approximately 72.69° N, 127.13° E, within the Siberian Arctic. The Lena River, recognized as the tenth longest natural river in the world, flows through this delta before emptying into the Laptev Sea (ESA, 2019). The delta, spanning around 29,000 km², lies within a vast permafrost region and is characterized by a complex network of river channels, lakes, and wetlands (ESA, 2019). The delta's intricate landscape, largely shaped by seasonal flooding, forms part of a critical ecological zone that supports a diverse range of Arctic wildlife (Lutjen et al, 2023). This

region, dominated by yedoma—a type of permafrost rich in organic matter and ice—remained largely unglaciated during the last glacial period, contributing to its unique geomorphological features (Lutjen et al, 2023). The delta's location within the Arctic Circle results in extreme climatic conditions, with long, harsh winters and brief, mild summers. The Lena River itself typically freezes from early December to late April, with ice thawing and peak river flow occurring in June. The mean annual air temperature in this region hovers around -12°C , reflecting the severe cold characteristic of Siberia (Lutjen et al, 2023). Annual precipitation is low, averaging 200-300 mm, but substantial snowfall and thick ice cover persist for most of the year.

3.5 Alaska North Slope



Figure 7: Capture area for the Alaska North Slope, near Utqiagvik, Alaska. Lakes highlighted were used in study.

The last study area of our secondary studies areas is centered on Utqiagvik, Alaska, formerly known as Barrow, located at approximately 71.29° N, 156.79° W, on the northernmost tip of the United States. Utqiagvik lies within the Arctic coastal plain, where the landscape is dominated by permafrost, low-lying tundra, and a multitude of lakes and ponds (Hinkel et al, 2003). As the northernmost community in the U.S., Utqiagvik experiences some of the most

extreme winter conditions on the planet, making it a prime location for studying Arctic lake ice processes. Utqiagvik's climate is typified by long, bitterly cold winters, with temperatures frequently dropping below -30°C from December through March (Hinkel et al, 2003). The region is subject to polar night, a period of continuous darkness that lasts from mid-November to late January, during which the absence of sunlight leads to persistent freezing conditions (Hinkel et al, 2003). The mean annual air temperature in Barrow is approximately -12°C , reflecting the extreme cold that dominates the region for much of the year (Hinkel et al, 2003). Utqiagvik has a moderate level of precipitation, averaging 115-150 mm as liquid precipitation and 740mm of snow fall annually, the large amount of snowfall contributes to thick ice cover on the lakes and ponds (Hinkel et al, 2003). The lakes in the Utqiagvik region are combination of fasting and shallow lakes, a result of thermokarst features formed by the thawing of ice-rich permafrost (Surdu et al, 2014). During the brief Arctic summer, these lakes thaw partially, but for most of the year, they remain solidly frozen, encapsulating sediments and gases that are slowly released during the thaw (Surdu et al, 2014). Winter conditions in Barrow are severe and prolonged, with snow and ice cover persisting well into the spring. The thick ice cover on the lakes, combined with the underlying permafrost, makes this region particularly sensitive to climate change, as even slight temperature variations can have significant impacts on the local environment (Surdu et al, 2014). Utqiagvik's extreme Arctic conditions provide a unique opportunity to study the impacts of long, harsh winters on lake systems, contributing valuable insights into the broader understanding of Arctic environmental change.

Chapter 4: Data and Methods

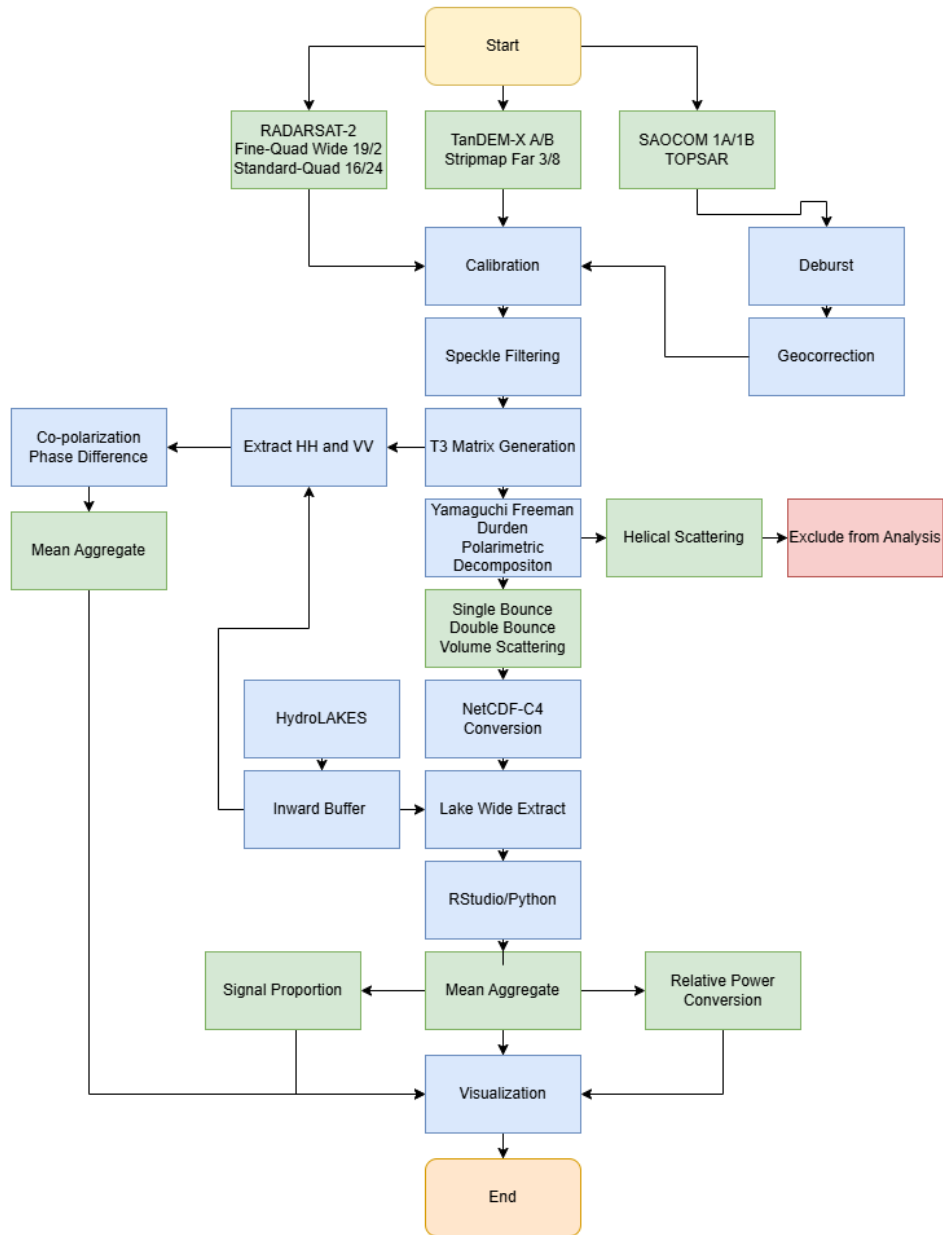


Figure 8: Methods Flow Diagram

4.1 SAR Acquisitions

In this study, SAR acquisitions are sourced from TanDEM-X, RADARSAT-2, and SAOCOM, a collection of PolSAR platforms, capturing microwaves in X-band (9.65 GHz, 3.1cm), C-band (5.405 GHz, 5.6 cm), and L-band (1.275 GHz, 23.5cm).

With shortest wavelength observed in this study at 3.1cm (9.65 GHz), Tandem-X was launched by DLR in 2010 and is designed for interferometric applications. Operating in tandem with its twin satellite TerraSAR-X in a constellation, TanDEM-X captures high-resolution radar imagery, with two modes capable of capturing polarimetric acquisitions, Spotlight and StripMap. Stripmap mode acquisitions are explored in this study.

RADARSAT 2, launched by the CSA, is renowned for its fully polarimetric Synthetic Aperture Radar (SAR) capabilities, with a multitude of beam modes available to acquisitions and a wide area of coverage. Operating within the C-Band spectrum, it centers at the frequency of 5.405 GHz, with a corresponding wavelength of 5.6 cm. This satellite system is adept at capturing imagery in single, dual, and quad-polarization modes. RADARSAT 2 offers a selection of four beam modes for Polarimetric captures: fine, standard, fine wide, and fine standard.

SAOCOM, developed by CONAE (Argentina's National Space Activities Commission), operates at a frequency of 1.275 GHz, with a wavelength of 23.5 cm. This platform has two beam modes with polarimetric capabilities, TOPSAR and StripMap. For this study, the TOPSAR beam mode will be utilized, offering a balance between wide coverage and high-resolution imagery, making it ideal for polarimetric decomposition.

Table 2: SAR acquisitions utilized in study

Beam Mode	Sensor	Date of Acquisition	Number of Captures	Incidence Angles
Fine Quad 2 Wide	RADARSAT 2	October 2018- April 2019	10	37-40
Fine Quad 19 Wide	RADARSAT 2	October 2018- April 2019	10	19-22
Standard Quad 16	RADARSAT 2	October 2018- April 2019	18	34-37
Standard Quad 24	RADARSAT 2	October 2018- April 2019	14	42-44
TOPSAR Quad- Pol	SAOCOM 1B	November 2020- April 2020	7	27-35
TOPSAR Quad- Pol	SAOCOM 1A	November 2022- April 2023	11	27-25
Stripmap Far 3 Quad	TANDEM-X A	January 2015- April 2015	18	33-34
Stripmap Far 8	TANDEM-X B	January 2015- April 2015	14	22-24

4.2 Polarimetric Data

Drawing from three different platforms, over a several band types, this study will be positioned to offer a comprehensive examination into microwave lake ice behaviour. However, it is pertinent to note that polarimetric data from across each satellite is less prevalent compared to dual or single polarization. This results in a less temporally coherent dataset, dispersed across multiple locations and beam mode types. For each of our study sites, we have endeavored to collect all temporally coherent quadrature polarized data that is available. This data was filtered to select beam modes that provide a time series which best capture the behaviour of lakes as winter progresses and covering the same area in each capture.

Consequently, for our primary analysis, we have identified four pertinent time series – two for Noel Lake and two for Old Crow Lake. Specifically, for Old Crow Lake, standard polarimetric beam modes 24 and 16 were acquired, spanning October 2011 to May 2012. For Noel Lake, fine polarimetric beam modes 2 and 19 were acquired, covering the period from October 2018 to May 2019. The Old Crow acquisitions exhibit incidence angles ranging between $35.4\text{--}42.8^\circ$ and a resolution between $19.2\text{--}23.6\text{m}$. Conversely, the Noel Lake images feature incidence angles from $19.7\text{--}38.3^\circ$ degrees, with a spatial resolution spanning $8.9\text{m}\text{--}15.4\text{m}$.

In the second phase of this study, we introduce data from SAOCOM and TanDEM-X, alongside new study sites at Utqiagvik, Lena River Delta, and Churchill. SAOCOM, introducing L-Band into our analysis, will cover the same areas as RADARSAT-2, specifically Noel Lake and Old Crow Flats. For the Old Crow Flats area, the time series from November 2020 to April 2021 was captured. For Noel Lake and its surrounding area, the time series from October 2022 to April 2023 was captured. In both cases, the TOPSAR beam mode was used, providing a spatial resolution of 38.6m to 41.4m and incidence angles ranging from 27.2 to 35.5 degrees.

TanDEM-X, operating in X-Band, has coverage of the regions surrounding Utqiagvik, Lena River Delta, and Churchill. All imagery was acquired during the winter of 2014-2015 during the interferometric DEM acquisition phase of the sensor. For Utqiagvik, the imagery spans from December to March, with a spatial resolution of 2.8m and incidence angles between 27.4 and 29.1 degrees. The Lena River Delta series, captured from December to March, offers a spatial resolution of 3.6m and incidence angles between 23.7 and 25.6 degrees. Finally, the Churchill site presents a shorter time series from January to March, with a spatial resolution of 2.4m and incidence angles ranging from 33 to 34.5 degrees.

4.3 Polarimetric Decomposition

The initial phase of this study involves the application of the Yamaguchi-Freeman-Durden (YFD) Polarimetric Decomposition to each acquisition. The form of this decomposition does not change between each platform. This decomposition was chosen because it allows for a robust classification of scattering mechanisms which is essential for understanding backscattering dynamics of lake ice. To conduct the YFD decomposition, the Sentinel Application Platform (SNAP) was selected due to its extensive documentation on polarimetric processing and its ability to handle datasets from multiple sensors, ensuring methodological consistency across different platforms. The methodological steps undertaken adhere closely to the guidelines found in the Sentinel-1 Toolbox documentation for polarimetric decomposition, as this ensures standardization and reproducibility of results.

The analysis began by acquiring the PolSAR data from Earth Observation Data Management System (EODMS) for RADARSAT-2, the Earth Observation Centre Portal (EOWEB) for Tandem-X, and the National Apace Activities Commission (CONAE) for SAOCOM. The data acquired is all fully polarimetric, and Single Look Complex (SLC). SLC data is required because it retains both the

amplitude and phase information of the original microwave signal, which is critical for polarimetric decomposition. Single look refers to the image being absent of any averaging or multi-looking, which is often applied to higher levels of pre-processed microwave imagery. Complex indicates that the data stored in each pixel is stored as complex numbers, retaining both the in-phase and quadrature components of the microwave imagery. The complex information is required to do any sort of polarimetric studies. Once the all of the required imagery was acquired and organized the data is brought into the SNAP framework to begin the polarimetric decomposition process.

The first step is the calibration process, which is platform-dependent and completed within SNAP. This calibration process utilizes lookup tables, incidence angles, calibration constants, and range spreading loss, all of which are stored within each acquisition's metadata. Calibration is necessary to ensure that pixel values accurately reflect the true backscatter intensity, removing radiometric biases introduced during image acquisition. Without proper calibration, comparing images across different sensors, time periods, or environmental conditions would be less reliable and robust.

Once the images have been calibrated, a polarimetric matrix needs to be generated. This results in each pixel having a T3 matrix taking the form of:

$$\left\langle \frac{1}{2} \begin{bmatrix} \langle |S_{HH} + S_{VV}|^2 \rangle & \langle (S_{HH} + S_{VV})(S_{HH} - S_{VV})^* \rangle & 2\langle (S_{HH} + S_{VV})S_{HV}^* \rangle \\ \langle (S_{HH} - S_{VV})(S_{HH} + S_{VV})^* \rangle & \langle |S_{HH} - S_{VV}|^2 \rangle & 2\langle (S_{HH} - S_{VV})S_{HV}^* \rangle \\ 2\langle S_{HV}(S_{HH} + S_{VV})^* \rangle & 2\langle S_{HV}(S_{HH} - S_{VV})^* \rangle & 4\langle |S_{HV}|^2 \rangle \end{bmatrix} \right\rangle \quad (3.14)$$

The T3 matrix is required for the calculation found within the polarimetric decomposition model.

Before applying the decomposition, a speckle filter is implemented to reduce noise while maintaining the statistical properties of the polarimetric information. The Refined Lee filter was selected for this study, as it effectively suppresses speckle while preserving the tone and structural details necessary

for accurate decomposition results. This ensures that the volume, double-bounce, and single-bounce scattering contributions remain consistent with the underlying physical properties of the terrain.

After setting up the imagery by completing the calibration, speckle filtering, and T3 matrix generation, the YFD decomposition is applied. The Yamaguchi-Freeman-Durden 4 Component Polarimetric Decomposition employs an improved version of the Freeman-Durden 3 Component Polarimetric Decomposition. The YFD calculates each scattering mechanism power using equations 3.15 to 3.18. Surface scattering (P_s) was calculated using the surface scattering coefficient (fs), weighted by the complex-unknown parameter term β , as $P_s = fs (1 + |\beta|^2)$. Similarly, double-bounce scattering (P_d) was derived using the coefficient fd and weighted by the complex-unknown parameter term α , as $P_d = fd (1 + |\alpha|^2)$. Volume scattering (P_v) was calculated directly from the volume coefficient (fv), and helix scattering (P_c), was directly calculated for the helical coefficient (fc). The total scattering power (P_t) was then determined as the sum of these components, $P_t = P_s + P_d + P_v + P_c = \langle |SHH|^2 + 2|SHV|^2 + |SVV|^2 \rangle$. These calculations allowed for the decomposition of the total backscattered signal into individual scattering contributions for analysis.

$$P_s = fs(1 + |\beta|^2) \quad (3.15)$$

$$P_d = fd(1 + |\alpha|^2) \quad (3.16)$$

$$P_v = fv \quad (3.17)$$

$$P_c = fc \quad (3.18)$$

$$P_t = P_s + P_d + P_v + P_c = \langle |SHH|^2 + 2|SHV|^2 + |SVV|^2 \rangle \quad (3.19)$$

For the purpose of this study, helical scattering can be removed from consideration as it is not seen in natural settings and will obfuscate the results of the study. We still use the YFD four component, as opposed to the FD or the YFD three component, as its treatment of modeled volume scattering is considered state-of-the-art.

Once the major analysis was completed, all 112 images were converted to NetCDF-C4 files for input into a Python extraction program. NetCDF-C4 was chosen due to its efficient storage structure and compatibility with large datasets, facilitating rapid access and analysis. The extraction process utilized a shapefile from HydroLAKES, as the source of lake polygons (Lehner et al. 2008). HydroLAKES was selected because it provides globally standardized lake boundary data, ensuring consistency in polygon selection. An inward buffer, three times the size of the average spatial resolution of each platform was applied to each polygon to minimize the effects of mixed pixels, ensuring that only lake ice was included in the extracted data. Additionally, the HydroLAKES shapefile was trimmed to include only lakes that were fully present in all images of a time series. This refinement resulted in three sets of polygons, one for each sensor, each inwardly buffered and consistently present across all captures, for use in the extraction program. The program operates by iterating through each lake in the shapefile, extracting each pixel captured within the polygon from the NetCDF-C4 files. The variables extracted include the lake identification number, surface-bounce power, double-bounce power, volume scattering power, and average lake depth. This results in a series of csv files, which are further manipulated in R-Studio, to display the results of the study

This advanced decomposition technique excels at separating the complex interactions of microwave backscatter signals of natural phenomena. The primary goal of the YFD is to quantify the relative contributions of each backscattering mechanism observed at the sensor. By determining the relative proportions of different scattering mechanisms, such as surface, double-bounce, volume and scattering, we can draw significant insights into the physical and structural properties of the lakes ice-water interface. A key aspect of this study is to discover whether the distinctive characteristics of shallow lakes, influence the backscattering mechanisms in a discernible manner. We anticipate that the shallowness of Old Crow Lake will form tubular bubbles, which cannot form in the deeper Noel

Lake. This contrast is expected to shed light on the interaction microwaves and ice particularly in the context of Subarctic freshwater lakes. By meticulously parsing the backscatter power data and correlating these findings with the known geographical and physical characteristics of each lake, we aim to elucidate the dominant backscattering mechanisms at play at the ice-water interface of lakes in the Subarctic and Arctic.

4.4 Co-Polarization Analysis

An additional parameter that provides evidence of interactions at the ice-bottom versus double-bounce or volume scatter is to examine the co-polarization phase difference. Utilizing the same data, calibration, and matrix generation steps, we use the co-polarization elements of the T3 matrix to calculate the co-polarized phase difference to observe whether or not a double-bounce interaction is occurring at the lake ice. This is done to complement the finding of derived from the polarimetric decomposition, as it is another method of observing the potential presence of double bounce scatter in lake ice to impute the effects of tubular bubbles on overall backscatter. Once completed, Noel Lake and Old Crow time series are examined in R, as supplementary findings.

This multifaceted approach, combining Polarimetric Decomposition, and Co-Polarization analysis, aims to provide a robust record of scattering interactions for lakes of various sizes and depth to improve the understanding of microwave interactions with the unique environments of Sub-Arctic freshwater lakes.

4.5 Methodological Limitations and Uncertainty

After a comprehensive analysis of polarimetric SAR data an acknowledgment of methodological limitations is required, which arises from multiple factors inherent to microwave imaging, remote sensing and the processing chain of microwave acquisitions. While this study employs rigorous methodologies to mitigate sources of error, the inherent limitations of SAR

acquisitions, speckle noise, and incidence angle variability introduce uncertainties that must be considered when interpreting the results.

Speckle is an inherent characteristic of coherent imaging systems such as SAR, manifesting as grainy noise that can obscure fine details and distort backscatter values. This noise originates from the constructive and destructive interference of microwaves reflecting off multiple scatterers within a resolution cell. Speckle can significantly impact polarimetric decomposition by introducing artificial variations in scattering mechanisms, potentially skewing the relative contributions of surface, double-bounce, and volume scattering. To mitigate speckle, this study applies the Refined Lee filter, chosen for its balance between noise suppression and preservation of the on the ground interaction. However, speckle filtering itself introduces a degree of uncertainty, as any smoothing operation may suppress genuine scattering characteristics and alter the statistical properties of the backscatter signal. To account for this, speckle filtering is applied consistently across all acquisitions and study areas, ensuring uniformity in preprocessing and reducing bias across the different sensors and study sites.

The incidence angle, defined as the angle between the microwave signal and the surface, plays a crucial role in determining backscatter intensity. Variations in incidence angle can lead to considerable differences in observed scattering mechanisms, even for the same surface conditions. Given that this study incorporates data from multiple SAR platforms, each with varying beam modes and incidence angles, these variations introduce an additional layer of uncertainty. To reduce the influence of incidence angle variation, all acquisitions selected for a time-series were constrained to the same or similar incidence angle. However, residual effects of incidence angle differences on backscatter values remain a consideration in the interpretation of results.

While methodological consistency and preprocessing techniques help control for these sources of uncertainty, it is essential to interpret results with an awareness of their potential

limitations. As well, since this study is considering an aggregate of values, the influences of speckle will be more diminished than if only one pixel from each lake was considered. The interplay between speckle noise, incidence angle variation, and the chosen decomposition model may introduce localized inconsistencies in backscatter classification. Therefore, trends in the data are analyzed across multiple acquisitions to discern persistent patterns rather than relying on individual images.

Chapter 5: Results

5.1 Old Crow

In the examination of fully polarimetric acquisition of Old Crow Lake, spanning October 2011 to March 2012, for standard beam mode 24 and 16, (with average incidence angles of 34 and 44, respectively), we observe patterns of single-bounce, double-bounce, and volume scattering mechanisms from the polarimetric decomposition. Our analysis, grounded in average signal power (measured in decibels), relative power, and signal proportionality, leverages the Yamaguchi Freeman Durden decomposition technique for a nuanced exploration of the temporal evolution of each scattering mechanism's characteristics throughout the winter 2011/2012 winter season.

Standard Beam Quad Mode 24

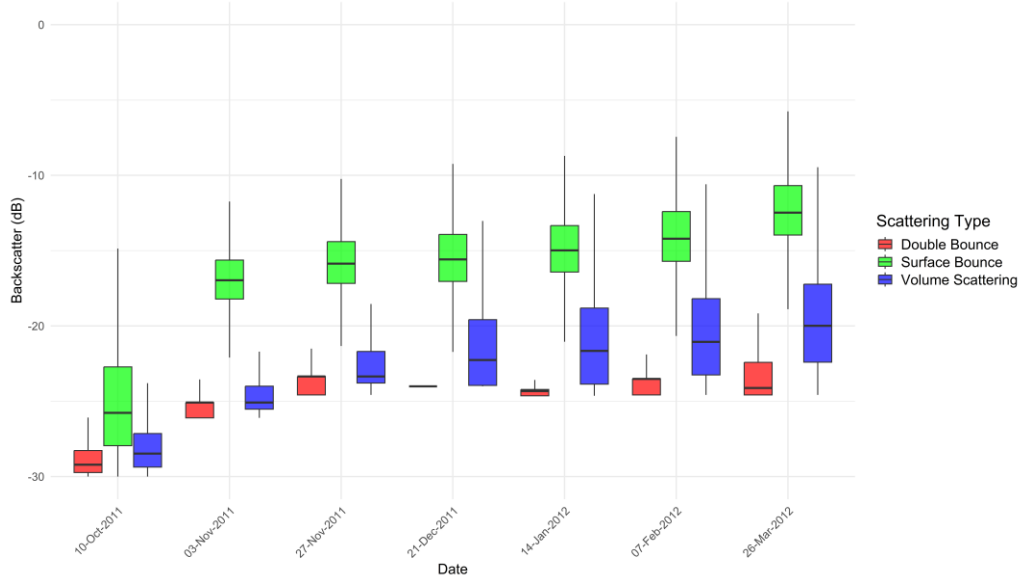


Figure 9: Old Crow, RADARSAT 2 Standard Quad-Pol Beammode 24. Median signal power

Beginning with standard beam mode 24, the temporal trend in average signal power for single-bounce scattering exhibits a progressive increase in signal strength throughout the observation period. The initial acquisition starting at the lowest signal power of -25.68 dB in October 2011, with each month increasing in power as winter progresses resulting in a significant escalation in observed power, culminating in a peak signal strength of -12.16 dB by March 2012 (Figure 9). This increasing trajectory for single bounce suggests enhanced backscatter from single surface interface, potentially indicative of modifications of interface roughness conditions. The relative power of single-bounce scattering increased linearly, evolving from 0.0027 in October 2011 to 0.061 by March 2012. Concurrently, the fraction of the total microwave signal ascribed to single-bounce scattering followed a similar upward trajectory, increasing from 53.52% in October 2011 to 79.65% by March 2012 (Figure 10).

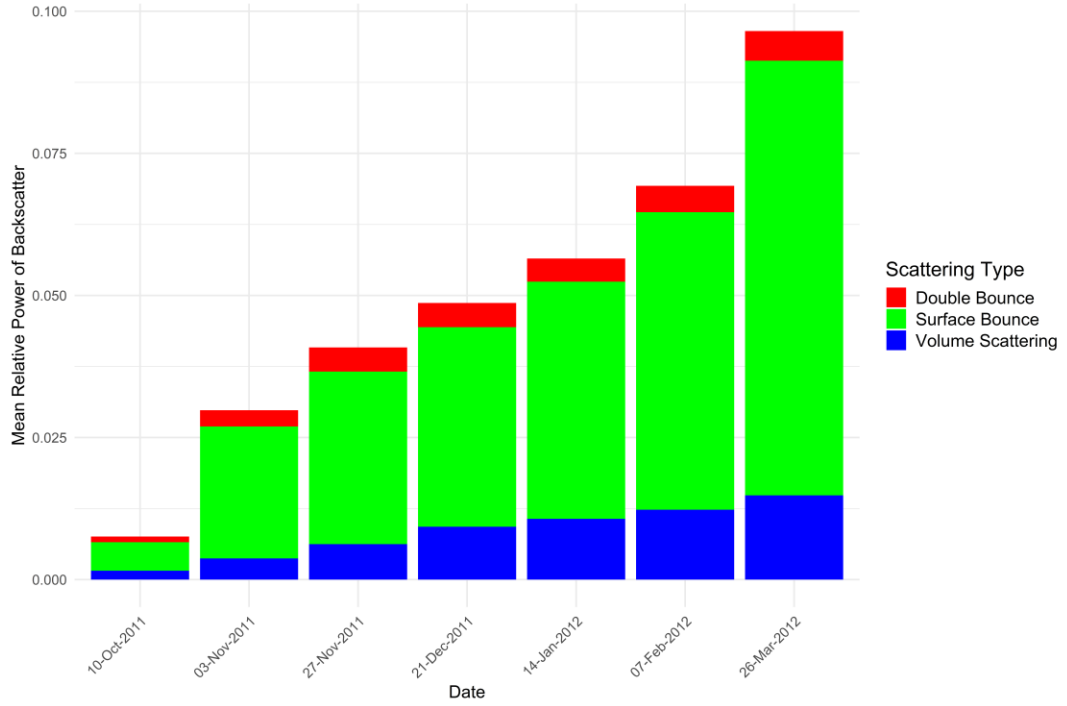


Figure 10: Old Crow, RADARSAT-2 Standard Quad-Pol Beammode 24. Average relative power

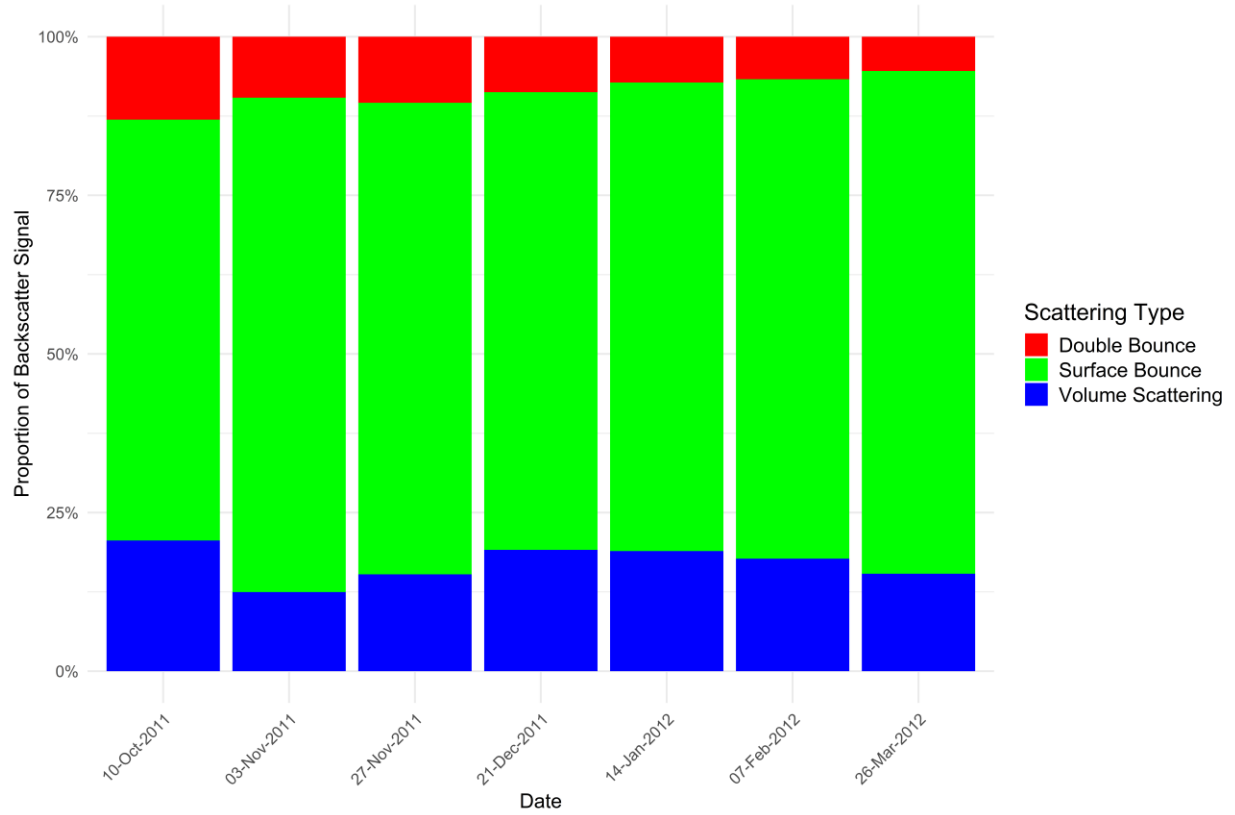


Figure 11: Old Crow, RADARSAT-2 Standard Quad-Pol Beammode 24. Average proportion of signal

Conversely, double-bounce scattering exhibited a less pronounced positive trend in average signal power, from -30.12 dB in October 2011 to -23.26 dB by March 2012, approaching the noise floor of the sensor of -28 dB for co-pol data (Hannevik, 2011). This trend might signify a reduced interaction between the microwave signal and orthogonal vertical structures with a flat surface. The relative power of double-bounce scattering, despite an increase from 0.00097 in October 2011 to 0.0047 by March 2012, necessitates contextual interpretation within the overall signal composition, suggesting a diminution in the prominence of double-bounce mechanisms relative to single-bounce

scattering. The signal proportion attributable to double-bounce scattering diminished over time, from 19.29% in October 2011 to 6.17% in March 2012.

Volume scattering's average signal power experienced an uptick from -28.62 dB in October 2011 to -19.66 dB by March 2012, indicative of an increased signal strength from mechanisms within this category, likely attributable to inclusions of scatterers stemming from snow and superimposed ice structures. The relative power for volume scattering increased, starting at 0.0014 in October 2011 and ascending to 0.011 by March 2012. The proportion of the total microwave signal linked to volume scattering displayed variability, yet generally trended downwards from 27.19% in October 2011 to 14.17% by March 2012. These result of the polarimetric decomposition for these captures showed that the majority of the returned signal, by a large margin, was single bounce, followed by volume scattering.

Standard Beam Quad Mode 16

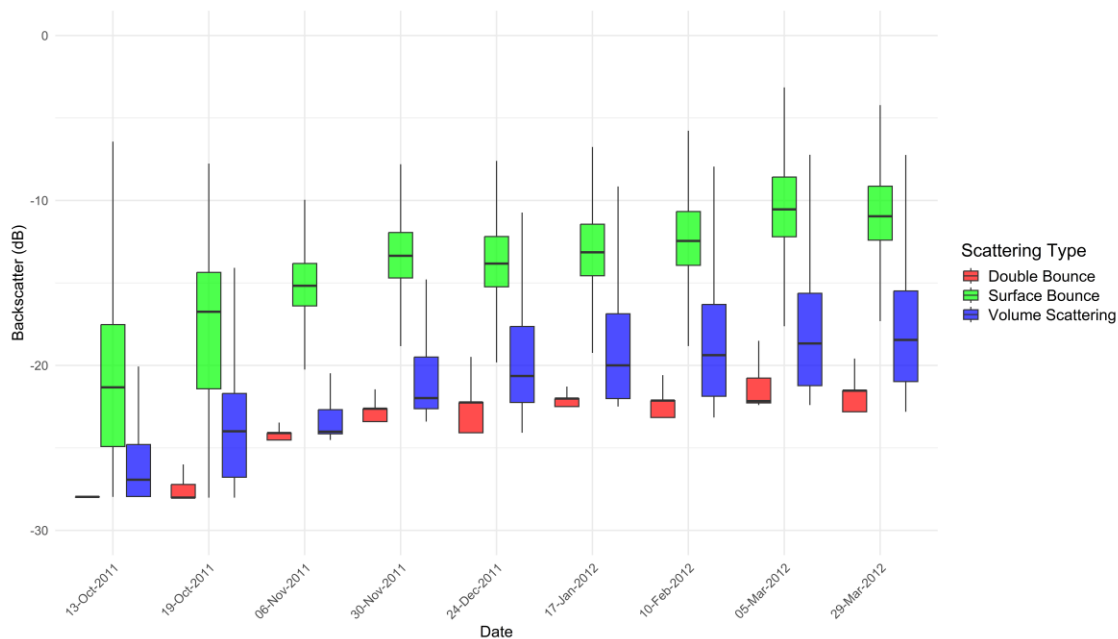


Figure 12: Old Crow, RADARSAT 2 Standard Quad-Pol Beam mode 16, median backscatter power

For the Standard beam 16 acquisitions (Figure 11), spanning from October 2011 to March 2012, our observations reveal increases in the average signal power for single-bounce scattering consistent with Standard beam 24, with the average values starting at -21.04 dB in October 2011 and increasing to -10.58 dB by March 2012, consistent with increasing surface bounce power throughout the season shown in SQ24. The relative power for single-bounce scattering witnessed a substantial growth throughout the observation span, from 0.0079 to 0.088. The proportion of the microwave signal attributed to single-bounce scattering increased from 65.23% in October 2011 to 79.23% by March 2012, consistent with proportional increases in surface bounce shown in SB 24.

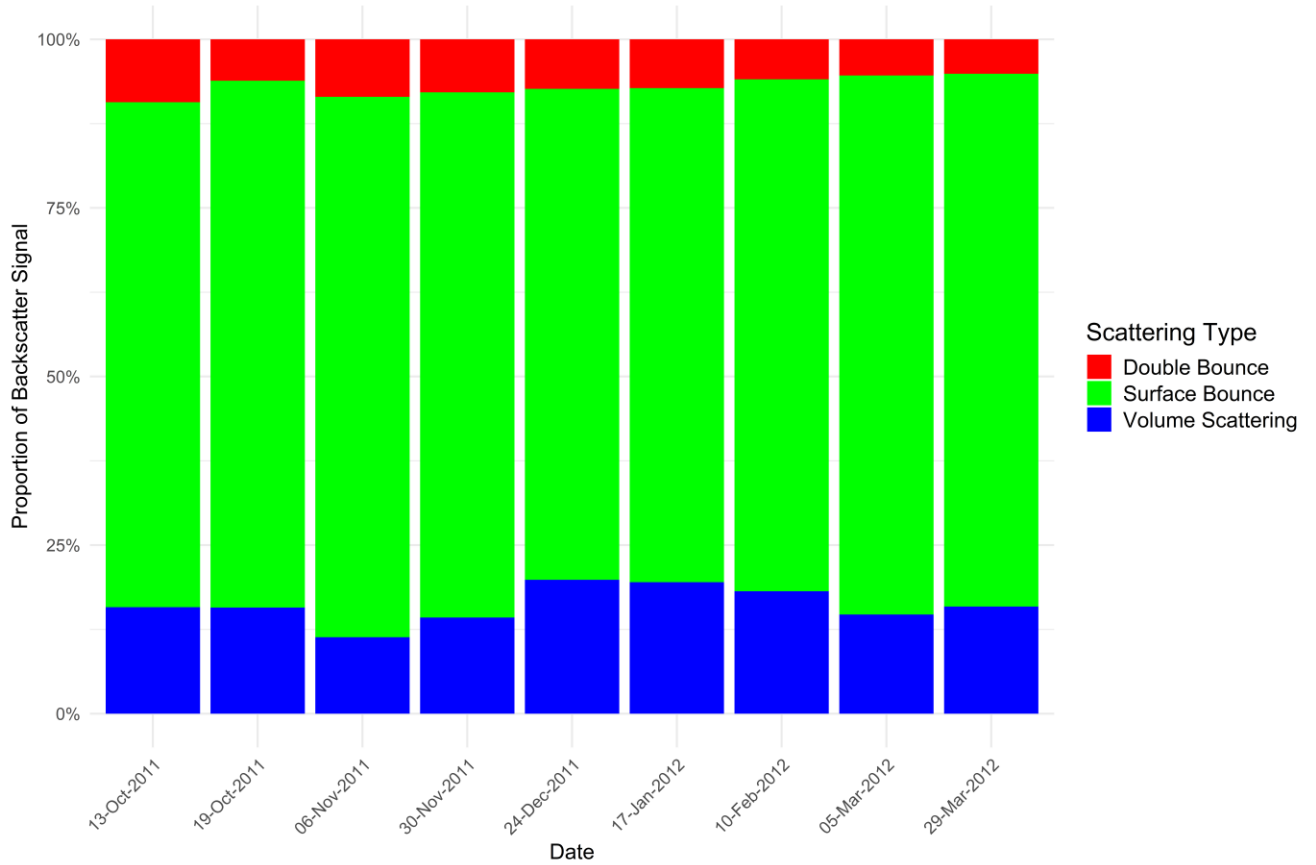


Figure 13: Old Crow, RADARSAT 2 Standard Quad-Pol Beam mode 16, relative power

The average signal power for double-bounce scattering increased from -27.69 dB in October 2011 to -21.62 dB by March 2012, an increase in signal strength from this backscattering mechanism, but taken into context is not proportional to that of other backscatter types. Following this increase in average signal power, the relative power for double-bounce scattering rose, from 0.0017 to 0.0069. Regardless of the increase in signal strength and power, the proportion emanating from double-bounce scattering showed a general decline, from 14.12% to 6.23% by March 2012.

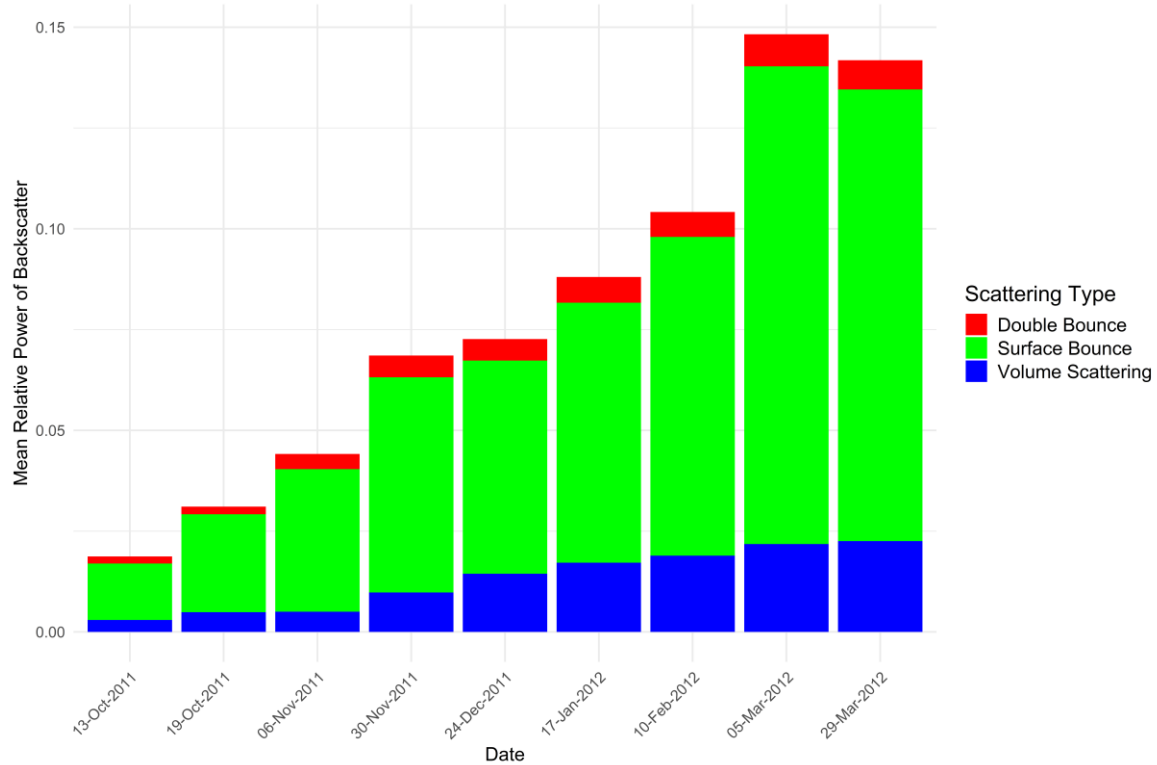


Figure 14 Old Crow, RADARSAT 2 Standard Quad-Pol Beam mode 16, proportion of signal

The average signal power for volume scattering exhibited a general increase from -26.04 dB in October 2011 to -17.94 dB by March 2012, signaling an increase in signal strength for volume scattering mechanisms, possibly indicative of changes in properties or density of volume scatterers. The relative power of volume scattering also saw an uptick, from 0.0025 to 0.016. The total signal proportion attributable to volume scattering demonstrated variability, yet generally exhibited an upward pattern, increasing from 20.65% to 14.55%.

Co-Polarization Phase Difference Ratio

The co-polarized phase difference values observed in Figure 14 for fine beam mode 19 at the Old Crow site generally demonstrate stability over the observation period. This stability is indicated by the consistent mean phase difference, which remain steady, save one instance in April 29th. This

consistence suggests minimal variations in the target's scattering properties. Anomalies are most

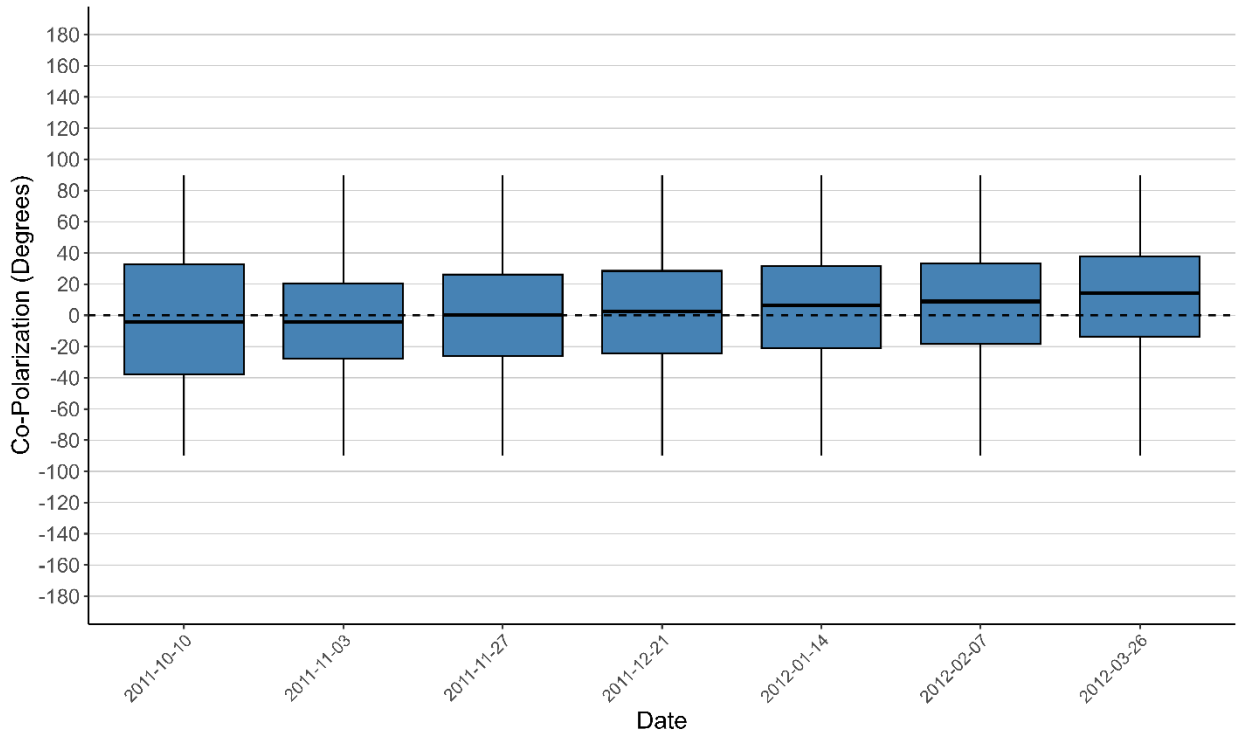


Figure 15: C-band co-polarization ratio for fine beam quad mode 19 from 2011-2012 at Old Crow (RADARSAT 2).

notable in the dataset with a singular pronounced deviation occurring on April 29th, where the co-polarization values peaked at 20.5 degrees. This deviation is significant given the tight clustering of mean values around zero. The absence of data from January to April introduces a caveat to the continuity and interpretability of the temporal pattern. Notwithstanding this gap, the data, where available, exhibits minimal variability in co-polarization values, with narrow interquartile ranges (IQR), and maintains a distribution that mirrors the behaviour observed at the Noel Lake site.

Old Crow Site Summary

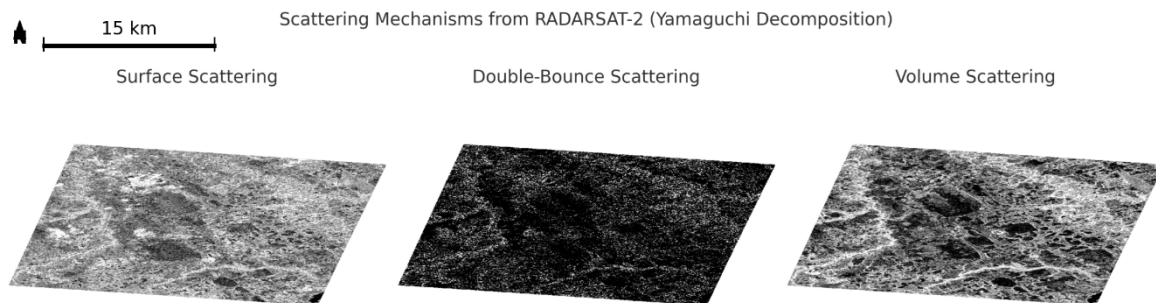


Figure 16: Old Crow scattering mechanisms in grey scale. SQ24, RADARSAT-2, 2011.

The temporal decomposition analysis of Old Crow Lake, using standard beam modes 24 and 16 from October 2011 to March 2012, exhibits distinctive patterns in the behavior of single-bounce, double-bounce, and volume scattering mechanisms. A sharp escalation in the average signal power for single-bounce scattering is observed, with a substantial increase from -25.68 dB to -12.16 dB in beam mode 24 and from -21.04 dB to -10.58 dB in beam mode 16 by March 2012. In contrast, double-bounce scattering presented a less pronounced increase in average signal power. The pattern was similar across both beam modes 24 and 16, with the relative signal power slightly increasing and proportion of double-bounce scattering decreasing, exhibiting reduced influence within the microwave signal composition over the winter season. Volume scattering displayed a general increase in signal strength in both beam modes, with a notable rise in relative power, though its proportion to the overall signal is reduced during the winter season.

5.2 Noel Lake

A time series of Radarsat-2 full polarimetric datasets of Noel Lake span October 2018 to May 2019 with data acquired using fine beam mode 2 and 19 (with average incidence angles of 19 and 40, respectively). Single-bounce, double-bounce, and volume scattering mechanism contributions are examined in the same format as Section 5.1.

Fine Beam Quad Mode 2

A notable trend of escalating signal strength for single-bounce scattering emerges from the data, starting at -14.87 dB in October 2018 and achieving its peak of -5.28 dB by May 2019. The average relative power of single-bounce scattering also shows an increase in backscatter throughout the observation period, evolving from 0.033 to 0.29. Such an increase underscores the persistent dominance of single-bounce scattering with freshwater ice for the deep Noel Lake, consistent with shallow lakes observed in Old Crow. Concurrently, the proportion of the microwave signal attributed to single-bounce scattering exhibits a consistent increase, from 83.99% to 91.51%, comprising nearly all of the signal observed at the sensor.

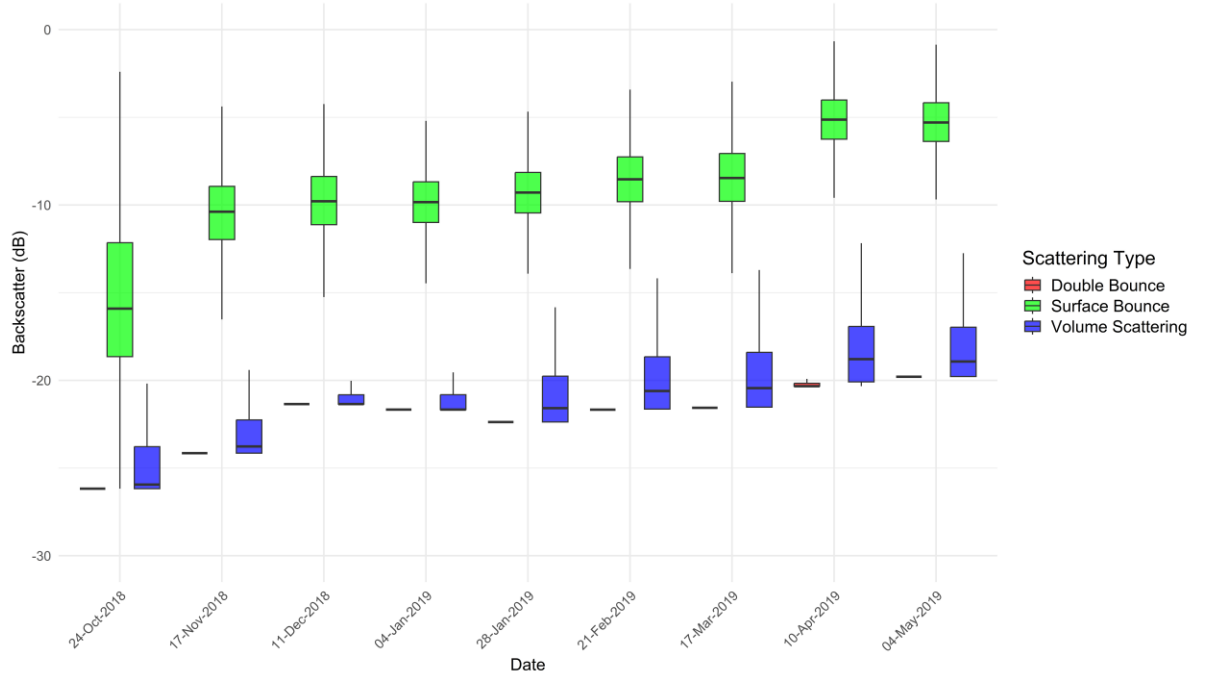


Figure 17: Noel Lake, RADARSAT 2 Fine Quad-Pol Beam mode 2, mean backscatter power (dB)

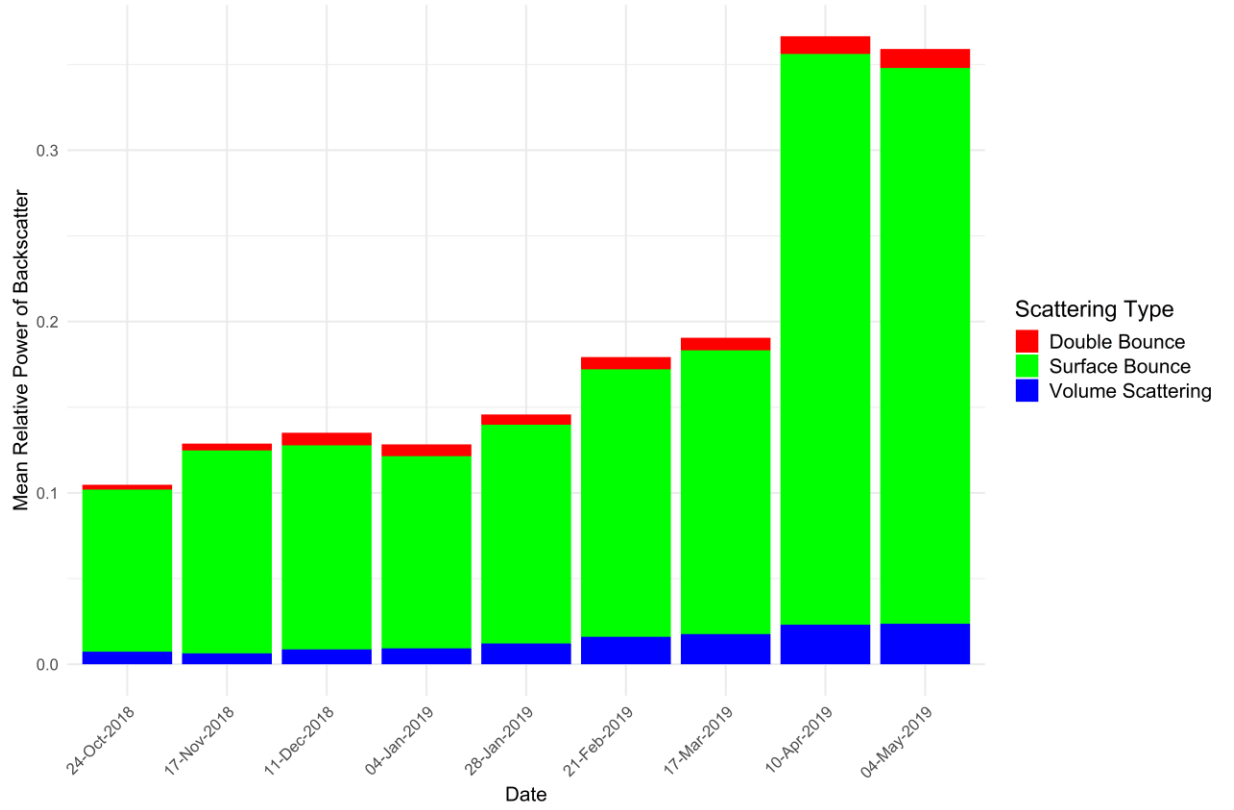


Figure 18: Noel Lake, RADARSAT 2 Fine Quad-Pol Beam mode 2, relative power

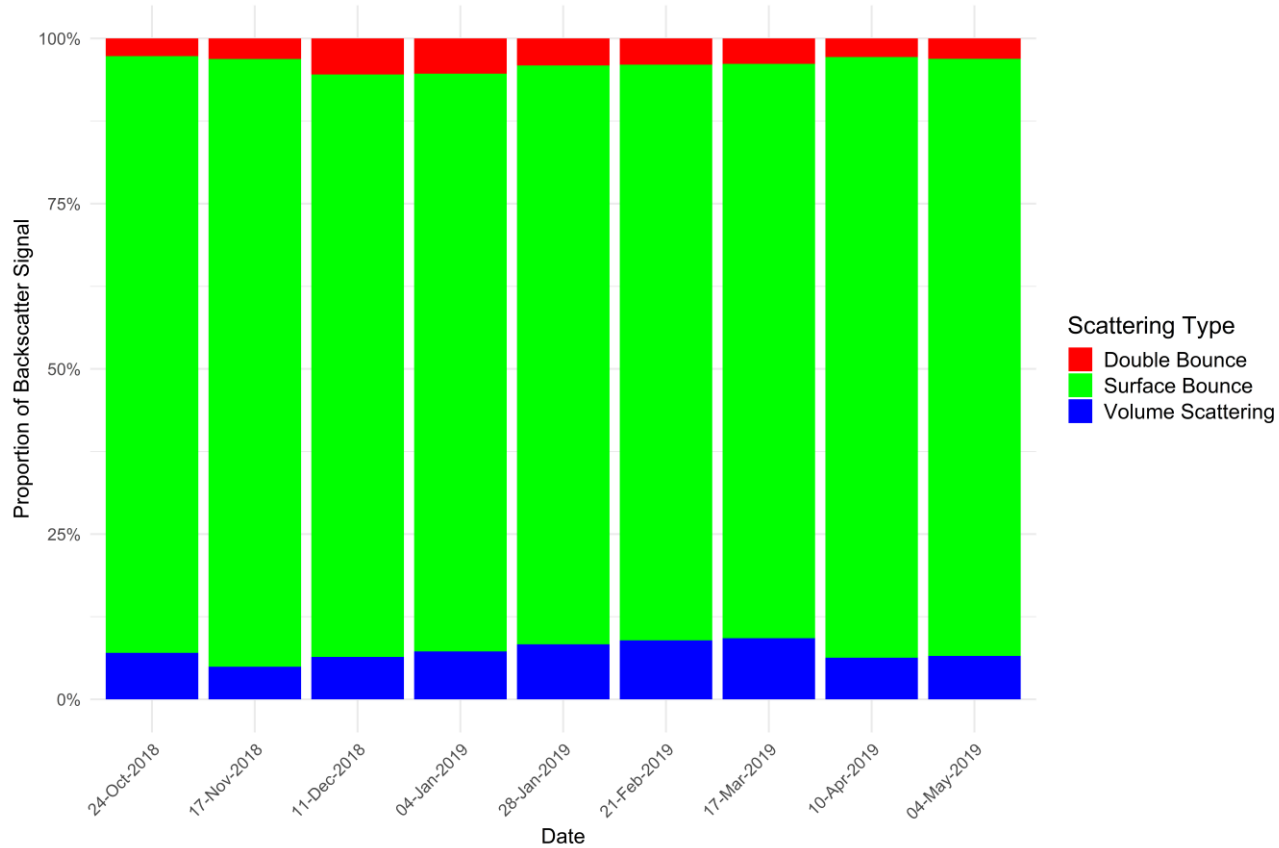


Figure 19: Noel Lake, RADARSAT 2 Fine Quad-Pol Beam mode 2, proportion of signal

Double-bounce scattering reveals a general increase in average signal power, from -25.93 dB in October 2018 to -19.63 dB by May 2019. This trend denotes a slight increase in signal strength from double-bounce backscattering mechanisms. Additionally, the average relative power for double-bounce scattering slightly fluctuates but ultimately exhibits an increase, moving from 0.0026 to 0.011. The proportion of double bounce in the overall signal decreases from 6.57% to 3.36% throughout the winter of 2018-19, reflective of decreased microwave signal interactions with vertical structures.

The dataset also indicates a general increase in average signal power for volume scattering, from -24.36 dB in October 2018 to -17.80 dB by May 2019, with average relative power for volume scattering increasing from 0.0037 to 0.017. However, the total microwave signal proportion

attributable to volume scattering exhibits a slight overall decrease, from 9.44% to 5.13%, indicating that while the absolute signal strength from volume scattering varies through the year, its relative importance diminished in comparison to single-bounce scattering, likely due to the more pronounced increase in single-bounce scattering throughout this period.

Fine Beam Quad Mode 19

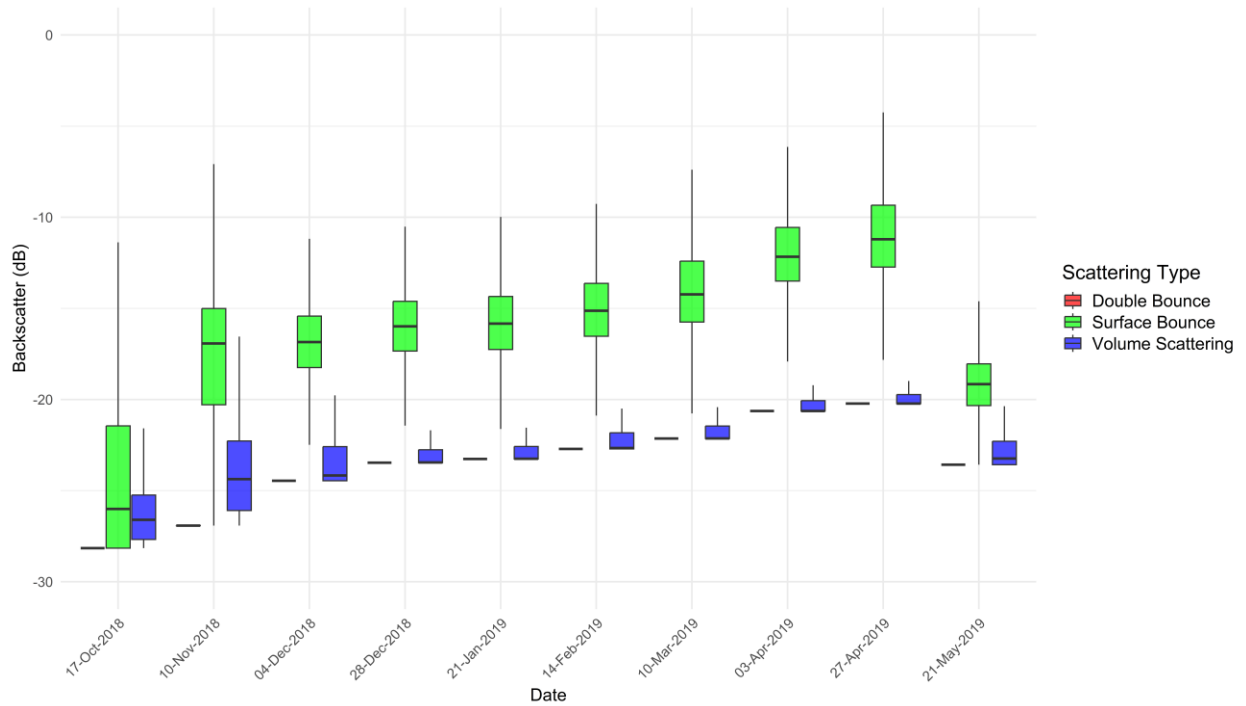


Figure 20: Noel Lake, RADARSAT 2 Fine Quad-Pol Beam mode 19, mean backscatter power (dB)

Compared to the steeper FQ2 mode, FQ19 with a shallower range of incidence angles also exhibits a general increase in the average signal power for single-bounce scattering, from -23.99 dB in October 2018 to -19.22 dB by May 2019. As well, the average relative power for single bounce scattering exhibit an increase, from 0.0039 to 0.081, before declining to 0.012 towards the study's conclusion. The proportion of the total signal attributable to single-bounce scattering shows

variability, starting at 48.02% and peaking at 79.43%, highlighting shifts in the dominance of single-bounce scattering. Curiously, for the final capture, in May 2019, we can see a sudden decrease in the proportion of single-bounce to 55.41%, which could be reflective of a drastic change in the surface composition, most likely caused by the onset of melt and increase in absorption of the signal.

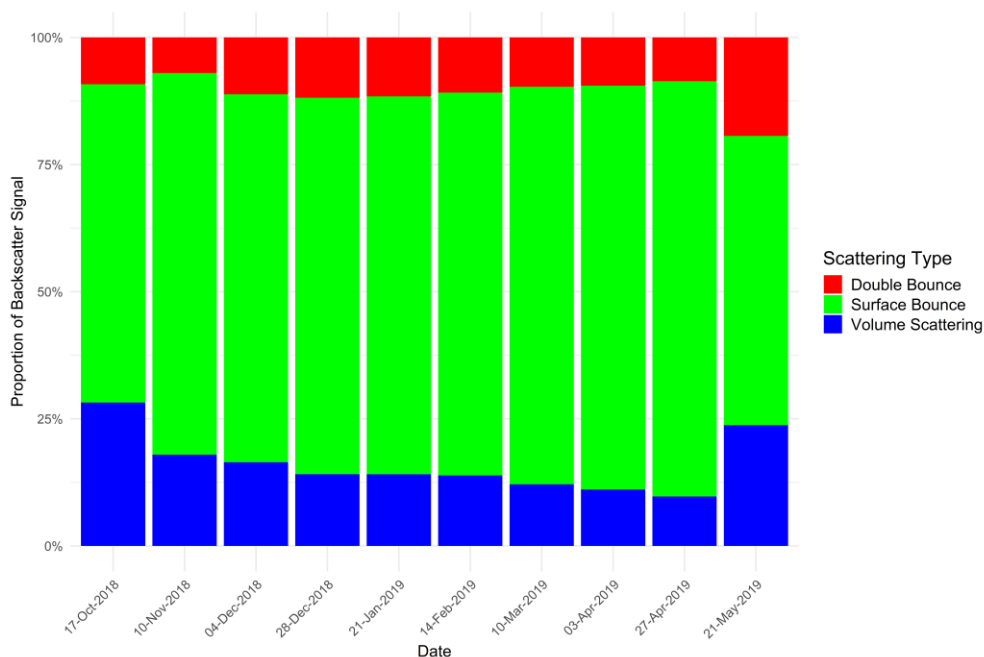


Figure 21: Noel Lake, RADARSAT 2 Fine Quad-Pol Beam mode 19, proportion of signal

The average signal power for double-bounce scattering also displays an increasing trend, from -27.90 dB in October 2018 to -23.58 dB by May 2019. As well, the average relative power for double-bounce scattering exhibits variability, initially increasing from 0.0016 to 0.0099, but then decreasing to 0.0044 reflecting a similar fluctuation found in the single bounce. The signal proportion

from double-bounce scattering initially decreases from 32.45% to 9.85%, then markedly increases to 20.33% by the timeseries end.

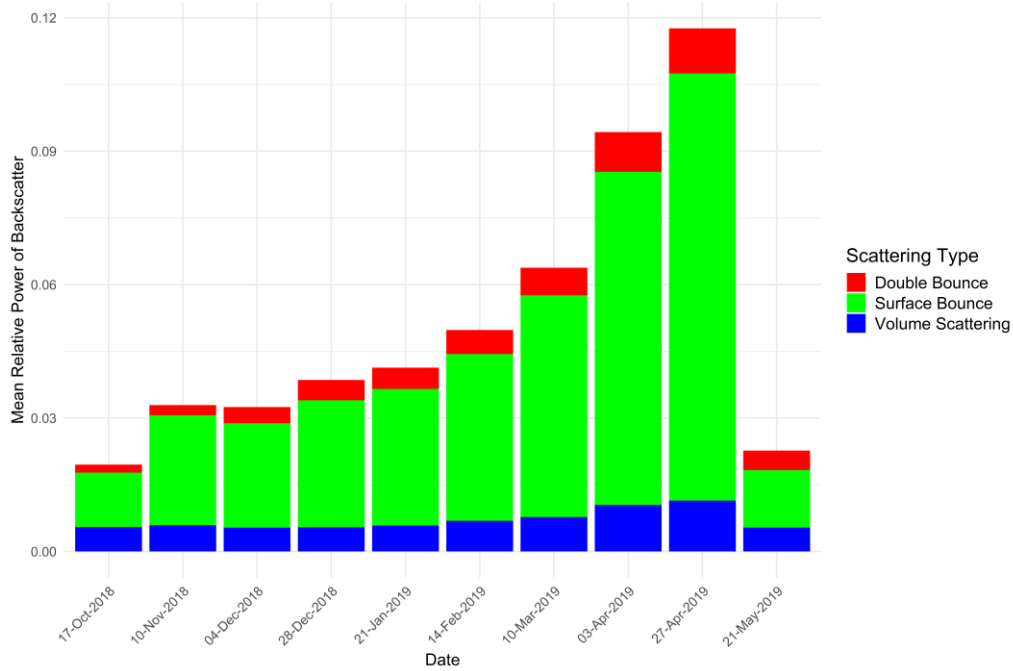


Figure 22: Noel Lake, RADARSAT 2 Fine Quad-Pol Beam mode, relative signal power

For volume scattering, the average signal power shows a decrease from -25.69 dB in October 2018 to -22.81 dB by May 2019, indicating a subtle increase in signal strength, suggestive of changes in scatterers' properties within the volume, such as vegetation density or moisture content. The total microwave signal proportion attributed to volume scattering demonstrates variability, initially increasing and then settling at 24.27% by May 2019, contrasting the decrease in proportional volume scattering observed in the steeper FQ 19.

Co-Polarization Phase Difference Ratio

In contrast to Old Crow, the Noel Lake site's co-polarization phase difference values illustrate a discernible seasonal trend with a gradual increase, especially notable during the late winter months.

This is underscored by the progressively rising mean value, culminating in a peak of 17.1 degrees on April 27th. The IQRs in these spring months are wider, reflecting a greater variability in the data. Outliers are present in the dataset, notably during periods of increased variability, in the later acquisitions. Furthermore, there is some positive skewness present in the data during these late winter periods, as indicated by the averages that are not centrally located within the boxes, suggesting an asymmetry in distribution of co-polarization values.

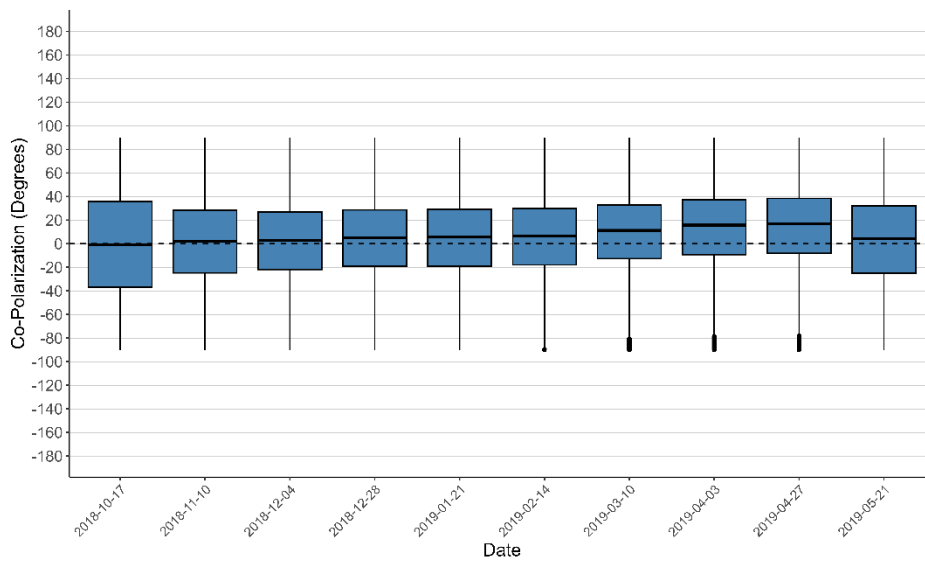


Figure 23: Noel Lake, RADARSAT 2, co-polarization returns

Noel Lake Site Summary

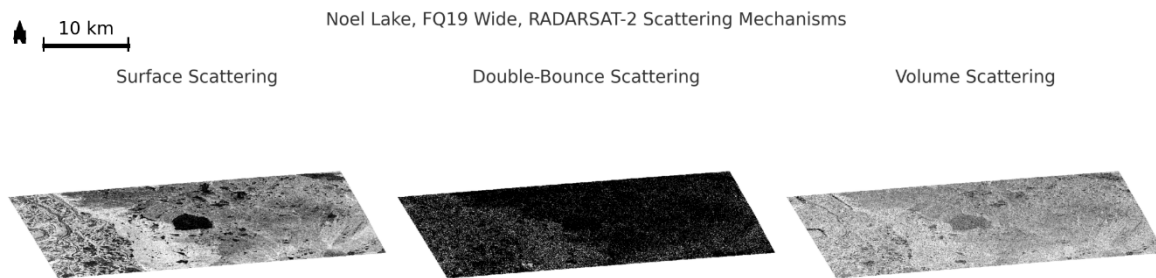


Figure 24: Noel Lake scattering mechanisms in grey scale. FQ19W, RADARSAT-2, 2018

Our polarimetric analysis of Noel Lake, utilizing fine beam modes 2 and 19 from October 2018 to May 2019, has revealed patterns across single-bounce, double-bounce, and volume scattering mechanisms. The average signal power for single-bounce scattering demonstrated a notable increase in both beam modes, with notable power increases from -14.87 dB to -5.28 dB in beam mode 2 and from -23.99 dB to -19.22 dB in mode 19. The analysis also presented an increase in average signal power for double-bounce scattering in both beam modes, although the relative importance within the microwave signal composition decreased over time, showing a smaller proportion of signal double bounce against the increasingly dominant single-bounce scattering. The signal proportions for double-bounce scattering began at 6.57% and 32.45% for beam modes 2 and 19, respectively, and showed a declining trend, reinforcing the observed decrease in its relative influence. Volume scattering in Noel Lake exhibited an overall increase in average signal power, but the proportion of the microwave signal attributed to volume scattering demonstrated a decrease. The behaviour of volume scattering shows an increase in absolute terms but a relative decline when compared to single-bounce scattering. The cumulative results from Noel Lake's polarimetric analysis underscore the dominance of single-

bounce scattering and a diminishing relevance of double-bounce and volume scattering throughout the observed period.

Polarimetric Decomposition Results Summary

Although Old Crow and Noel Lake are notably different in depth from each other, Old Crow being shallow (5.7 m) and Noel Lake being deep (17m), the decomposition and co-polarization results reveal similar backscattering characteristics across both sites. Single-bounce consistently and without fail emerged as the dominant backscattering mechanism, increasing in both absolute power and signal proportion. Double-bounce scattering, while present, remained negligible for each beam mode and capture area.

Volume scattering demonstrated more variability across the time series, particularly at Old Crow, but remained a minor component when compared to the overall contribution of single-bounce scattering. After taking this deep dive into to backscattering profiles of two lakes, shallow and deep, the patterns suggest that differing bathymetric profiles or average lake depths exhibit broadly comparable microwave backscattering responses.

5.3 Multiple Lakes and Wavelengths

The following section presents results from polarimetric decomposition for shallow and deep lakes for additional spaceborne platforms at shorter (X-band, 9.6 GHz, 3.1 cm) and longer (L-band, 1,275 GHz, 23.5) wavelengths to explore the scattering mechanisms to investigate the signal's dependence on frequency and lake depth. Overall, the behavior of the microwave signals show that shorter wavelengths return higher power values than much larger wavelengths, consistent with how a common surface roughness value scatters varying wavelengths. Additionally, regarding wavelength size, we can see that the depth of the lakes have a minimal effect on the back scattering returns, with

shallower lakes showing a slightly higher power return than the deeper lakes. Finally, regardless of wavelengths it is apparent that single-bounce backscattering returns are the dominant backscattering mechanism for lake ice which is displayed in Figure 22 and Figure 23.

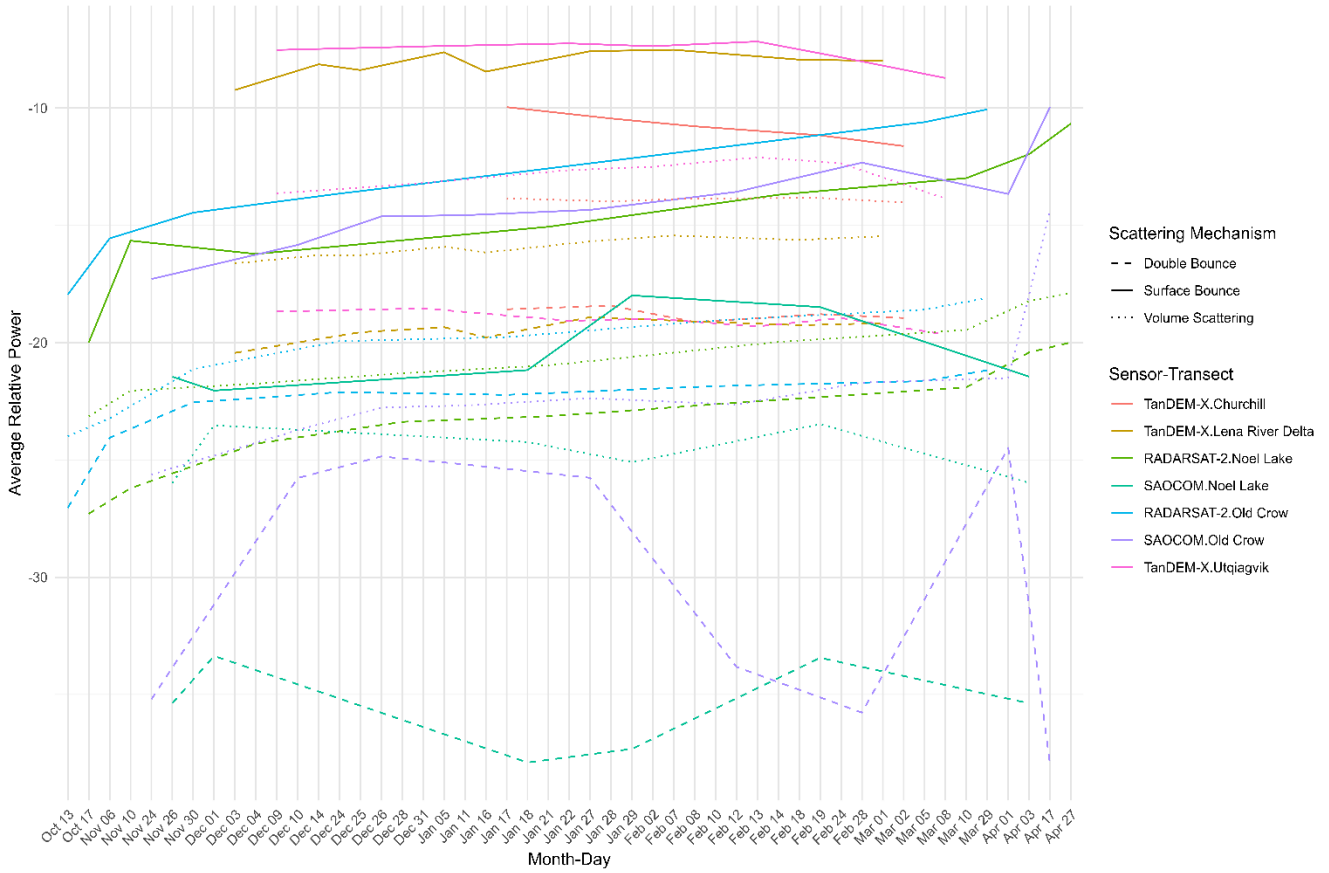


Figure 24: All Sites and beam modes, RADARSAT 2, SAOCOM, and TanDEM-X, mean backscatter signal power (dB). Showing all wavelengths and scattering types.

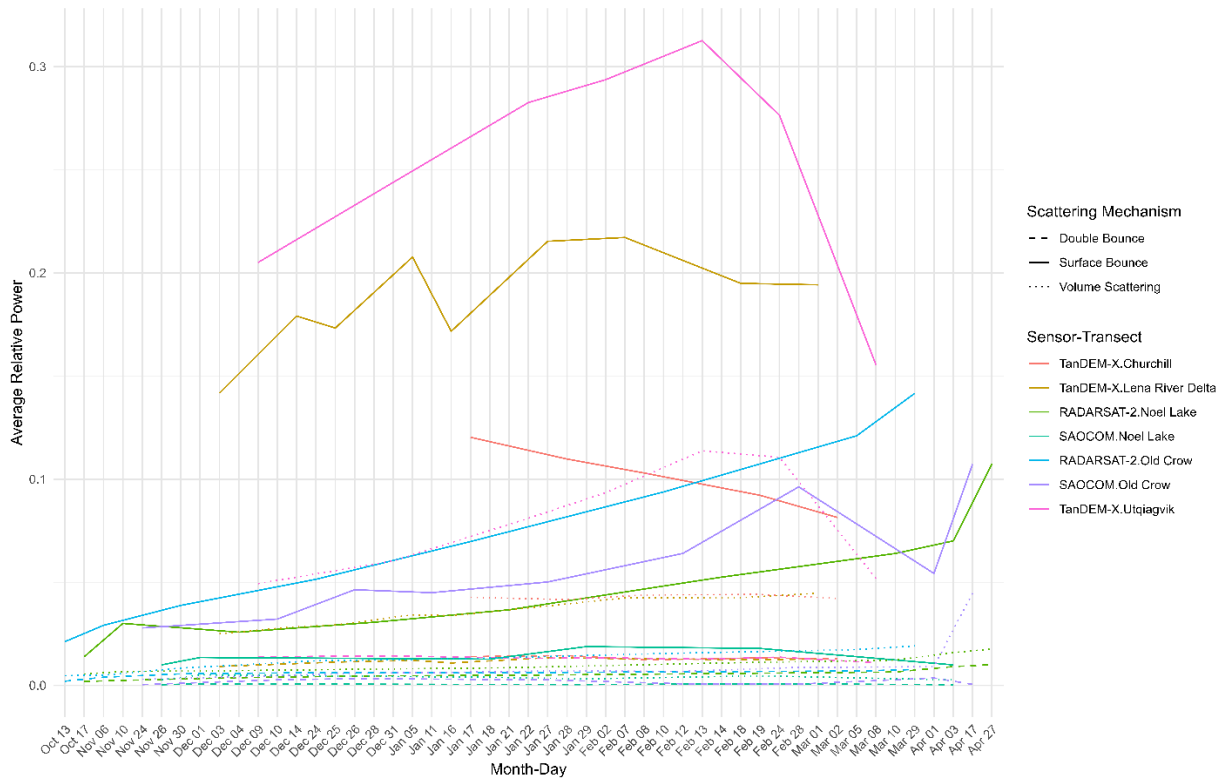


Figure 25: All sites and beam modes, RADARSAT 2, SAOCOM, and TanDEM-X, average relative signal intensity visualized in linear power. Showing all wavelengths and scattering types.

5.3.1 TanDEM-X

At X-Band (9.65GHz, wavelength of 3.1 cm), decomposed backscatter returns are analyzed for 193 lakes of varying depths across Churchill, MB, Utqiagvik, AK, and the Lena Delta. Lake depths ranged from less than 0.5 m to over 17 m.

5.3.1.1 Utqiagvik Site (Alaska North Slope)

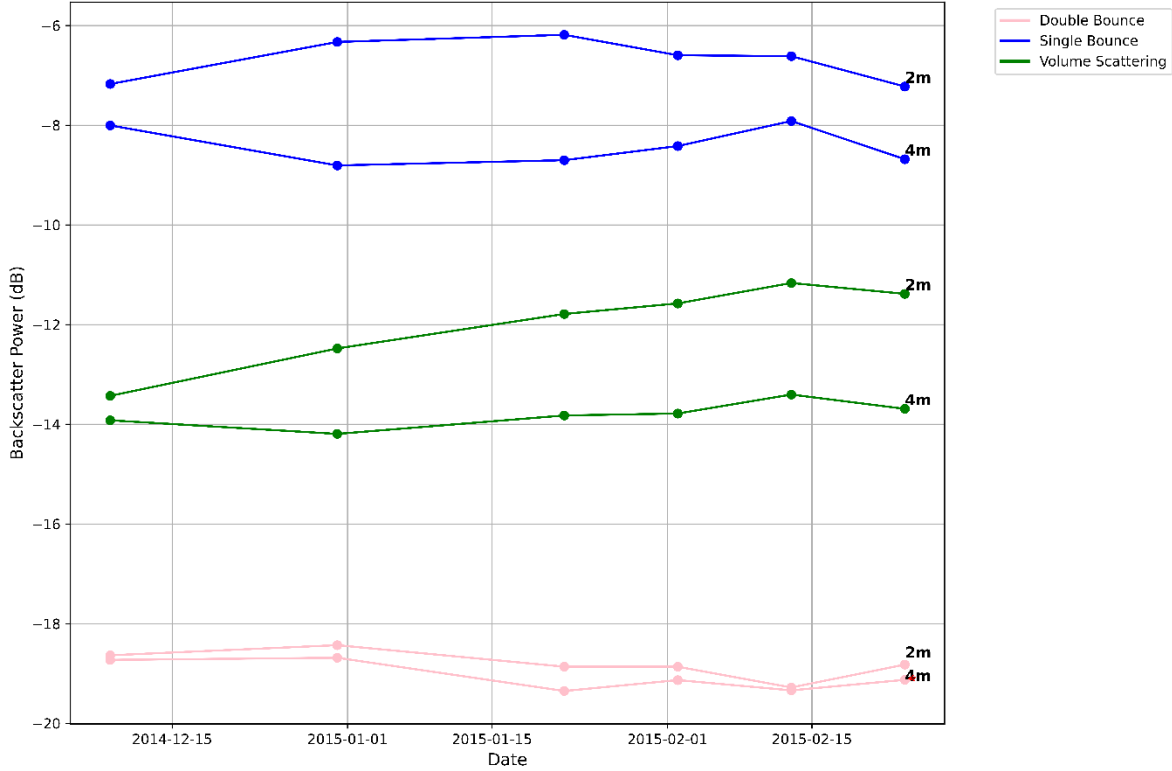


Figure 26: Mean backscatter power broken out by lake depths. 2m depth binning interval. TanDEM-X, 2015. Strip-map Far 8. Incidence angles 30-50°.

For lakes surrounding Utqiagvik, AK., single-bounce scattering dominated the signal during the winter of 2015, accounting for over 60% of the total signal composition. Figure 26 illustrates the temporal trends in mean power for the various scattering mechanisms at this site. The mean power for single-bounce scattering increased from -8.4 dB in early December 2014 to -6.1 dB by late January 2015

Volume scattering became more prominent as winter developed, with mean power increasing from -14 dB in early December to -11 dB by February. In contrast, double-bounce scattering remained

minimal, with mean power values consistently around -18 to -19 dB, indicating limited ice-water interface interactions.

The signal proportion data, illustrated in Figure 27, further corroborates these findings, demonstrating the dominance of single-bounce scattering and the gradual rise in volume scattering as the winter progressed. Additionally, when considering this data by its depth class, it is apparent that the proportion of single-bounce backscatter for shallower lakes (0-2 metres) decreases throughout the season as ice thickens and becomes bedfast as shallower lakes freeze to bed (Figure 25). Overall, shallower lakes exhibit stronger absolute backscatter than the deeper lakes throughout the study period (Figure 24).

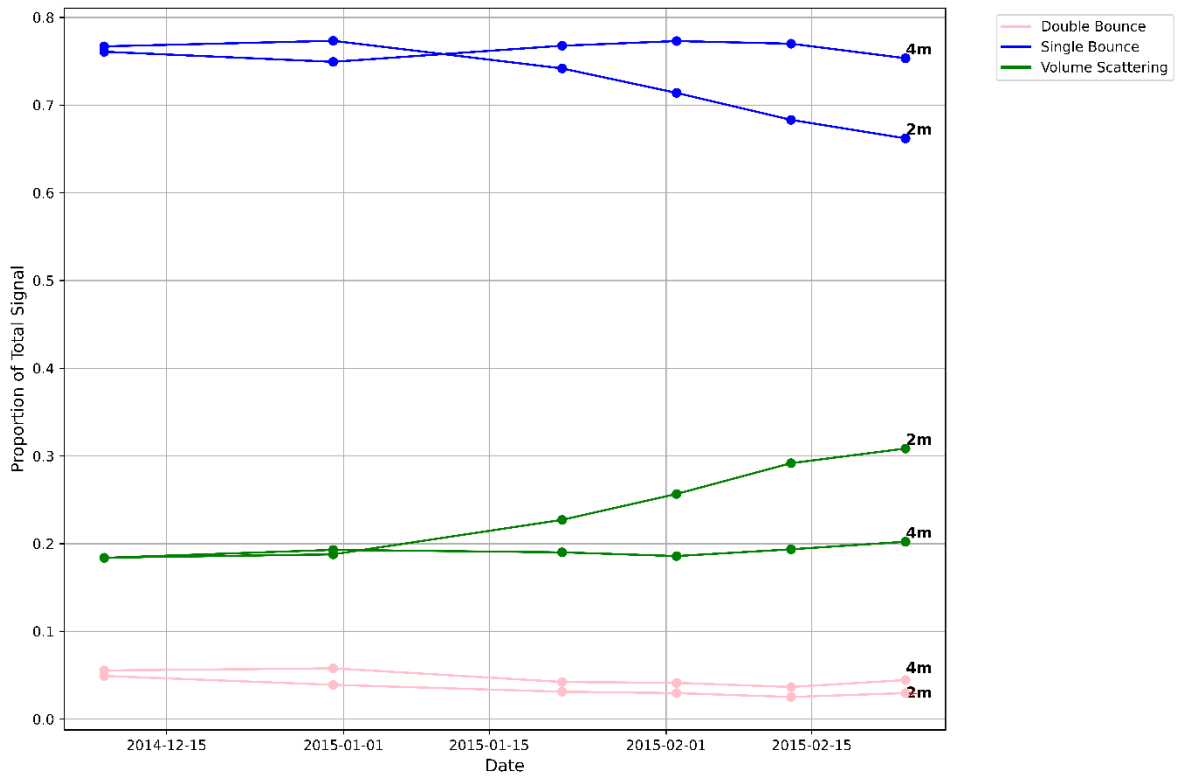


Figure 27: Mean signal proportion by depth. 2m depth binning interval. TanDEM-X, 2015. Strip-map Far 8. Incidence angles 30-50°.

5.3.1.2 Churchill Site

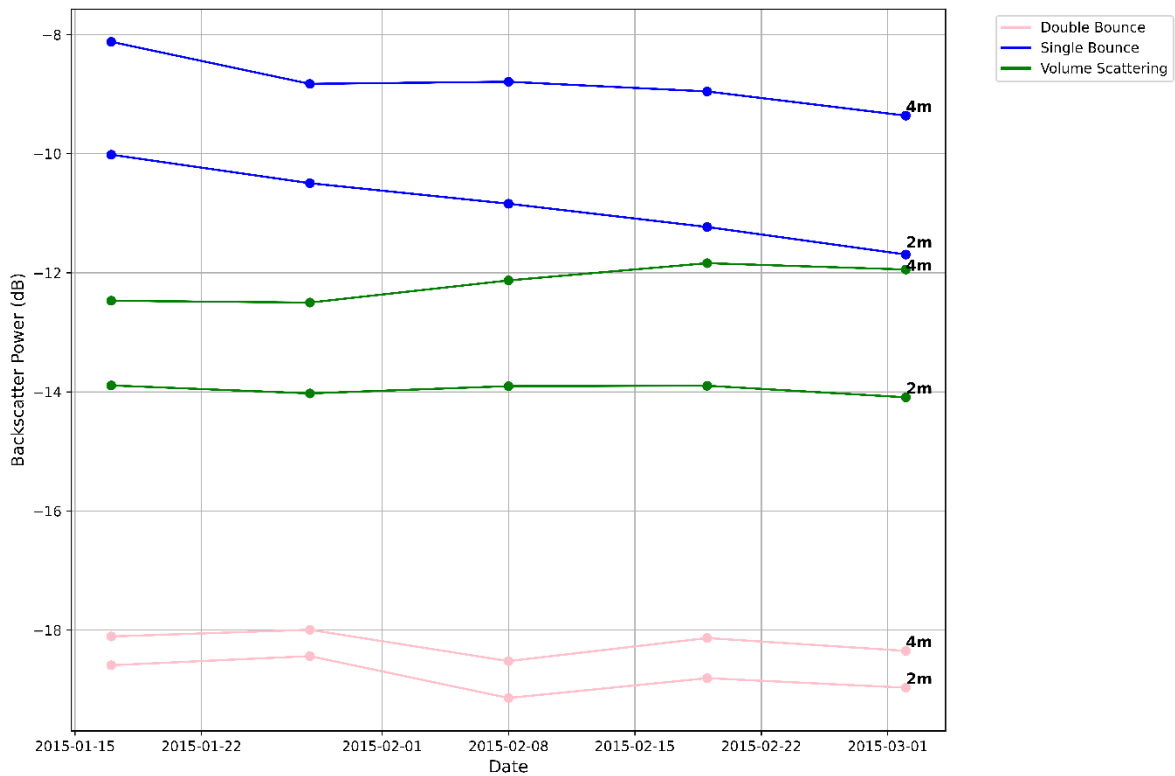


Figure 28: Mean backscatter power broken out by lake depths for Churchill. 2m depth binning interval. TanDEM-X, 2015. Strip-map Far 8. Incidence angles 30-50°.

The Churchill site exhibited a similar dominance of single-bounce scattering, with mean power values remaining steady around -8.5 dB throughout the observation period.

Interestingly, for the shallowest depth classes (0 – 2m), backscatter reduces nearly 4 dB by the end of the study period as a larger proportion of lakes freeze to bed. Figure 26 shows the stability of this scattering mechanism, emphasizing the consistent interaction between microwaves and the rough ice surface.

Volume scattering also followed a progressive trend, with mean power increasing from -12 dB in December to -11 dB by February. This could indicate a development of internal ice heterogeneities, similarly to the observed behaviour at Utqiagvik. Double-bounce scattering was negligible, with mean power hovering around -18 dB, signifying the absence of conditions favorable for double-bounce interactions.

Signal proportion analysis, which can be seen in Figure 27, confirms the prominence of single-bounce scattering at Churchill, maintaining at 60% of the total signal, with volume scattering playing a secondary role as winter progressed. Furthermore, we can see that regardless of depth class, single bounce remained the majority of the signal composition. Though, when we consider the dynamics between each depth class, even though single-bounce remains dominant, deeper lakes exhibit higher absolute signal power returns in Churchill than Utqiagvik as shallow lakes have the propensity to freeze to bed as ice thickens throughout the winter season.

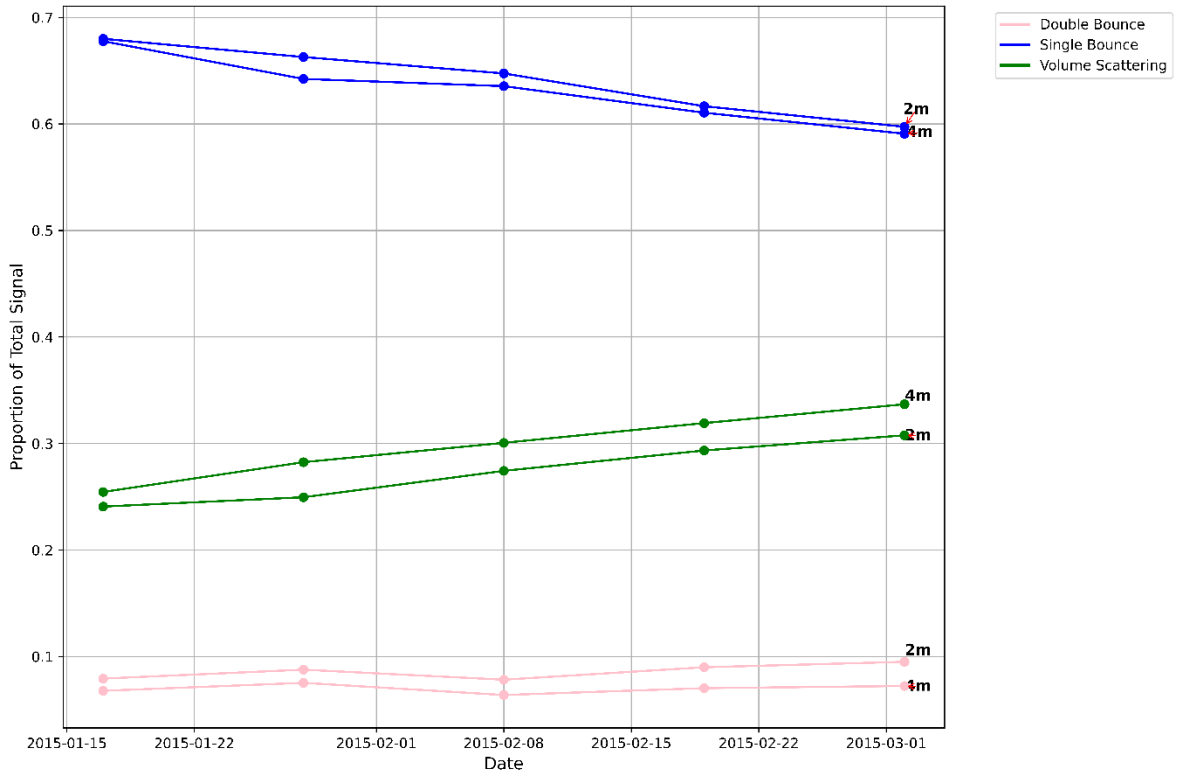


Figure 29: Mean signal proportion broken out by lake depths for Churchill. 2m depth binning interval. TanDEM-X, 2015. Strip-map Far 8. Incidence angles 30-50°.

5.3.1.3 Lena River Delta

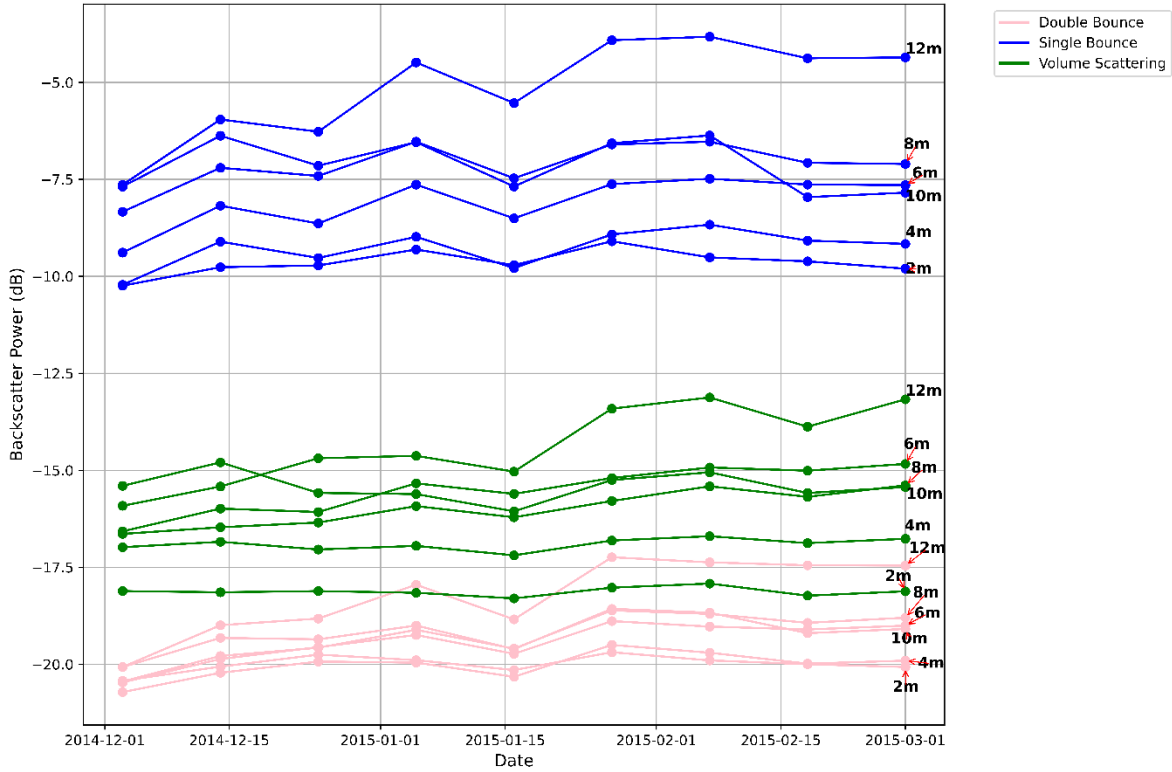


Figure 30: Mean backscatter power broken out by lake depths for Lean River Delta. 2m depth binning interval. TanDEM-X, 2015. Strip-map Far 8. Incidence angles 30-50°.

At the Lena River Delta site, single-bounce scattering again dominated, with mean power values increasing from -7.9 dB in December to -6.9 dB by February. Figure 28 highlights this consistent trend for the Lena River Delta. Single bounce also dominated the proportion of the received signal. Considering the depth classes, shallower lakes had lower absolute signal power than shallower lakes. In terms of signal proportion, the relevance of depth becomes more muddled, with a seemingly random ordering of rank.

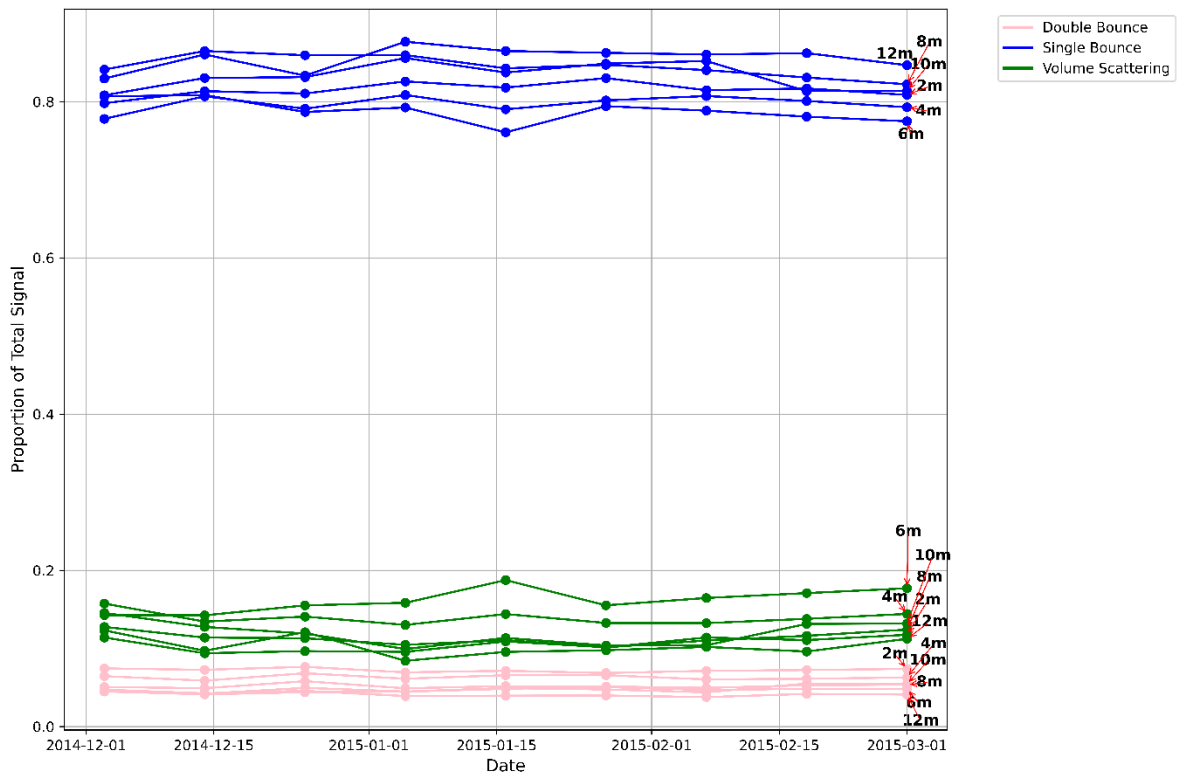


Figure 31: Mean signal proportion broken out by lake depth, Lena River Delta. 2m depth binning interval. TanDEM-X, 2015. Strip-map Far. Incidence angles 30-50°.

5.3.1.4 Summary

Single bounce scattering is the dominant backscatter mechanism at the X-band wavelength for the lake ice captured in this study, these results are represented in Figures 26 to 31. Volume scattering gains importance as winter progresses but remains secondary to single-bounce scattering, while double-bounce scattering plays an insignificant role. These consistent patterns across the three study sites and lake depths, for the X-band wavelength and reflects similarities in form to the other platforms covered by this study.

5.3.2 SAOCOM

For this section, we analyze SAOCOM data (1.275 GHz, wavelength = 23.5 cm) to understand the scattering mechanisms of lake ice. Only a total of 17 lakes were examined in this series, as the resolution and geocorrection of SAOCOM data posed constraints. The results also highlight the dominance of surface scattering across all study sites throughout the winter season.

5.3.2.1 Noel Lake

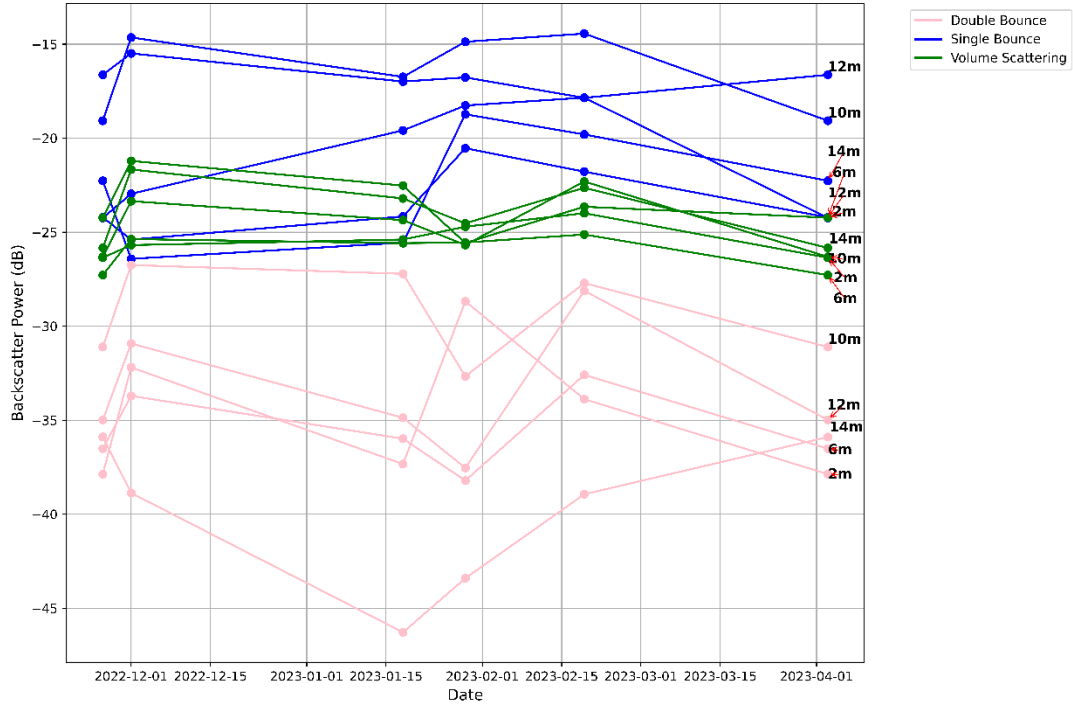


Figure 32: Mean backscatter power by depth class for Noel Lake. 2m depth binning interval SAOCOM, 2021, TOPSAR, incidence angle 20-45°.

At Noel Lake, single-bounce scattering was also the primary contributor to the backscatter signal, accounting for over 60% of the total composition. The mean power for surface scattering started at approximately -20 dB in early November and increased slightly to around -17 dB by late February. The trend, depicted in Figure 32, highlights the consistent dominance of single-bounce scattering across the study period, reflecting the role of surface bounce in the signal composition.

The relative importance of volume scattering at Noel Lake became more apparent as winter progressed. The mean power for volume scattering increased from -25 dB in early November to -23 dB by February, with the signal proportions rising from 30% to 35%. Figure 33 shows this progression, showing some variance in signal proportion, but the majority of the winter single-bounce is the dominant mechanism.

Double-bounce scattering at Noel Lake was negligible, with mean power values hovering around -34 dB in early January and increasing slightly to -33 dB by February. Relative signal proportions remained consistently low, starting at 5% and rising to 6%. These values suggest limited double-bounce backscatter stemming from the ice column, reinforcing the minimal role of this scattering mechanism in L-Band backscatter for lake ice features.

When we consider the effects of lake depth on the signal returns, the 10m, 12m and 14m have a slightly higher absolute power return than that of the more shallow 6m and 2m lakes. This relationship holds true in signal proportion, with the deeper lakes having a higher proportions of single bounce backscatter than that of the shallow lakes.

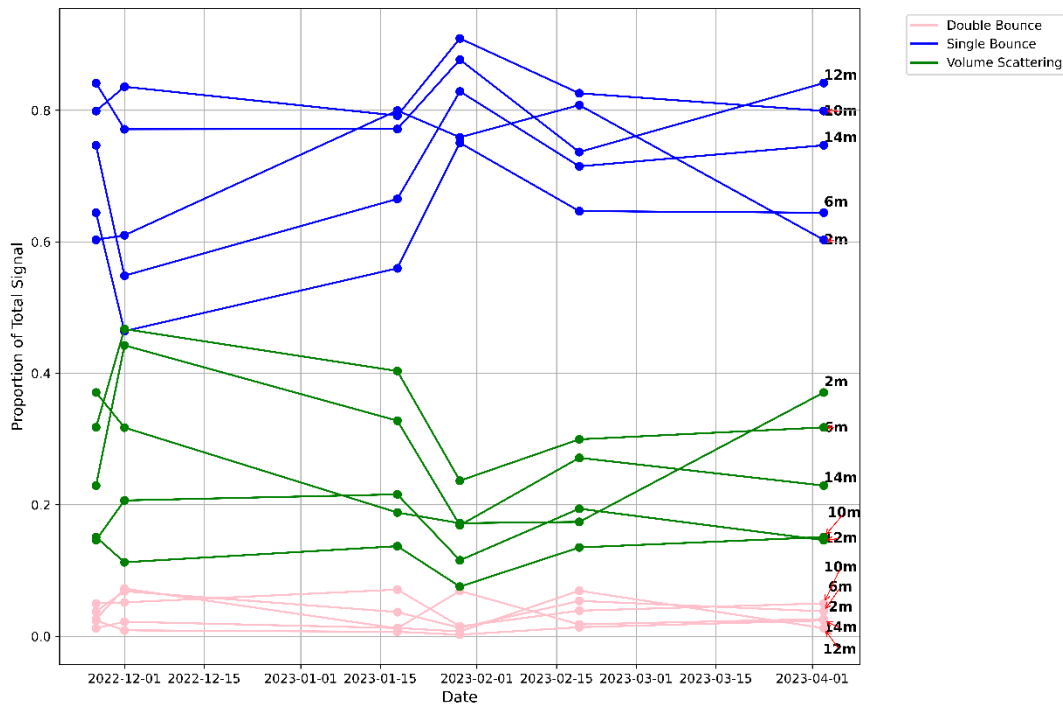


Figure 33: Mean signal proportion by depth class for Noel Lake. 2m depth binning interval SAOCOM, 2021, TOPSAR, incidence angle 20-45°.

5.3.2.2 Old Crow

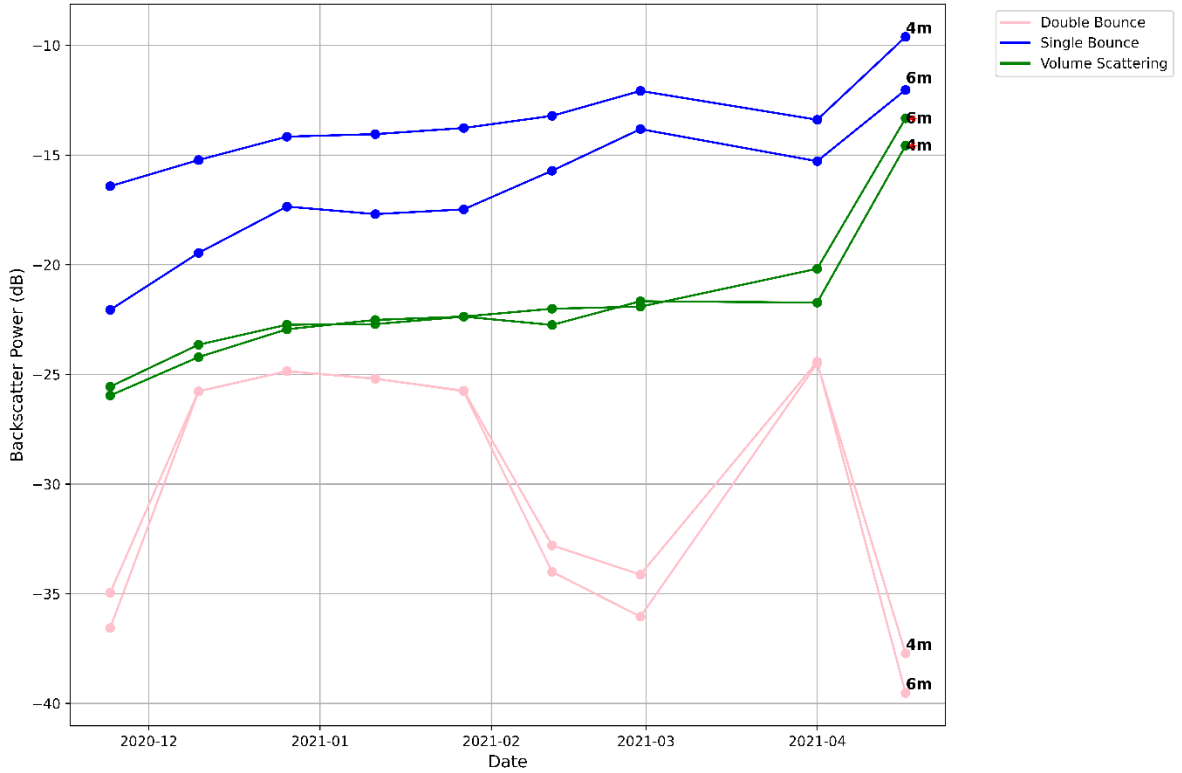


Figure 34: Mean backscatter power by depth class for Old Crow. 2m depth binning interval SAOCOM, 2021, TOPSAR, incidence angle 20-45°.

The Old Crow study site exhibited similar scattering patterns, with single-bounce scattering dominating the backscatter signal and contributing over 60% of the total composition. The mean power for single-bounce scattering increased from -16 dB in mid-November to -11 dB by February, as shown in Figure 32. This increase in backscatter for the shallow lakes at Old Crow is in contrast to the deeper Noel lake region, which exhibited an overall lower (-15 dB at Noel vs. -10 dB at Old Crow) and relatively stable backscatter throughout the winter season (Figure 30 and Figure 32).

Volume scattering followed a similar trend to that observed at Noel Lake, becoming more significant as winter advanced. The mean power for volume scattering rose from -25 dB in December to -21 dB by February. Double-bounce scattering at Old Crow was nearly zero, with mean power values stable around -35 dB (the noise floor of SAOCOM quad-polarization data is -34 dB (Brunelli & Mancini, 2024)). Both of these scattering types reflected similar behaviour to that of Noel Lake, with single-bounce representing the vast majority of the signal composition, followed by volume scattering, and double-bounce essentially at the noise floor of the sensor.

In terms of the depth class, we see a swapping of behaviour in the signal returns, with the shallower of the two classes showing more absolute power than the deeper. This continues into the signal proportion, with the shallow lake single-bounce signal proportions remaining highest.

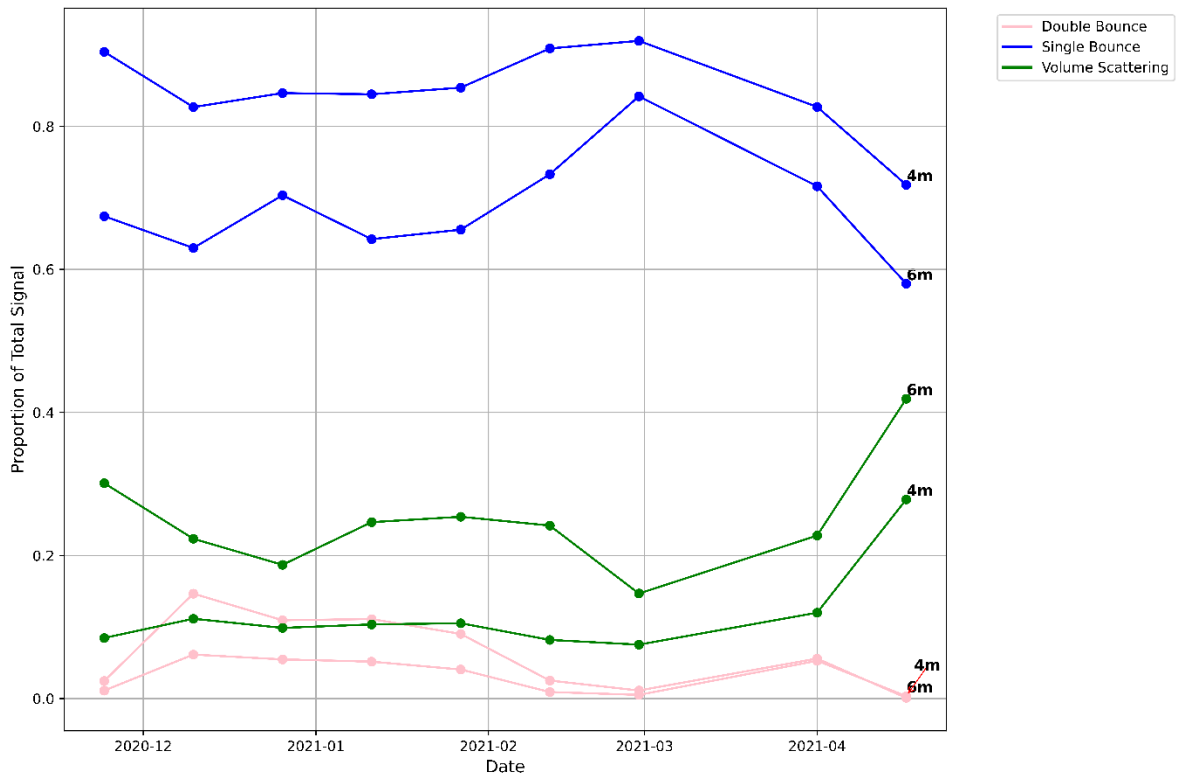


Figure 35: Mean signal proportion by depth class for Old Crow. 2m depth binning interval SAOCOM, 2021, TOPSAR, incidence angle 20-45°.

5.3.2.3 Summary

The continued dominance of single-bounce scattering across both study sites in L-Band backscatter, further highlight this scattering mechanisms its importance to microwave backscatter. The consistent increases in mean power for single-bounce scattering, from -20 dB to -17 dB at Noel Lake and from -16 dB to -11 dB at Old Crow, highlight the influence of surface roughness and evolving ice thickness on microwave lake-ice interactions relative to their depth. At L-band deeper lakes exhibited lower and more stable backscatter than shallow

lakes, which exhibited over all higher backscatter combined with increases in power throughout the ice thickening period.

Volume scattering, while less significant than single-bounce scattering, gained importance as winter progressed. Double-bounce scattering continued to consistently exhibited low mean power values, confirming its negligible role in L-Band backscatter for lake ice.

Single-bounce scattering dominated the L-Band PolSAR backscatter throughout the winter, contributing over 60% of the total signal composition at both Noel Lake and Old Crow. Volume scattering gained importance as winter progressed, though it remained a secondary contributor. Double-bounce scattering had negligible relevance, consistent with findings from other platforms. These behaviours, for the L-band results, are clearly reflected in Figures 32 to 35.

5.3.3 RADARSAT 2

As a radar employing a wavelength of 5.6cm, RADARSAT-2 represents the midpoint between the narrowest and widest wavelength. Due to the availability and quality of imagery, a total of 763 lakes were included in this analysis, well above the number in previous sections. Similar to results from TanDEM-X and SAOCOM, surface scattering was the predominant mechanism observed throughout the winter season for both Noel Lake and Old Crow. This mechanism remained dominant during the early stages of ice formation and persisted throughout the winter, only diminishing during melt onset.

5.3.3.1 Noel Lake

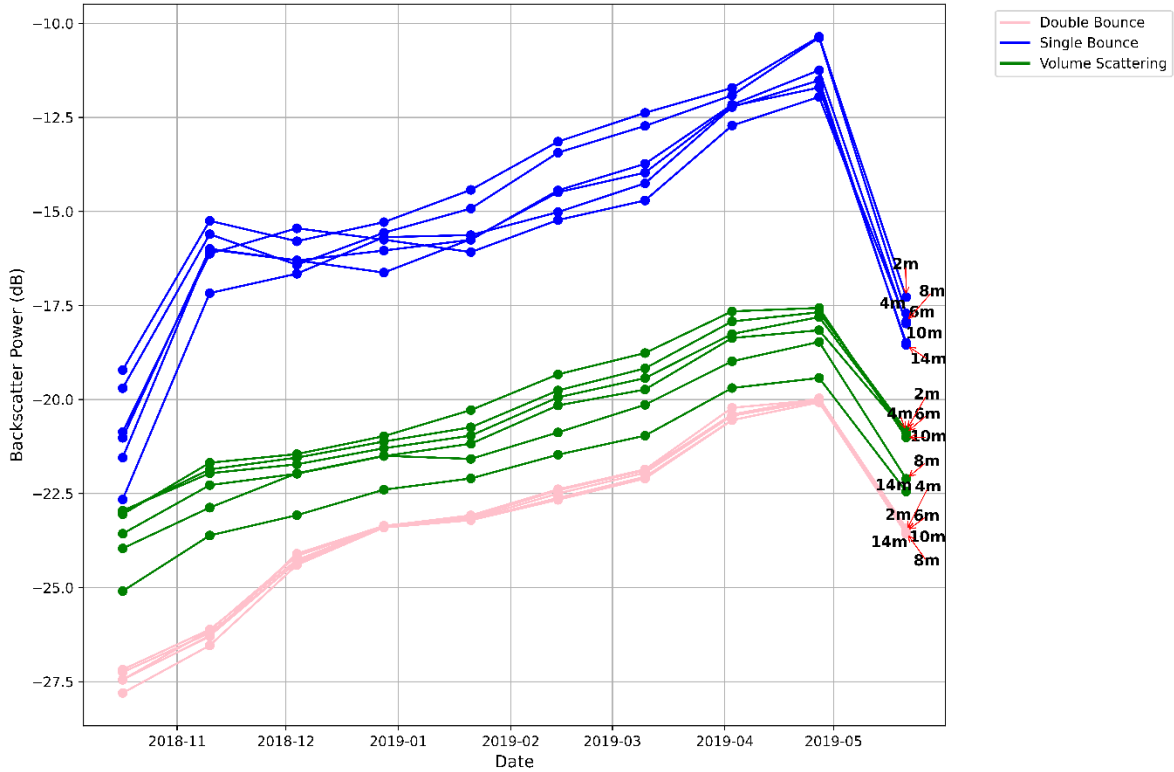


Figure 36: Mean backscatter power by depth class for Noel Lake. 2m depth binning interval RADARSAT 2, 2019, Fine-Quad Pol Beam mode 19. Incidence angle 20-45°.

In the Noel Lake region, surface scattering exhibited consistently high backscatter values. Mean power values for surface scattering started at -19 dB in October and increased steadily to -11 dB by April. As shown in Figure 36, surface scattering was the primary contributor to backscatter throughout the observation period.

Volume scattering at Noel Lake displayed a steady increase in mean power as the winter progressed. The mean power for volume scattering began at -22 dB in October and reached -18 dB by April, as illustrated in Figure 36. Double-bounce scattering, while less dominant,

exhibited a slight increase over the winter. Mean power values for double-bounce scattering started at -27 dB in October and increased to -23 dB by April.

The consistency of the returns for RADARSAT-2, results in a minimal difference between lakes depths, with each lake class behaving in a similar pattern. Lakes in the 8m depth class show the high absolute signal power, but the 10m depth class shows the lowest, but the data is tightly clustered together. This behaviour extends into the signal proportion as well, making it challenging to identify a relationship between depth and signal power.

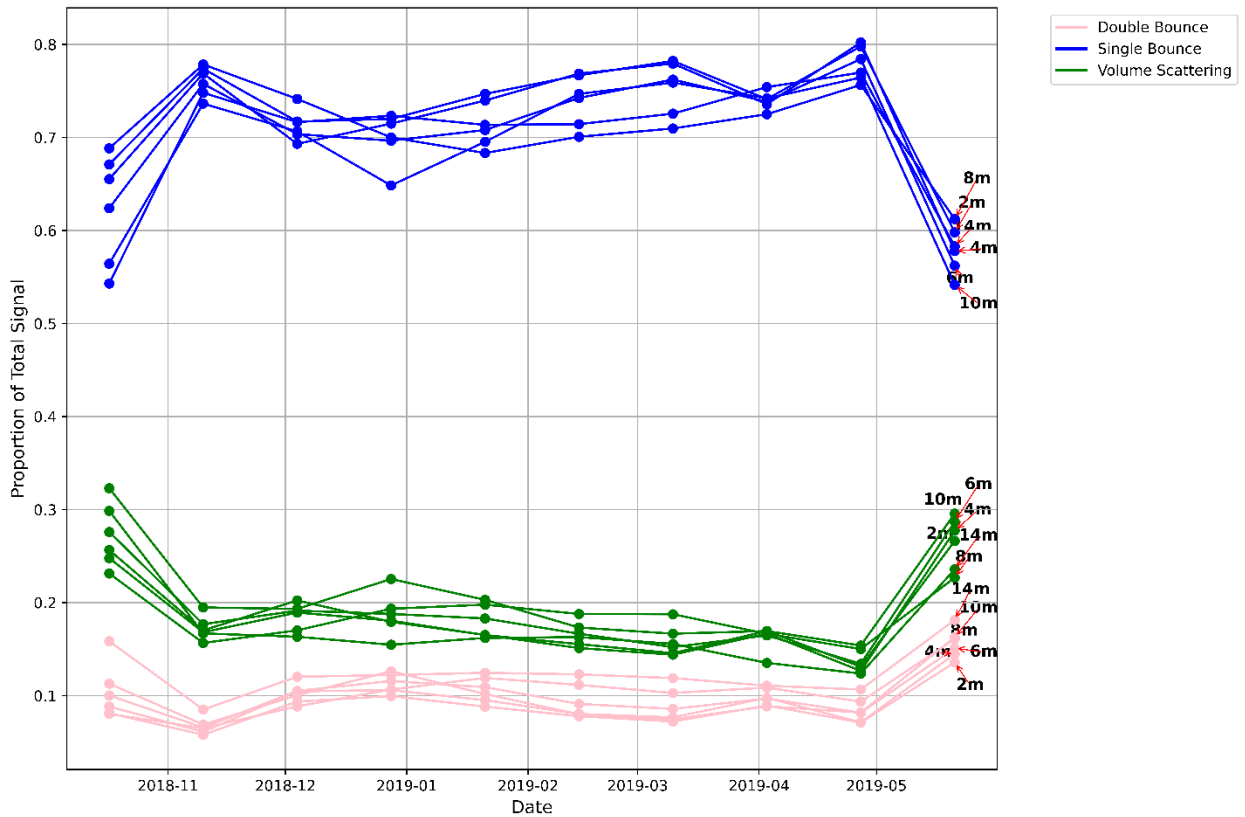


Figure 37: Mean signal proportion by depth class for Noel Lake. 2m depth binning interval RADARSAT 2, 2019, Fine-Quad Pol Beam mode 19. Incidence angle 20-45°.

5.3.3.2 Old Crow

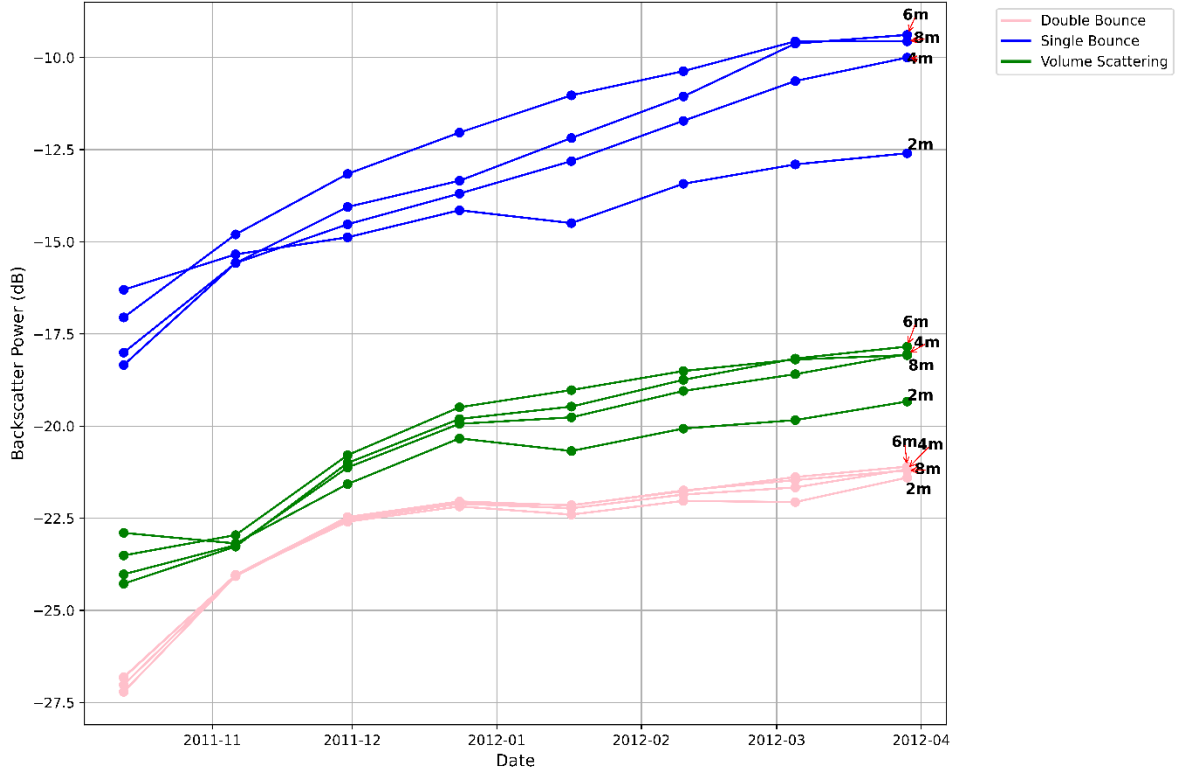


Figure 38: Mean backscatter power by depth class for Old Crow. 2m depth binning interval RADARSAT 2, 2019, Fine-Quad Pol Beam mode 19. Incidence angle 20-45°.

The Old Crow study area exhibited similar trends, with surface scattering dominating the backscatter signal throughout the winter. Mean power values for surface scattering began at -17 dB in October and rose sharply to -9 dB by March, as shown in Figure 36.

Volume scattering at Old Crow followed a similar trajectory to that observed at Noel Lake. The mean power for volume scattering started at -23 dB in October and increased to -17 dB by March. Double-bounce scattering at Old Crow, while minimal, exhibited a slight

increase over time. Mean power values began at -27 dB in October and improved to -21 dB by March.

In regards to depth, the signal power and proportion are again clustered, which creates a challenge to identify a relationship between depth and signal power, but in general, the 4m, 6m, and 8m, are showing stronger returns than that of the 2m lakes (Figure 37).

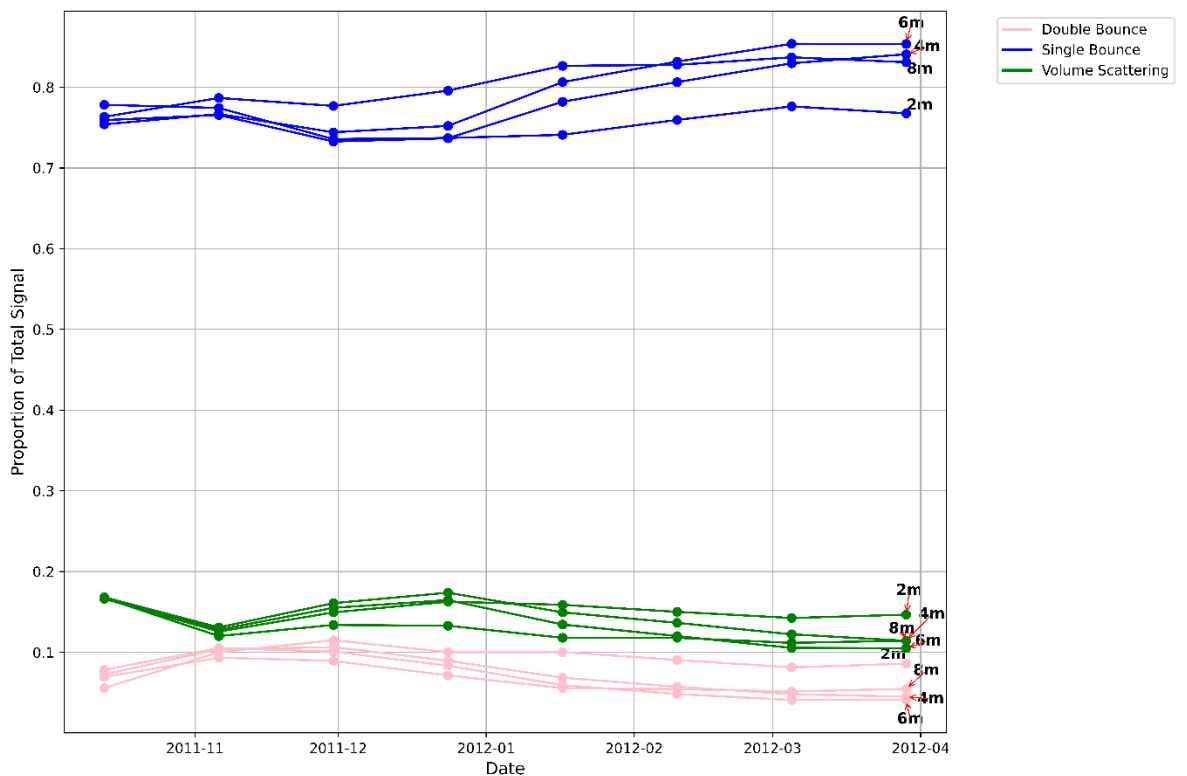


Figure 39: Mean signal proportion by depth class for Old Crow. 2m depth binning interval RADARSAT 2, 2019, Fine-Quad Pol Beam mode 19. Incidence angle 20-45°.

5.3.3.3 Summary

Surface scattering consistently dominated RADARSAT-2 backscatter across both Noel Lake and Old Crow throughout the winter. The increases in mean power values, from -19 dB to -11 dB at Noel Lake and from -17 dB to -9 dB at Old Crow, highlight the critical role of surface roughness and ice conditions in enhancing scattering efficiency. These results are consistent with findings from TanDEM-X and SAOCOM, demonstrating the robustness of surface scattering as a key mechanism in C-Band backscatter signal composition.

Volume scattering became more prominent as winter progressed, with mean power values increasing at both sites, but remained dwarfed by single bounce. Double-bounce scattering remained minimal across both sites, with low mean power and signal proportion values throughout the observation period. RADARSAT-2 data confirmed the dominance of surface scattering in C-Band backscatter for Arctic and Subarctic lake ice, with volume scattering gaining relevance as winter progressed. Double-bounce scattering had negligible influence for deep and shallow lakes at both Noel and Old Crow sites. These results, derived from a larger dataset of 763 lakes, are reflected in Figures 36 to 39.

Chapter 6: Discussion

6.1 Polarimetric Decomposition

The results of the polarimetric decomposition, across wavelengths and lake depths, reveal that the single bounce, according to these results, is the dominant backscattering mechanism at both lake sites. Though each mechanism sees an increase in power as the winter scene progresses, the vast majority of the signal remains firmly classified as single bounce as a result of surface roughness. Following modeling efforts of Murfitt et al, (2022), we can infer that this is due to the signal interacting with the ice-water interface, and the signal power can be attributed to the development of this ice-water interface. This is significant as it clearly show that the main site of interaction between microwaves and lake ice is the ice-water interface, being driven by the contrasting dielectric properties of liquid water and frozen ice. Understanding that the bottom of the ice surface is the interaction point paves the waves for interferometric studies of lake ice, as we can now be more confident that the changes in phase length are occurring between the developing ice layer and the waters surface. For the sake of thoroughness, a deeper exploration of the modelled results will follow.

6.1.1 Single Bounce

Single-bounce scattering across all sites and platforms consistently shows an escalation in average signal power from the beginning to the end of winter. For instance, in the RADARSAT-2 data, the initial values at Old Crow in beam mode 24 began at -25.68 dB in October 2011 and increased progressively each month, reaching -12.16 dB by March 2012. Similarly, in beam mode 16, the signal power rose from -21.04 dB to -10.58 dB over the same period. When the analysis was expanded to incorporate all suitable lakes, a similar pattern of increasing signal power throughout the winters was observed.

Noel Lake, in particular, exhibited the most pronounced upward trend. The signal strength in fine beam mode 2 started at -14.87 dB in October 2018 and peaked at -5.28 dB by May 2019. This substantial increase suggests significant modifications in the backscatter signal, likely influenced by the steeper incidence angle associated with fine beam mode 2. Though less dramatic, fine beam mode 19 also demonstrated a similar behavior, with an increase from -23.99 dB in October 2018 to -19.22 dB by May 2019. This consistent upward trajectory in dB across all captured lakes suggests a progressive enhancement in backscatter behavior from surface roughness at the ice-water interface, reflecting the development of roughness of the interface itself throughout the winter season. This conclusion is supported by contemporary studies of lake ice development and decay, which suggest that influences such as depth, air temperature, and heat flux from lake sediments, all effect the growth length and speed of lake ice, which would promote a rough ice water interface (Rafat et al, 2023).

The proportion of the total microwave signal attributed to single-bounce scattering also increased in a similar manner. At Old Crow, the proportion rose from 53.52% in October 2011 to 79.65% by March 2012 in beam mode 24. This trend was mirrored at Noel Lake, where the proportion increased from 83.99% to 91.51%, the vast majority of the signal composition. Interestingly, the deeper lakes backscattering trends indicate an escalating dominance of single-bounce scattering proportion over time.

In summary, the temporal and site-specific trends in single-bounce scattering at both Old Crow and Noel Lake reveal a clear increase in signal power, relative power, and the proportion of the total microwave signal. Notably, single-bounce scattering consistently remains well above 50% throughout the winter, highlighting its role as the dominant interaction within the total backscatter signal. These findings suggest that, regardless of ice structures, inclusions such as tubular bubbles, or variations in lake depth, single-bounce remains the dominant backscattering mechanism, consistent

with studies observing shallow (Engram et al., 2013; Atwood et al., 2015; Gunn et al., 2018), deep lakes (Shokr & Daboor, 2020).

Atwood, using the YFG three-component polarimetric decomposition model of RADARSAT-2 and ALOS PALSAR imagery of the Alaskan North Slope, for March 2012 showed similar trends as our results (Atwood et al, 2015). This study found that single-bounce scattering accounted for the majority, over 70%, of the backscatter signal composition during the late winter period (Atwood et al, 2015). This proportion is also reflected in our results of imagery from late-winter lake ice backscatter, both in the Alaskan North Slope and across our study, where single-bounce scattering reached as high as 79.85% (Figure 13) of the total signal composition.

Engram, while studying the relationship between microwave backscatter and methane ebullitions trapped in lake ice, found that roughness-driven scattering, also known as single-bounce, dominated the signal composition, rather than volume or double-bounce scattering (Engram et al, 2013). This study employed a Pauli polarimetric decomposition method using dual-pol SAR captures from the Seward Peninsula in Alaska (Engram et al, 2013). While differing in approach, Engram's results for C-band radar showed that single-bounce backscatter returns were stronger than the other two backscattering components in the Pauli decomposition (Engram et al, 2013). This pattern is consistent across the study sites and sensors used in this thesis, where single-bounce dominates the backscatter signal composition for all lakes examined (Figure 24).

Shokr and Daboor, using Cloude-Pottier and YFD three-component polarimetric decomposition methods, found that single-bounce backscattering power increased with lake ice thickness (Shokr & Daboor, 2020). The study's findings, also using RADARSAT-2 captures, for Char and Resolute lakes from the Resolute Bay area, are similar to the results of our study (Shokr & Daboor, 2020). Conducted in 2017, that study combined SAR data with in-situ lake ice thickness measurements to

analyze polarimetric parameters across various ice types and stages of both sea and lake ice (Shokr & Daboor, 2020). A clear similarity emerges between the lake ice-specific results from Resolute Bay and this study: in both cases, single-bounce backscattering power was significantly higher than other backscattering mechanisms (Shokr & Daboor, 2020). Shokr's study observed an increase in average signal power for Char Lake from -16.15 dB to -9.17 dB, while our study of Noel Lake showed a comparable rise from -14.87 dB to -5.82 dB (Shokr & Daboor, 2020).

The behaviour of this study's lake ice microwave backscatter parallels the results and findings of previous works, by showing a consistent and dominant response of single-bounce backscattering. Moreover, the results of this study are consistent across all platforms, including the X-band TanDEM-X and the L-band SAOCOM, smaller wavelengths generally returned higher power values compared to larger wavelengths. Notably, the analysis revealed that single-bounce backscattering remains the most prevalent mechanism for lake ice, regardless of platform or wavelength. For instance, at the Utqiagvik site, surface scattering mean power values increased from approximately -8.4 dB in early December to around -6.1 dB by late January, indicating a robust single-bounce response. This smaller wavelength has the greatest potential for interactions with other ice structures within the ice column and would most certainly show a much more dynamic backscatter response if there was additional structures being interacted with. Similarly, SAOCOM's PolSAR data corroborated this finding, showing that even with a larger wavelength, having a greater potential to skip over ice features, single-bounce continued to be the predominant contributor to the microwave signal, particularly during the early stages of ice formation and continuing through the winter.

The dominance of single-bounce scattering, consistently demonstrated in this study, underscores a reliable and consistent interaction between microwave signals and the bottom of the ice column across different wavelengths. This robustness across varying conditions, different lakes and

wavelengths, highlights microwaves effectiveness in capturing the state and progression of lake ice throughout the winter season. These results show that this dominance is not merely a function of wavelength or lake depth but is intrinsically tied to the interaction between microwave signals and the ice-water interface, likely influenced by surface roughness at this boundary.

These findings establish a strong foundation for the development of techniques such as Interferometric SAR (InSAR) analysis, where changes in phases between imaging pairs can be attributed to ice growth. This ice growth tracking via InSAR can be leveraged to quantify ice thickness over a winter season, which is only possible when there is confidence in the site of microwave interaction. The overarching trend of increasing signal power and relative power of single bound throughout the winter, regardless of platform, geographic regions, and lake depth, reinforces previous research and clearly demonstrates the importance of single-bounce scattering in microwave lake ice imaging.

6.1.2 Double-Bounce

Overall, the results of this study shows a reduction in the impact of double-bounce scattering mechanisms over winter across the breadth of this study. The observed decrease in signal importance implies that the vertical structures, which should be present in shallow lakes such as Old Crow, that theoretically contribute to double-bounce scattering, do not play a significant role in the total backscatter observed at the sensor. This observation is consistent across a range of wavelengths across multiple sensors, including TanDEM-X (9.65 GHz), RADARSAT-2 (5.6 GHz), and SAOCOM (1.275 GHz), reinforcing the conclusion that double-bounce scattering is not a dominant interaction in lake ice environments. While double-bounce scattering does show a general increase in signal strength across study sites, this is paired with a relative decrease in its proportion and importance within the overall microwave signal. This trend is also consistent with observations across

different sizes of wavelengths, highlighting the dominance of single-bounce and surface scattering mechanisms in the radar backscatter signal from lake ice. For example, the peak double-bounce power from the TanDEM-X, with its smaller wavelength, did not surpass the single bounce power of the larger SAOCOM wavelength. If interactions occurred with between tubular bubbles and microwaves, it is more likely that smaller X-band wavelengths would result in double bounce of the signal, which is not observed in this study. This finding is consistent with recent microwave modeling efforts investigating the primary drivers of backscatter from freshwater lake ice, whereby the inclusion of bubbles in the ice volume did not result in backscatter increases on the order of magnitude observed in laboratory or field experiments (Murfit et al., 2024).

Furthermore, the results of this study, which captures the microwave responses of 976 different lakes spread over across large geographic region, agrees with other observations of similar studies, highlighting that double bounce was not a major factor in the microwave signal composition, never exceeding 20% of the total signal composition. Several other studies also examined the contribution of double bounce backscattering to lake ice microwave backscatter by employing co-polarization phase analyses, and simpler polarimetric decomposition models (Engram et al., 2013; Atwood et al., 2015; Tian et al., 2015; Gunn et al 2018;). The co-polarization ratio peaked at 18.2° across all RADARSAT-2 and TanDEM-X acquisitions, indicating a minimal influence of double-bounce (Atwood et al., 2015) These results are similar to our study which showed a co-polarization ratio peak of 20.1. This is a critical observation, because if double bounce was observed the co-polarization ratio would be much higher, approaching 180 degrees (Atwood et al., 2015). Furthermore, for long winter time series of RADARSAT-2 and TanDEM-X acquisitions, the double bounce returns did not exceed -19dB and -17 dB, respectively (Engram et al., 2013; Gunn et al., 2018). The double-bounce backscatter magnitude observed in this study is consistent at -18 dB for RADARSAT-

2 and TanDEM-X, indicating very low power contribution to the overall signal composition. This study extends the results of previous studies across the northern hemisphere, repeatedly illustrating that there is little double bounce interaction in lake ice.

6.1.3 Volume Scattering

Volume scattering exhibits a dynamic characterized by increased average signal power and relative power, though with variability in its relative importance over time. At Old Crow, in standard beam mode 24, the average signal power for volume scattering increased from -28.62 dB in October 2011 to -19.66 dB by March 2012. Similarly, at Noel Lake, volume scattering in fine beam mode 2 showed an increase in signal strength from -24.36 dB in October 2018 to -17.80 dB by May 2019. This increase suggests enhanced interactions with structures within the snow and ice, likely due to the inclusion of more complex scatterers such as air pockets within the ice or the increasing structural complexity of snow layers and surface ice types accumulating over the winter.

This behavior is corroborated across multiple sensors, including TanDEM-X and SAOCOM, where volume scattering consistently shows an increase in signal power as winter progresses. For example, at the Utqiagvik site using TanDEM-X, the mean power for volume scattering increased from approximately -14 dB in early December to -11 dB by February, indicating the development of internal ice structures that enhance scattering. Similarly, in SAOCOM's L-band data, the volume scattering at Old Crow demonstrated an increase in mean power values from -25 dB in December to about -21 dB by February, reinforcing the pattern observed with RADARSAT-2 of growing complexity within the ice.

However, the total proportion of the microwave signal linked to volume scattering reveals a more complex picture. At Old Crow, in beam mode 24, the proportion decreased from 27.19% in October 2011 to 14.17% by March 2012. This indicates that while the absolute signal strength from

volume scattering increased, its relative importance within the microwave signal diminished. At Noel Lake, in fine beam mode 2, the proportion of the microwave signal attributed to volume scattering also decreased, moving from 9.44% in October 2018 to 5.13% by May 2019. This trend was mirrored in SAOCOM's L-band data at Noel Lake, where the proportion of volume scattering in the microwave signal decreased slightly despite an increase in absolute power, echoing the behavior observed in RADARSAT-2 data. Although the proportion of volume scattering declined, the decrease was less severe than that observed in double-bounce scattering.

Similar trends in the contribution of volume scatter to overall backscatter returns from freshwater lake ice are seen in this study compared to previous polarimetric analysis. When observing polarimetric decomposition of freshwater lake ice at both C- and L-bands, Atwood et al., (2015) noted that the signal proportion of volume scattering did not exceed 15% for the month of March in both C-band and L-band sensors. This is consistent with reported volume scatter proportions at all study regions, with a signal proportion hovering around 15%, but never exceeding 20%, across L-, C-, and X-band. In another study, Gunn et al., (2018) found that median C-band volume scattering power never exceeded -10 dB for median pixel values aggregated lake-wide, which is also reflected in our results, where volume scattering did not exceed -15 dB across all RADARSAT-2 lakes.

Lakes of various depths, environmental and physical factors across the northern hemisphere present variability in ice cover type and structure. Across multiple sensor platforms and wavelengths, single-bounce scattering remains the dominant backscattering mechanism, and the increasing signal power and relative proportion associated with volume scattering indicate its growing significance in characterizing the internal structure of lake ice throughout the winter.

6.2 Co-polarization

The co-polarization analysis conducted at two distinct sites, Old Crow and Noel Lake, provides insightful observations into the microwave signal behaviors at these locations. This analysis serves as a secondary step to reinforce the findings from the Yamaguchi-Freeman-Durden decomposition. At both sites, there is a consistent, marginal positive increase in the degrees as winter progresses, culminating in a significant rise in April. Such incremental changes have been identified in other studies as indicative of single-bounce interactions (Hajsek and Desno, 2021). The analysis further reveals minimal cross-polarization interactions, confirming that both HH and VV polarizations directly interact with the target. This suggests the absence of internal structures within the ice that could cause double-bounce effects, supporting the notion that tubular bubbles minimally impact the microwave signal. Atwood et al., (2015) presented a peak CPD near 18.2 degrees for C-band acquisitions throughout a single winter season, suggesting limited influence from double-bounce scattering. These results are consistent with our own findings, which showed a CPD peak of 20.1 degrees, further supporting the interpretation that single-bounce scattering dominates under these conditions. This is a key observation: if a strong double-bounce interaction were present, the phase difference would be significantly higher, approaching 180 degrees (Atwood et al., 2015). This is critical, as the co-polarization phase can indicate that there is a double-bounce interaction occurring, as two phase orientations will more strongly interact with the geometric structures of tubular bubbles. The minimal cross-polarization response observed supports the dominance of single-bounce scattering, reinforcing the reliability of the polarimetric decomposition findings, and is another piece of evidence supporting the use of PolSAR for monitoring the progression of lake ice and accurately quantifying ice thickness.

6.3 Uncertainty

Interpreting the results of this study requires an acknowledgment of the uncertainties mentioned in the methodology section. While the overall trends in scattering mechanisms remain consistent across the breadth of the study, variability in backscatter behavior must be contextualized within the inherent limitations of SAR imaging and processing. These uncertainties stem largely from the presence of speckle, the influence of incidence angle variations, and the sensor-specific characteristics that shape the data collected. Each of these factors introduces potential biases that must be considered when assessing the backscattering mechanisms of lake ice.

Speckle, an artifact of coherent microwave imaging, presents a key challenge in the interpretation of SAR results. This noise, resulting from the constructive and destructive interference of microwaves, introduces localized fluctuations in backscatter power that do not correspond to real physical variations of the target feature. While the Refined Lee Filter was applied uniformly across all acquisitions to suppress speckle, filtering itself carries its own limitations. The effect of speckle is particularly relevant when examining the relative proportions of single-bounce, double-bounce, and volume scattering, as even minor variations in power distribution can influence the polarimetric decomposition model.

A representative example of uncertainty in the dataset can be observed in Lake 2347, where an anomalous decrease in single-bounce scattering to -33.91 dB was recorded in a SAOCOM 1A acquisition on January 18, 2023. This value deviates considerably from the surrounding time steps of -23.48 dB (December 1, 2022) and -22.14 dB (January 29, 2023), as well as from other lakes of similar depth. No corresponding environmental event or physical justification was identified, and the outlier did not align with trends observed in the broader dataset. Given the isolated nature of the drop and its inconsistency with expected ice development, the value was attributed to speckle-related

interference, sensor anomaly, or geolocation distortion. While speckle suppression was uniformly applied using the Refined Lee Filter, such localized anomalies underscore the importance of visual and statistical quality control. This lake and lakes similar to it were excluded from summary visualizations and trend interpretation to prevent distortion of broader results.

The incidence angle at which SAR acquisitions are collected plays a significant role in shaping the observed backscatter response. Variations in incidence angle can affect the relative contributions of each scattering mechanism, as the geometry of the incoming wave alters the way microwaves interact with the ice surface and subsurface layers. As well, it has been shown in previous lake ice studies that changes in incidence angle as a direct effect on the return power (Duguay et al, 2002). The dataset used in this study incorporates acquisitions from multiple beam modes, each with its own range of incidence angles. In the case of RADARSAT-2, the fine beam mode 19 dataset, which captures at shallower angles, exhibits a slightly higher proportion of double-bounce scattering compared to fine beam mode 2. This difference could suggest that part of the variation in scattering behavior is influenced by the geometry of the incoming signal rather than a fundamental change in ice conditions between observations.

Beyond speckle and incidence angle variations, sensor-specific limitations introduce another layer of uncertainty. Each SAR platform operates at a distinct wavelength, and spatial resolution, factors that will influence the detection and characterization of lake ice properties. The X-band data from TanDEM-X, for example, exhibits consistently higher backscatter values compared to C-band and L-band acquisitions. This greater signal power could be reflective of the X-band shorter wavelength being better able to interact with the surface roughness variations of the ice-water interface, than L-band. The quantification of surface roughness at the ice-water interface is not currently well studied but current estimates of under-ice roughness for temperate lakes have been

reported with root mean square (RMS) of height deviations at 0.84mm (Bacal et al., 2024) .

According to Fraunhofer's roughness criterion, an RMS of 0.84mm for ice would be considered to be rough to incoming microwaves only approaching X-band frequencies (e.g. 9.6 GHz). When observed with RADARSAT-2 (5.6 GHz) or SAOCOM (1.275 GHz), the height deviations that are needed to appear rough to the sensor are well above the reported ice roughness values of 0.84mm. In the range of incidence angles observed in this study (19° to 44°), the roughness needed at the ice-water interface to satisfy the Fraunhofer criterion ranges between 0.99 and 1.37 mm RMS for C-band, and 4.28 to 5.6 mm RMS for L-band, respectively.

Uncertainties also arise from temporal gaps within the dataset, which limit the ability to capture continuous seasonal transitions in ice development. While the available data suggests a steady increase in single-bounce scattering throughout the winter months, it is unclear whether this trend remained linear or if start/mid/end-season fluctuations occurred that were not captured due to missing acquisitions. The presence of such gaps in this study means that any interpretations of seasonal evolution must be understood as constrained by the available time series rather than reflecting a perfectly continuous progression of backscatter changes.

A final limitation of this study lies in the inclusion of SAOCOM 1A/1B data, which introduced several processing challenges. The TOPSAR acquisition format presented compatibility issues with standard platforms such as SNAP and CATALYST, necessitating that key pre-processing steps, including debursting and geocorrection, be carried out manually in Python. While care was taken to ensure geolocational accuracy and to remove clearly anomalous artifacts, the absence of an automated toolchain introduced a higher potential for residual distortions and processing inconsistencies. These issues, particularly those related to sensor-based artifacts, were visually confirmed and documented during internal quality checks. Consequently, the reliability of the

SAOCOM-derived decomposition results is limited relative to data from better-supported platforms. While the sensor's long-wavelength L-band data theoretically offers valuable insight into freshwater lake ice backscattering behavior, the presence of unpredictable artifacts and alignment inconsistencies warrants caution in interpretation. These factors should be considered when comparing SAOCOM results with those from RADARSAT-2 and TanDEM-X, as differences in data quality and the apparent verisimilitude of the results may significantly contribute to the observed variability.

Taken together, these sources of uncertainty highlight the complexities of interpreting polarimetric SAR data for lake ice monitoring. While the overall trends observed, such as the dominance of single-bounce scattering and the irrelevance of double-bounce scattering, remain consistent across multiple sensors and study sites, localized variations must be understood within the context of the underlying limitations of this study and the fundamental limitations of SAR acquisitions. The impact of speckle, the influence of incidence angle, and the characteristics of each SAR platform all contribute to the variability seen in the results. Recognizing these factors ensures that the findings are framed appropriately, reinforcing the importance of careful methodological considerations when applying SAR-based techniques to the study of all natural features including ice-covered water bodies.

Chapter 7: Conclusion

This study has systematically investigated the interactions between fully polarimetric C-band, X-band, and L-band, microwave signals and lake ice, employing advanced statistical analysis techniques to SAR data to discern the various scattering mechanisms responsible for the backscatter signal. Through detailed analysis of two distinct sites, Old Crow and Noel Lake, and an expanded analysis of multiple platforms and locations, this work has enhanced the understanding of the microwave signals composition and what that indicates for the study of lake ice using microwave remote sensing.

7.1 Summary of Key Findings

The goal of this thesis was to address two key objectives: (1) to identify the difference in microwave backscatter behaviour across lakes of differing depths, and (2) to utilize polarimetric decomposition algorithms to quantify the dominant scattering mechanisms associated with lakes of different sizes. This thesis has successfully achieved both of stated objectives, leveraging microwave backscattering signal from 973 lakes, three different sensors, and a broad geographical range. In

addressing the first objective, this study found that microwave backscattering behaviour remained consistently dominated by single-bounce scattering throughout the winter period. This dominance only diminished near the end of the winter period with the onset late winter period and the melting season, which brings with it an overall reduction in backscatter power from the lakes. Following this, with the second objective, the results showed that lake size had minimal influence on the backscattering signal composition, with single-bounce remaining the dominant source of signal power across lakes from .4m to 18m in depth, for 973 different lakes. Similar to the depth based findings, the dominance of single-bounce was only lost with the onset of melting conditions and the reduction of the overall signal power that comes with it.

The findings from the RADARSAT-2, SAOCOM, and TanDEM-X polarimetric data analysis underscore the predominance of single-bounce scattering across the studied sites, which correlates to an interaction with a sufficiently rough ice-water interface surface. The predominance of single-bounce scattering mechanism suggests minimal interactions with internal ice features, consistent with case studies across the northern hemisphere (Engram et al., 2013; Atwood et al., 2015; Gunn et al., 2018). Notably, the development of the proportion of scattering mechanisms of the returned signal during the winter season provides crucial insights into the seasonal evolution of the ice-water interface of freshwater lake ice.

Furthermore, the minimal cross-polarization interactions observed across lake size and depth reinforce the conclusion that the internal structure of the lake ice at these sites during the study period did not significantly contribute to internal scattering events resulting in considerable double-bounce or volume scatter. Though, that does not exclude tubular bubbles from playing a role in the development of the ice-water interface, as the tubular-bubble terminus provides additional roughness at the interface. These observations are instrumental in refining radiative transfer models for

predicting and simulating microwave-ice interactions, which are essential for remote sensing applications in cryospheric studies.

7.2 Limitations

While this study provides a comprehensive analysis of polarimetric SAR backscatter interactions with lake ice, several limitations must be acknowledged, particularly the lack of in-situ validation and field-based measurements. Remote sensing studies inherently rely on indirect observations, and while SAR offers robust capabilities for monitoring ice conditions, the absence of ground-truth data introduces constraints in interpreting scattering behaviours. Without in-situ validation, it is difficult to explicitly link observed scattering mechanisms to physical on-site ice conditions. For instance, ground control points with ice and snow structure measurements would have provided critical reference points for validating the decomposition results, by confirming the exact features present at the study site. Having these characteristics would confirm the presence of tubular bubbles or aid in the discernment of observed volume scattering increases being linked to snow accumulation, superimposed ice, or internal bubble structures. To address this fundamental limitation this study relied on published literature presenting similar studies of microwave interaction with fresh water lake ice, where in-situ observations were present.

An additional limitation is the lack of multi-year repeat acquisitions for the same study sites, for each sensor, preventing the ability to extend the observations of this study beyond short snapshots of time captured. Multiple years of fully polarimetric microwave acquisitions over the same site allows for an analysis of the lake ice backscattering behaviour, which would address any anomalous winter ice conditions and provide a more robust and universally applicable conclusions. Currently, this study is limited to specific site and temporal observations where quad-pol SAR data is acquired over frozen lakes. It is important to note, that this study is rooted in opportunism, as quad-pol microwave captures

are rarely acquired, even by platforms that are designed for this capture mode in mind. This limited the availability of data to be leveraged in this study.

Finally, SAR sensors acquiring data in quad-pol mode is restricted in its geographic area covered. At only two sites, Old Crow Flats and Noel Lake, was this study able to use data from two sensors acquiring observations from the same geographic region, albeit for different years. Having multiple sensors capturing the same lake feature within an approximate similar timeframe would allow for more robust conclusions regarding microwave interaction with lake ice. Currently, the observations from the different sensors cannot be explicitly attributed to differences in sensor wavelength, as the backscattering behaviour could be site specific. To address this limitation a study must be designed to capture the same area with each sensor over a winter period.

Despite these limitations, the study provides a strong foundation for understanding SAR-based lake ice monitoring. Addressing these gaps in future work by integrating field measurements, ground-based radar, and supplementary remote sensing datasets would enhance confidence in backscatter interpretations and further refine our understanding of the physical mechanisms governing microwave interactions with freshwater ice.

7.3 Future Work

To build on the findings of this study, several key areas of future research should be explored. First and foremost, the integration of in-situ validation data remains critical for the calibration of SAR-based observations. Ground-based measurements of ice thickness, snow cover, and internal ice structure would offer a means to directly link SAR backscatter signals with physical properties of lake ice. These field measurements could be used to confirm the presence of specific internal ice features, such as tubular bubbles or characterize snow structures on the ice surface, which might influence

scattering mechanisms. Furthermore, including more detailed seasonal and temporal observations, through multi-year data for the same site, would help in understanding the potential interannual variations in lake ice dynamics. This expanded dataset would enable a more robust analysis of the evolution of the ice-water interface over time, improving our understanding of how the scattering behavior changes with different ice conditions over multiple winter seasons.

To further refine our understanding of the scattering mechanisms observed in SAR data, future research should explore the direct physical measurement of lake ice surface roughness. While SAR data provides valuable insights into backscatter interactions, it is limited in its ability to directly quantify the fine-scale surface roughness of the ice. This necessitates a need for a peak underneath the ice column to deduce the surface's characteristics. This could be achieved by deploying a sonar system or utilizing divers equipped for underwater measurements, it is possible to capture detailed profiles of the ice-water surface. These under ice based measurements would complement SAR observations, providing critical data to validate and enhance models of ice-water interface interactions.

Additionally, the development of more advanced modeling techniques, such as the Snow Microwave Radiative Transfer Model (SMRT), that simulate backscatter from ice with various characteristics could lead to more accurate understanding of the interaction of microwaves with the ice-water interface (Picard et al., 2018). Such models could be used to simulate a multitude of ice conditions, wavelengths and orientations, making them invaluable for analyzing microwave backscattering characteristics. By addressing these aspects in future work, we can refine the methods used to monitor and predict lake ice conditions through SAR remote sensing, contributing to a more accurate understanding of cryospheric processes.

References

- Adams, W. P., & Roulet, N. T. (1980). Illustration of the Roles of Snow in the Evolution of the Winter Cover of a Lake. *ARCTIC*, 33(1), 100–116. <https://doi.org/10.14430/arctic2550>
- Adams, W. P., & Roulet, N. T. (1984). Sampling of Snow and Ice on Lakes. *ARCTIC*, 37(3), 270–275. <https://doi.org/10.14430/arctic2200>
- Adrian, R., O'Reilly, C. M., Zagarese, H., Baines, S. B., Hessen, D. O., Keller, W., Livingstone, D. M., Sommaruga, R., Straile, D., Van Donk, E., Weyhenmeyer, G. A., & Winder, M. (2009). Lakes as sentinels of climate change. *Limnology and Oceanography*, 54(6part2), 2283–2297. https://doi.org/10.4319/lo.2009.54.6_part_2.2283
- Alexeev, V. A., Arp, C. D., Jones, B. M., & Cai, L. (2016). Arctic sea ice decline contributes to thinning lake ice trend in northern Alaska. *Environmental Research Letters*, 11(7), 074022. <https://doi.org/10.1088/1748-9326/11/7/074022>

- Atwood, D. K., Gunn, G. E., Roussi, C., Wu, J., Duguay, C., & Sarabandi, K. (2015). Microwave Backscatter From Arctic Lake Ice and Polarimetric Implications. *IEEE Transactions on Geoscience and Remote Sensing*, 53(11), 5972–5982.
<https://doi.org/10.1109/TGRS.2015.2429917>
- Bengtsson, L. (2023). Spatial Variability of Lake Ice Covers. *Geografiska Annaler*.
- Bengtsson, L., Herschy, R. W., & Fairbridge, R. W. (Eds.). (2012). *Encyclopedia of Lakes and Reservoirs*. Springer Netherlands. <https://doi.org/10.1007/978-1-4020-4410-6>
- Boereboom, T., Depoorter, M., Coppens, S., & Tison, J.-L. (2012). Gas properties of winter lake ice in Northern Sweden: Implication for carbon gas release. *Biogeosciences*, 9(2), 827–838.
<https://doi.org/10.5194/bg-9-827-2012>
- Bring, A., Fedorova, I., Dibike, Y., Hinzman, L., Mård, J., Mernild, S. H., Prowse, T., Semenova, O., Stuefer, S. L., & Woo, M. -K. (2016). Arctic terrestrial hydrology: A synthesis of processes, regional effects, and research challenges. *Journal of Geophysical Research: Biogeosciences*, 121(3), 621–649. <https://doi.org/10.1002/2015JG003131>
- Brisco, B., Ahern, F., Hong, S. H., Wdowinski, S., Murnaghan, K., White, L., & Atwood, D. K. (2015). Polarimetric decompositions of temperate wetlands at C-band. *IEEE Journal of Selected Topics in Applied Earth Observations and Remote Sensing*, 8(7), 3585-3594.
- Brown, L. C., & Duguay, C. R. (2010). The response and role of ice cover in lake-climate interactions. *Progress in Physical Geography: Earth and Environment*, 34(5), 671–704.
<https://doi.org/10.1177/0309133310375653>
- Brunelli, B., & Mancini, F. (2024). Comparative analysis of SAOCOM and Sentinel-1 data for surface soil moisture retrieval using a change detection method in a semiarid region (Douro

- River's basin, Spain). *International Journal of Applied Earth Observation and Geoinformation*, 129, 103874. <https://doi.org/10.1016/j.jag.2024.103874>
- Cherepanov, N. (1974). Classification of ice of natural water bodies. *Ocean '74 - IEEE International Conference on Engineering in the Ocean Environment*, 97–101. <https://doi.org/10.1109/OCEANS.1974.1161327>
- Degtyarev, V. G. (2007). Effect of deep freezing of lakes on food supply in habitats of waterbirds. *Russian Journal of Ecology*, 38(6), 408–412. <https://doi.org/10.1134/S1067413607060057>
- Dibike, Y., Prowse, T., Saloranta, T., & Ahmed, R. (2011). Response of Northern Hemisphere lake-ice cover and lake-water thermal structure patterns to a changing climate. *Hydrological Processes*, 25(19), 2942–2953. <https://doi.org/10.1002/hyp.8068>
- Dieleman, C. M., Branfireun, B. A., & Lindo, Z. (2017). Northern peatland carbon dynamics driven by plant growth form—The role of graminoids. *Plant and Soil*, 415(1–2), 25–35. <https://doi.org/10.1007/s11104-016-3099-3>
- Engram, M., Anthony, K. W., Meyer, F. J., & Grosse, G. (2013a). Synthetic aperture radar (SAR) backscatter response from methane ebullition bubbles trapped by thermokarst lake ice. *Canadian Journal of Remote Sensing*, 38(6), 667–682. <https://doi.org/10.5589/m12-054>
- Ferguson, J. E., & Gunn, G. E. (2022). Polarimetric decomposition of microwave-band freshwater ice SAR data: Review, analysis, and future directions. *Remote Sensing of Environment*, 280, 113176. <https://doi.org/10.1016/j.rse.2022.113176>
- Fissel, D., Marko, J., & Melling, H. (2008). Advances in Marine Ice Profiling for Oil and Gas Applications. *Day 3 Tue, July 22, 2008*, D031S011R001. <https://doi.org/10.5957/ICETECH-2008-134>

Freeman, A., & Durden, S. L. (1998). A three-component scattering model for polarimetric SAR data. *IEEE Transactions on Geoscience and Remote Sensing*, 36(3), 963–973.

<https://doi.org/10.1109/36.673687>

Griffiths, D. J., & Inglefield, C. (2005). *Introduction to Electrodynamics*. *American Journal of Physics*, 73(6), 574–574. <https://doi.org/10.1119/1.4766311>

Griffiths, K., Michelutti, N., Sugar, M., Douglas, M. S. V., & Smol, J. P. (2017). Ice-cover is the principal driver of ecological change in High Arctic lakes and ponds. *PLOS ONE*, 12(3), e0172989. <https://doi.org/10.1371/journal.pone.0172989>

Gunn, G. E., Duguay, C. R., Atwood, D. K., King, J., & Toose, P. (2018). Observing Scattering Mechanisms of Bubbled Freshwater Lake Ice Using Polarimetric RADARSAT-2 (C-Band) and UW-Scat (X- and Ku-Bands). *IEEE Transactions on Geoscience and Remote Sensing*, 56(5), 2887–2903. <https://doi.org/10.1109/TGRS.2017.2786158>

Gunn, G. E., Duguay, C. R., Brown, L. C., King, J., Atwood, D., & Kasurak, A. (2015). Freshwater lake ice thickness derived using surface-based X- and Ku-band FMCW scatterometers. *Cold Regions Science and Technology*, 120, 115–126.

<https://doi.org/10.1016/j.coldregions.2015.09.012>

Gunn, G. E., Duguay, C. R., Atwood, D. K., King, J., & Toose, P. (2018). Observing scattering mechanisms of bubbled freshwater lake ice using polarimetric RADARSAT-2 (C-Band) and UW-Scat (X-and Ku-Bands). *IEEE Transactions on Geoscience and Remote Sensing*, 56(5), 2887-2903.

- Gunn, G. E., Tarabara, V., Ruttu, M., Bessette, D. L., & Richardson, R. B. (2021). Roughness and storage capacity of freshwater ice in the Straits of Mackinac. *Cold Regions Science and Technology*, 186, 103278. <https://doi.org/10.1016/j.coldregions.2021.103278>
- Hannevik, T. (2011). Evaluation of Radarsat-2 for ship detection. *Norwegian Defense Research Establishment*, ISBN 978-82-464-2026-4, 59pp.
- Hajnsek, I., & Desnos, Y.-L. (Eds.). (2021). *Polarimetric Synthetic Aperture Radar: Principles and Application* (Vol. 25). Springer International Publishing. <https://doi.org/10.1007/978-3-030-56504-6>
- Hall, D. K. (1982). A Review of the Utility of Remote Sensing in Alaskan Permafrost Studies. *IEEE Transactions on Geoscience and Remote Sensing*, GE-20(3), 390–394. <https://doi.org/10.1109/TGRS.1982.350460>
- Huang, L., Timmermann, A., Lee, S.-S., Rodgers, K. B., Yamaguchi, R., & Chung, E.-S. (2022). Emerging unprecedented lake ice loss in climate change projections. *Nature Communications*, 13(1), 5798. <https://doi.org/10.1038/s41467-022-33495-3>
- Kämäri, M., Alho, P., Colpaert, A., & Lotsari, E. (2017). Spatial variation of river-ice thickness in a meandering river. *Cold Regions Science and Technology*, 137, 17–29. <https://doi.org/10.1016/j.coldregions.2017.01.009>
- Kirillin, G., Leppäranta, M., Terzhevik, A., Granin, N., Bernhardt, J., Engelhardt, C., Efremova, T., Golosov, S., Palshin, N., Sherstyankin, P., Zdorovenova, G., & Zdorovenov, R. (2012a). Physics of seasonally ice-covered lakes: A review. *Aquatic Sciences*, 74(4), 659–682. <https://doi.org/10.1007/s00027-012-0279-y>

Kirillina, K., Tananaev, N., Savvinova, A., Lobanov, V., Fedorova, A., & Borisov, A. (2023).

Climate change impacts the state of winter roads connecting indigenous communities: Case study of Sakha (Yakutia) Republic. *Climate Services*, 30, 100356.

<https://doi.org/10.1016/j.cliser.2023.100356>

Kraemer, B. M., Anneville, O., Chandra, S., Dix, M., Kuusisto, E., Livingstone, D. M., Rimmer,

A., Schladow, S. G., Silow, E., Sitoki, L. M., Tamatamah, R., Vadeboncoeur, Y., &

McIntyre, P. B. (2015). Morphometry and average temperature affect lake stratification responses to climate change. *Geophysical Research Letters*, 42(12), 4981–4988.

<https://doi.org/10.1002/2015GL064097>

Langley, K., Hamran, S.-E., Hogda, K. A., Storvold, R., Brandt, O., Hagen, J. O., & Kohler, J.

(2007). Use of C-Band Ground Penetrating Radar to Determine Backscatter Sources Within Glaciers. *IEEE Transactions on Geoscience and Remote Sensing*, 45(5), 1236–1246.

<https://doi.org/10.1109/TGRS.2007.892600>

Lauriol, B., Duguay, C. R., & Riel, A. (2002). Response of the Porcupine and Old Crow rivers in northern Yukon, Canada, to Holocene climatic change. *The Holocene*, 12(1), 27–34.

<https://doi.org/10.1191/0959683602hl517rp>

Luo, H., Tong, L., Li, X., Chen, Y., Liu, X., Li, M., & Zhang, Y. (2007). *Polarimetric SAR image classification based on polarimetric decomposition and neural networks theory* (S. J.

Maybank, M. Ding, F. Wahl, & Y. Zhu, Eds.; p. 67881P). <https://doi.org/10.1117/12.750037>

Michaud, A. B., & Apollonio, S. (2022). Overwinter oxygen and silicate dynamics in a high Arctic lake (Immerk Lake, Devon Island, Canada). *Inland Waters*, 12(3), 418–426.

<https://doi.org/10.1080/20442041.2022.2063623>

- Michel, B., & Ramseier, R. O. (1971). Classification of river and lake ice. *Canadian Geotechnical Journal*, 8(1), 36–45. <https://doi.org/10.1139/t71-004>
- Murfitt, J. C., Brown, L. C., & Howell, S. E. L. (2018). Estimating lake ice thickness in Central Ontario. *PLOS ONE*, 13(12), e0208519. <https://doi.org/10.1371/journal.pone.0208519>
- Murfitt, J., & Duguay, C. R. (2021). 50 years of lake ice research from active microwave remote sensing: Progress and prospects. *Remote Sensing of Environment*, 264, 112616. <https://doi.org/10.1016/j.rse.2021.112616>
- Murfitt, J., Duguay, C. R., Picard, G., & Gunn, G. E. (2022). Investigating the Effect of Lake Ice Properties on Multifrequency Backscatter Using the Snow Microwave Radiative Transfer Model. *IEEE Transactions on Geoscience and Remote Sensing*, 60, 1–23. <https://doi.org/10.1109/TGRS.2022.3197109>
- Murfitt, J., Duguay, C., Picard, G., & Lemmetyinen, J. (2024). Forward modelling of synthetic-aperture radar (SAR) backscatter during lake ice melt conditions using the Snow Microwave Radiative Transfer (SMRT) model. *The Cryosphere*, 18(2), 869-888. <https://doi.org/10.5194/tc-18-869-2024>.
- Page, D. F., & Ramseier, R. O. (1975). Application of Radar Techniques to Ice and Snow Studies. *Journal of Glaciology*, 15(73), 171–191. <https://doi.org/10.3189/S0022143000034365>
- Picard, G., Sandells, M., & Lowe, H. (2018). A New Active/Passive Microwave Radiative Transfer Model for Snow (SMRT) to Foster Inter-Comparisons of Model Components. *IGARSS 2018 - 2018 IEEE International Geoscience and Remote Sensing Symposium*, 6276–6279. <https://doi.org/10.1109/IGARSS.2018.8517407>

- Prowse, T., Alfredsen, K., Beltaos, S., Bonsal, B., Duguay, C., Korhola, A., McNamara, J., Vincent, W. F., Vuglinsky, V., & Weyhenmeyer, G. A. (2011). Arctic Freshwater Ice and Its Climatic Role. *AMBIO*, 40(S1), 46–52. <https://doi.org/10.1007/s13280-011-0214-9>
- Rafat, A., Kheyrollah Pour, H., Spence, C., Palmer, M. J., & MacLean, A. (2023). An analysis of ice growth and temperature dynamics in two Canadian subarctic lakes. *Cold Regions Science and Technology*, 210, 103808. <https://doi.org/10.1016/j.coldregions.2023.103808>
- Robinson, A. L., Ariano, S. S., & Brown, L. C. (2021). The Influence of Snow and Ice Albedo towards Improved Lake Ice Simulations. *Hydrology*, 8(1), 11. <https://doi.org/10.3390/hydrology8010011>
- Rouse, W. R., Oswald, C. J., Binyamin, J., Spence, C., Schertzer, W. M., Blanken, P. D., Bussi eres, N., & Duguay, C. R. (2005). The Role of Northern Lakes in a Regional Energy Balance. *Journal of Hydrometeorology*, 6(3), 291–305. <https://doi.org/10.1175/JHM421.1>
- [Vogt, C. 1999. Creating Long Documents using Microsoft Word. Published on the Web at the University of Waterloo.]
- Schertzer, W. M., Rouse, W. R., Blanken, P. D., & Walker, A. E. (2003). Over-Lake Meteorology and Estimated Bulk Heat Exchange of Great Slave Lake in 1998 and 1999. *Journal of Hydrometeorology*, 4(4), 649–659. [https://doi.org/10.1175/1525-7541\(2003\)004<0649:OMAEBH>2.0.CO;2](https://doi.org/10.1175/1525-7541(2003)004<0649:OMAEBH>2.0.CO;2)
- Scott, K. A., Xu, L., & Pour, H. K. (2020). Retrieval of ice/water observations from synthetic aperture radar imagery for use in lake ice data assimilation. *Journal of Great Lakes Research*, 46(6), 1521–1532. <https://doi.org/10.1016/j.jglr.2020.08.018>

- Shaposhnikova, M., Duguay, C., & Roy-Léveillé, P. (2023). Bedfast and floating-ice dynamics of thermokarst lakes using a temporal deep-learning mapping approach: Case study of the Old Crow Flats, Yukon, Canada. *The Cryosphere*, 17(4), 1697–1721.
<https://doi.org/10.5194/tc-17-1697-2023>
- Sharma, S., Blagrove, K., Magnuson, J. J., O'Reilly, C. M., Oliver, S., Batt, R. D., Magee, M. R., Straile, D., Weyhenmeyer, G. A., Winslow, L., & Woolway, R. I. (2019). Widespread loss of lake ice around the Northern Hemisphere in a warming world. *Nature Climate Change*, 9(3), 227–231. <https://doi.org/10.1038/s41558-018-0393-5>
- Staroszczyk, R. (2019). *Ice Mechanics for Geophysical and Civil Engineering Applications*. Springer International Publishing. <https://doi.org/10.1007/978-3-030-03038-4>
- Thompson, Simpson, Whitman, Barber, & Parisien. (2019). Peatland Hydrological Dynamics as A Driver of Landscape Connectivity and Fire Activity in the Boreal Plain of Canada. *Forests*, 10(7), 534. <https://doi.org/10.3390/f10070534>
- Warner, K., Fowler, R., Northington, R., Malik, H., McCue, J., & Saros, J. (2018). How Does Changing Ice-Out Affect Arctic versus Boreal Lakes? A Comparison Using Two Years with Ice-Out that Differed by More Than Three Weeks. *Water*, 10(1), 78.
<https://doi.org/10.3390/w10010078>
- Weeks, W. F., Fountain, A. G., Bryan, M. L., & Elachi, C. (1978). Differences in radar return from ice-covered North Slope Lakes. *Journal of Geophysical Research*, 83(C8), 4069.
<https://doi.org/10.1029/JC083iC08p04069>
- Woodhouse, I. H. (2006). *Introduction to microwave remote sensing*. Taylor&Francis.

Wu, J., Atwood, D., & Sarabandi, K. (2016). Scattering phenomenology of arctic lake ice. *2016 IEEE International Geoscience and Remote Sensing Symposium (IGARSS)*, 3668–3671.

<https://doi.org/10.1109/IGARSS.2016.7729950>

Yamaguchi, Y., Moriyama, T., Ishido, M., & Yamada, H. (2005). Four-component scattering model for polarimetric SAR image decomposition. *IEEE Transactions on Geoscience and Remote Sensing*, *43*(8), 1699–1706. <https://doi.org/10.1109/TGRS.2005.852084>

Yang, Y., Xiong, X., Melville, B. W., & Sturm, T. W. (2021). Dynamic morphology in a bridge-contracted compound channel during extreme floods: Effects of abutments, bed-forms and scour countermeasures. *Journal of Hydrology*, *594*, 125930.

<https://doi.org/10.1016/j.jhydrol.2020.125930>